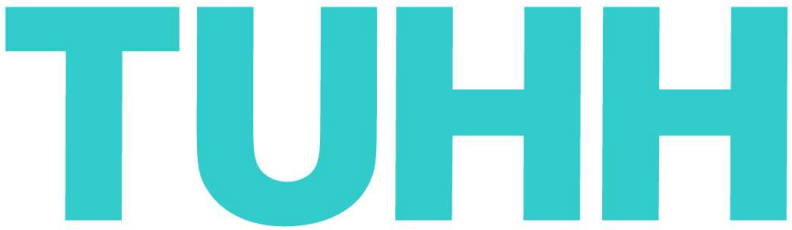

Technische Universität Hamburg-Harburg

Diploma Thesis

Modelling of an Accelerator Based X-ray Free Electron Laser System for Controller Design

Winter term 2005/2006

Author:	Guido Koch
Field of Study:	Mechatronics
Immatriculation number:	18852
Submission date:	30.11.2005

Institute:	Institute for Control Engineering
Supervisors:	Dr.-Ing. Gerwald Lichtenberg
	Dipl. Phys. Alexander Brandt (DESY)
1. Examinator:	Prof. Dr.-Ing. Herbert Werner
2. Examinator:	Prof. Dr. rer. nat. Ernst Brinkmeyer

Hiermit erkläre ich, die vorliegende Arbeit selbstständig durchgeführt und keine weiteren Hilfsmittel und Quellen als die angegebenen genutzt zu haben.

Hamburg, den 30.11.2005 Guido Koch

Abstract

Free Electron Lasers (FEL) operating in the X-ray wavelength range are a current field of research in physics. They will lead to a tremendous gain in insight of various science disciplines, e.g. material science, biology or chemistry.
The FELs coherent radiation is produced using linear accelerator structures to increase the energy of electrons by the interaction with electromagnetic radio frequency (RF) fields. At the German Electron Synchrotron (DESY), an FEL is already operating in the ultraviolett wavelength range. The "quality" of the emitted radiation critically depends on the stability of the RF-fields, which are so far controlled in amplitude and phase by a decentralized P-controller. The severe control objectives needed for the emission of coherent X-ray radiation are not satisfied yet.
In this thesis models for the linear accelerator system at DESY have been developed with respect to the application of high performance RF-field controller synthesis methods. The first steps have been the analysis and parameter estimation for an existing LPV state space model. Moreover, two kinds of LTI models have been developed using a system identification approach: A state space model structure with an additional, estimated parameter disturbance input and two MIMO state space models.
On the basis of the obtained models a first design approach to a multivariable dynamic controller has been made using nonlinear controller design methods.

Contents

Chapter 1

Introduction

One important aspect of various natural sciences is the structural investigation of matter. In physics structural and electronic properties of matter are an intense field of research while in biology atoms and molecules incorporated in large biomolecular complexes shall be studied more intensively. Chemists dream of a way of being able to visualize the dynamical behaviour of electrons forming chemical bonds and thus "film" a chemical reaction. All these research activities need a light source that is able to resolve objects on an atomic level.

The wavelengths of X-ray radiation are in the range of the diameter of an atom (10^{-10}m or equally 1Å) such that X-ray radiation is suitable for the desired experiments. However, conventional X-ray sources can not provide X-ray pulses with a sufficiently short pulse length. This has the effect that single biomolecules are destroyed by the highly energetic radiation as well as the pulse lengths being too long to resolve the fast dynamical processes of a chemical reaction. Moreover, the resolution of conventionally[1] produced X-ray radiation is limited by the broadness of its spectrum. Laser light on the other hand, which is used for a variety of optical experiments, can be optimally focussed compared with other light and very short laser pulses can be produced.

The physician Emilio Segrè formulated in 1980: *In the 1920's we used to joke that good physicists, once passed to their heavenly rewards, would find* (an) *apparatus in paradise which, with a twist of knobs, would give electromagnetic radiation of any desired frequency, intensity, polarisation, and direction of propagation*, [21]. The properties desired for the radiation are mainly properties of laser light (see section 2.1.1), however conventional lasers operate in the wavelength range of visible light and in the infrared and ultraviolett spectrum. If it would be possible to produce laser light with a wavelength in the X-ray range all the prospected experiments mentioned above could be done. Thus, with such a light source a tremendous gain in insight in various disciplines of science would be expectable.

A current field of research in particle accelerator physics are *Free Electron Lasers (FELs)*,

[1] For example by an X-ray vacuum tube.

which produce radiation with the properties of laser radiation but with tuneable wavelength. In section 2.1.1 it will be explained, how a free electron laser works and how it is possible to lower the wavelength of its radiation such that it reaches the X-ray range.

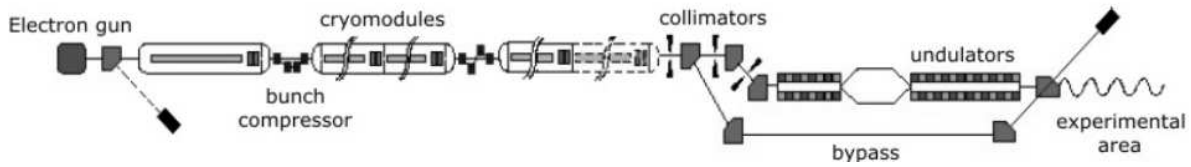

Figure 1.1: Structure of a free electron laser

At the *German Electron Synchrotron (DESY)* in Hamburg a european research project is conducted called *XFEL - X-ray Free Electron Laser*. This project will be described in section 2.1.2. The goal the XFEL-project is to realize an *Free Electron Laser (FEL)* operating in the X-ray wavelength range. At DESY an FEL is already operating in the ultraviolett wavelength range, the *VUV-FEL - Vacuum ultraviolett FEL*. For the realization of an FEL a linear accelerator is needed, which increases the energy of loaded particles, electrons in this case, by the interaction with electromagnetic radio frequency fields (*RF-fields*). The emission of the X-ray radiation crucially depends on the stability of the electromagnetic fields in the accelerator. For the stabilization of the fields a control system is used. The control objectives, i.e. the specifications for the fields quality that must be met by the control system for the XFEL to work properly, are introduced in section 2.2.7.

In the framework of the control objectives formulated for the XFEL-project this thesis is an approach to the development of a new control control strategy for the electromagnetic fields of the FEL's linear accelerator system. The goal of the thesis presented in the next subsection mainly involves the modelling of the linear accelerator system operating at DESY such that model based high performance field controllers can be designed.

A first RF-field control objective formulation for the XFEL-project

Figure 1.1 shows the structure of an FEL. For the emission of coherent radiation it is required to increase the energy of electrons by a linear accelerator consisting of resonators housed in *cryomodules*. In chapter 2 detailled explanations on linear accelerators will be given. The properties coherence and brilliance of the radiation produced by an FEL depend mainly on the energy spread of the electron beam. The energy spread has to be low in order to achieve the SASE effect described in section 2.3. Energy gain of the electrons in the linear accelerator is caused by the interaction of the electrons with oscillating electromagnetical RF-fields. To clearly formulate the control objectives for the RF-field stability the linear accelerator system has to be explained in detail, which will be done in chapter 2.2. Here, a first formulation is given to illustrate the objectives severity in order to formulate the goal of this thesis.

The linear accelerator at DESY is operated in *pulsed mode*, i.e. the RF-fields inside the

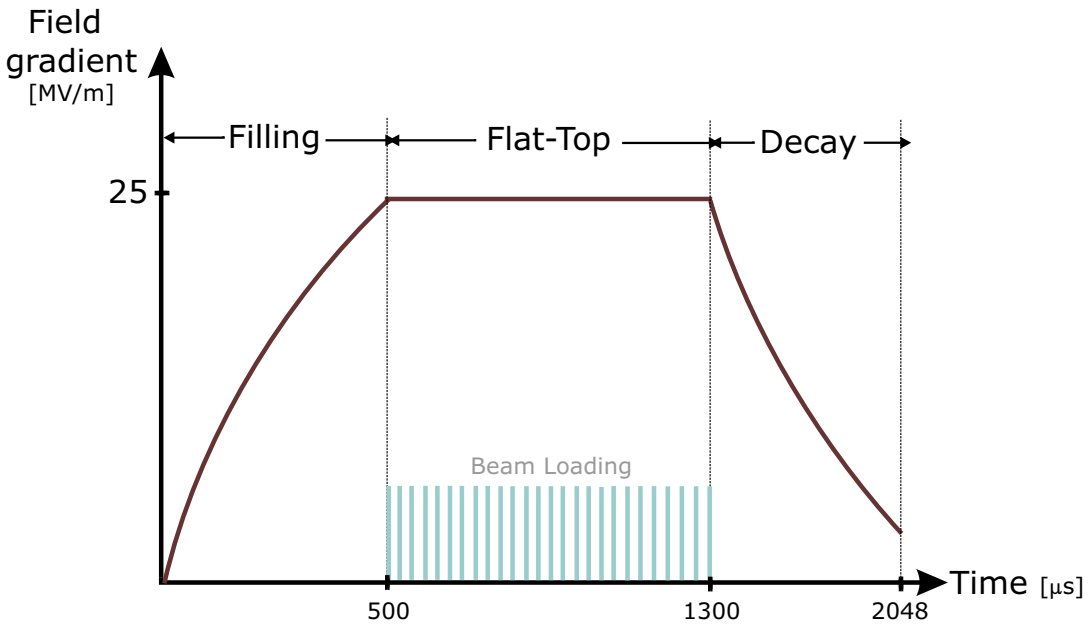

Figure 1.2: Timing structure of an RF-pulse in the superconducting cavities of TTF2 (numerical values are only exemplary)

accelerators superconducting cavities are supplied by an actuator system for a finite time interval and then turned off again iteratively. A reason for the operation in pulsed mode is less required cooling power of the cryogenic system. The timing structure of an RF-pulse is shown in Figure 1.2. In this figure the RF-field amplitude, which is also called *gradient*, is displayed as a function of time. The field builds up inside the accelerator's cavities and once the required gradient for appropriate energy gain of the electrons is reached it has to be kept constant. During this so called *flat top phase* the electron beam is injected into the accelerator. When the electron beam has passed, the RF-field is turned off and the field amplitude decays.

The oscillating RF-fields must be kept constant in amplitude and phase during the flat top time interval to transfer a precise amount of energy to the electrons. A more detailed explanation will be given in chapter 2.2. The control-objectives regarding the necessary RF-field stability for the XFEL are specified as follows:

- The field amplitude must be kept constant with a precision of 0.01% of the reference value.
- The field phase may not differ from the reference value by more than 0.01°.

Goal of the thesis

The focus of this thesis is the first module (ACC1) of the accelerator section of the VUV-FEL at DESY's TESLA Test Facility 2 (TTF2). Fullfilling the control objectives presented in

the previous section is crucial for the success of the XFEL-Project. Compared with control objectives for industrial applications the required amplitude and phase precision are very severe. Moreover, the degree of complexity of the *plant*, i.e. the system to be controlled, is very high. The complexity results from a variety of different electronical, electrical and mechanical components which are spatially distributed over a wide range. The system is highly susceptible to various kinds of disturbances affecting the operation and the RF-fields inside the superconducting cavities in particular. Up to now, a decentralized proportional feedback is used for the control of the RF-fields.

Steps towards achieving the control objectives can be done by improving hardware components and designing high performance RF-field controllers. The design or *synthesis* of these controllers is model based. This means a mathematical model of the input/output (I/O) behaviour of the plant to be controlled must be developed because its properties influence the structure and parametrization of the high performance controller. Modelling of TTF2 so far has been done using first principles, i.e. equations based on physical laws. For the superconducting cavities in particular, a model consisting of two linear time varying differential equations has been developed using analogies to an electrical resonant circuit.

The main goal of this thesis is to derive models of the RF-field behaviour in the first module (called *ACC1*) of the linear accelerator system containing 8 superconducting cavities. The mathematical models must be suitable for high performance controller synthesis which means that the model must be able to accurately predict the I/O behaviour for a specified set of operating points if the same input signals are applied to the model and the real system. The term "accurate" refers to minimal deviations of model output signals from measured output signals and the deviations should be of the order of magnitude of the required control accuracy.

The goals of the thesis can be summarized to:

- *Analysis and simulation of the existing resonant circuit model*: It must be clarified whether the model is suitable for high performance controller design. Therefore it must be tested, how accurate the model structure predicts the systems I/O behaviour. Parameter estimation should be used to reduce the influence of not exactly known parameters on the model performance

- *System identification of the accelerator section ACC1*: With this experimental based way of modelling, the I/O behaviour of the accelerator system consisting of an actuator system and eight superconducting cavities should be modelled. Models must be developed for the large signal I/O behaviour during the RF-pulse as well as the small signal I/O behaviour during the flat top. For modelling the influence of the beam is not to be taken into account and a correct calibration of the system is assumed.

- *A first approach on multivariable controller design*: On the basis of a suitable developed model that describes the I/O behaviour of ACC1 during the RF-pulse it should be clarified if a multivariable controller can improve the performance of the RF-fields. Especially achievement of asymptotic tracking of the reference value and

low overshoot at the beginning of the flat top must be in the focus of the design. For the controller design actuator constraints shall be taken into account. The controllers must be designed with respect to applicability in a new FPGA based signal processing system.

Outline of the thesis

In chapter 2 principles of free electron lasers (FELs) and the XFEL-project at DESY will be presented as well as an overview of the linear accelerator system. The frequency control system for the stabilization of the RF-fields inside the linear accelerator's superconducting cavities will be described in the coverage necessary for the modelling and controller design presented this thesis. With this fundamentals presented, the control objectives will be precisely formulated.

Chapter 3 starts with an overview of most commonly used model structures for *linear time invariant (LTI)* and *linear paramater varying (LPV)* systems. Then two kinds of model building procedures will be illustrated: Modelling by *first principles*, e.g. physical insight into the system behaviour, and *system identification*, an experimental based way to obtain a mathematical model of the behaviour of a dynamical system. The theoretical framework for modelling by system identification will be given.

The modelling of the first linear accelerator section (ACC1) will be presented in chapter 4. An approach to model the accelerator system and the superconducting cavities in particular by using analogies to an electrical resonant circuit will be presented on the basis of [20]. The model will be analyzed by means of systems theory. Furthermore, the performance of the resonant circuit model will be tested by comparing measurement data with output data of a simulation model based on the obtained model structure which will be parametrized using parameter estimation methods.

Chapter 5 describes system identification of the RF-system of ACC1. By this modelling approach it shall be tested whether more accurate models for specified operating conditions of the system can be developed. The experiments performed at TTF2 and a first analysis of measurement data are presented. Two different model structures are parametrized on the basis of the data recorded during the system identification experiments at TTF2. Both model structures are linear time invariant models, in one model structure a *parameter disturbance input* is incorporated while the other model structure is a multivariable state space model without an additional input signal. Models for the large signal behaviour of ACC1 at TTF2 are presented that describe the system behaviour during the whole RF-pulse time interval as well as a small signal model that describes the behaviour of the RF-fields during the flat top. The models are validated, analyzed and the large signal models are compared to the resonant circuit model.

A first approach of multivariable controller design for the section ACC1 of the linear accelerator is described in chapter 6. The controller structure has been chosen under consideration of applicability in an *FPGA* system that will be implemented for signal processing at

TTF2. Different multivariable controllers are presented and their RF-field performance is compared.

The conclusions and an outlook on future work will be given in chapter 7. The results of this thesis provide a basis for the application of further controller synthesis methods in order to take steps to fulfilling the control objectives necessary for the XFEL-project to be successfull.

In Appendix A a mathematical tool needed for system identification is explained, the *singular value decomposition*. Appendix B contains diagrams regarding the system identification of ACC1. Further aspects of system theoretical analysis of the developed small signal model of ACC1 are presented in Appendix C and Appendix D contains diagrams to illustrate the performance in simulation of designed multivariable controllers.

Chapter 2

Radio frequency system of the linear accelerator

The pre-step of modelling the first module of the TTF2 linear accelerator system is to get an insight into its operating principles and its components. In this chapter, first a motivation is given where the principles of free electron lasers are explained and the XFEL-project at DESY is presented (section 2.1). The accelerator system, its components and the function of the superconducting cavities in particular is presented in Section 2.2. Then in Section 2.2.2 the focus is put on the *Low Level Radio Frequency (LLRF)* control system that is used to stabilize the RF-fields in amplitude and phase. In particular the actuator system and the signal processing of the LLRF system is presented.

In Section 2.2.4 the main calibration parameters are described and some consequences are discussed the calibration has for control of the system. In Section 2.2.5 disturbance sources are presented that lead to corruption of the RF-field performance such that their effects on the RF-fields have to be compensated by the control system. The current structure of the LLRF control system is illustrated in Section 2.2.6. In Section 2.2.7 the controller parameters are formulated precisely with respect to the technical background layed previously in this chapter. Section 2.2.8 gives an idea about actuator constraints.

It shall be emphasized that the highly complex accelerator system is presented only in its basic principles such that a framework for understanding issues relevant for the modelling process of the I/O behaviour is given.

2.1 Motivation

2.1.1 Principles of Free Electron Lasers (FEL)

Before the operating principles of FELs are presented a brief illustration about conventional lasers and the properties of laser radiation is given. It will become clear that various aspects of the radiation production in an FEL are very similar to conventional laser sources like Helium-Neon lasers.

Laser radiation and conventional lasers

Laser radiation is used for various optical applications in scientific as well as industrial contexts. The term *laser* stands for "Light Amplification by Stimulated Emission". In conventional lasers, the radiation is emitted by electron transitions in atoms of certain materials, e.g. Helium and Neon (He-Ne). In a He-Ne laser electrons are transferred to a higher energy state by so called "pumping", e.g. applying energy to the atoms for example by light. After this transition the electron falls back to the lower energy level to minimize the energy level of the atom. During the transitions from upper to lower energy levels a photon is emitted whose amount of energy is exactly the difference between both energy states of the electron. *Spontaneous Emission* of photons occurs without excitation by pumping due to zero point fluctuations which is quantum-mechanically explained by the uncertainty principle, [6].

The pumping is used to create an electron population inversion, i.e. more alectrons are at the higher energy level compared to the lower level. Due to this inversion *Stimulated Emission*, which is caused by emitted photons, occurs and outweighs the spontaneous emission. Since the electron transition in this case is forced by an electromagnetic wave, the emitted photon[1] during the transition adds in phase to the incoming wave, has the same polarization and travels in the same direction, [22]. In order to increase amplification, a resonator is used that reflects the emitted radiation such that the emitted photons pass the gain medium multiple times. Usually mirrors are used to construct resonators for lasers in the visible wavelength range.

The properties of laser radiation should only briefly be mentioned here, detailed explanations of the following terms are given in [6]. Laser radiation has the following properties:

- It is *monochromatic*, i.e. it has a very narrowbanded spectrum resulting from the resonator arrangement where oscillation can only occur at the resonance frequency of the resonator.
- The emitted electromagnetic waves have a fixed temporal and spatial phase relation, i.e. the radiation is *coherent*.

[1] electromagnetic waves and photons are related by the wave-particle-duality (see [17] for details)

- A laser beam possesses optimal *collimation* compared to other radiation sources, i.e. an emitted laser beam hardly widens in diameter when travelling through space or passing an optical aperture.
- The *brightness* of laser sources is very high. It is defined as the power emitted per unit surface area per unit solid angle. Thus very high peak intensities in the focal plane of the laser can be achieved.
- The *pulse duration* of lasers can be very short ($\sim 10^{-14}$s for semiconductor lasers, [22])

Free electron lasers (FEL)

In conventional lasers the electrons are bound to atoms. This implies that usually only radiation with fixed wavelenght can be emitted because of the discrete energy states in the atom's structure. In a FEL on the contrary, the electrons are free and thus the emitted wavelength is tuneable because the energy of the emitted photons depends on the electrons' energy decay that can be nearly arbitrary for free electrons. The theoretical background of the FEL principle has been developed by John M.J. Madey in 1971. The first FEL has been realized at the Stanford University in 1977.

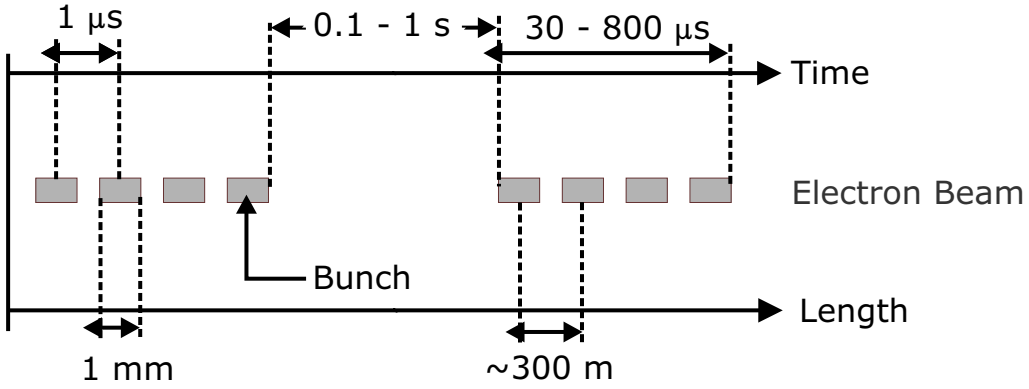

Figure 2.1: Temporal and spatial dimension of the pulsed electron beam

An FEL is considered a vacuum tube device: Its principle of operation is based on the interaction of an electron beam with radiation in vacuum, [19]. The basic structure of a FEL is shown in Figure 1.1. An *electron gun* emits a pulse train of electron clouds, so called *bunches* (see figure 2.1). The electrons are injected into a *linear accelerator*. The bunches enter the accelerator already with nearly the speed of light such that one bunch passes the whole accelerator structure before the next bunch is emitted a microsecond later. Technical aspects of linear accelerators will be discussed in chapter 2.2. Basically, the energy of the electrons is increased by the interaction with electromagnetic radio frequency fields (*RF-fields*) which are oscillating in superconducting resonator structures called *cavities* (see Figure 2.2). Because superconductivity can only occur at low temperature the cavities are housed in Helium cooled *cryomodules*. In the linear accelerator structure the electrons

are modulated in energy by *bunch compressors*. A simplified vivid explanation for this compression process is that slow electrons are accelerated and fast electrons are decelerated such that all microbunches have the same energy.

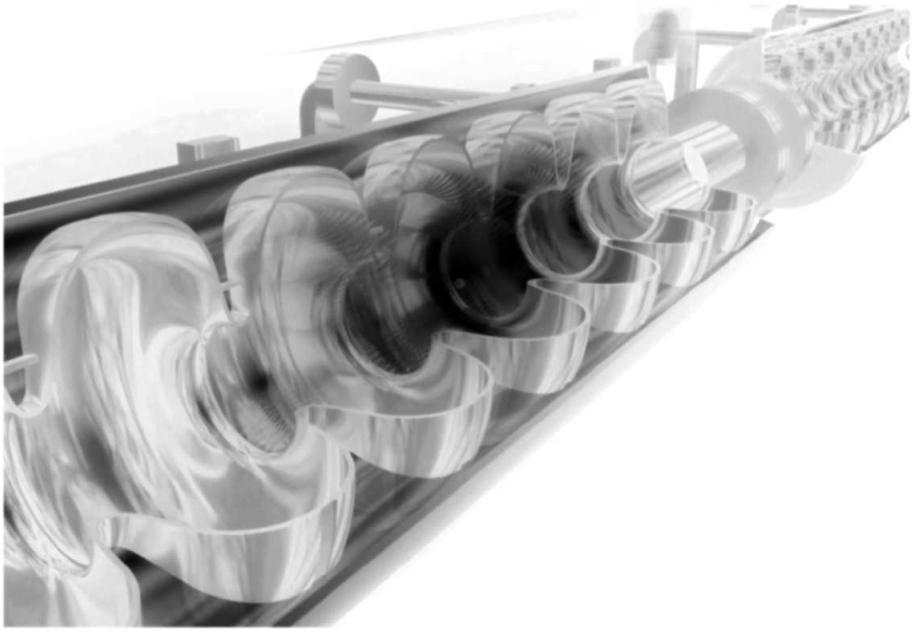

Figure 2.2: Visualization of RF-fields accelerating a particle in superconducting 9-cell cavities of the linear accelerator, [29]

After having passed the accelerator structure the electron beam is guided by beam optic systems called *collimators* into arrays of magnets called *undulators*. These magnets are arranged such that the electrons are forced onto sinusoidal (so called planar undulators) or helix shaped (so called helical undulators) trajectories. By the acceleration caused by the change of direction the electrons emit radiation pulses whose wavelength depends on the energy of the electron beam. Therefore the wavelength is tuneable by the field strength of the RF-fields in the linear accelerator. The *SASE* effect, which is explained in more detail in the next section, causes the electrons to emit their radiation synchronously. This leads to radiation that has the same properties like laser radiation. At the end of the undulators, the electrons are deflected by magnets into an electron trap. The emitted radiation is not affected by these magnets and travels further into an experimental area.

The properties of the emitted radiation by the X-ray FEL are specified for the year 2012 and include a wavelength of $\lambda_{XFEL} = 10^{-10}\,\mathrm{m} = 1\text{Å}$ and a pulse duration for each radiation pulse of $T_p = 10^{-13}$s. The brilliance of the coherent X-ray radiation is about factor 10^4 higher than that of conventional X-ray sources. With a wavelength in the Ångstrom range it becomes possible to optically inspect atoms because their radius is of the same order of magnitude.

SASE principle

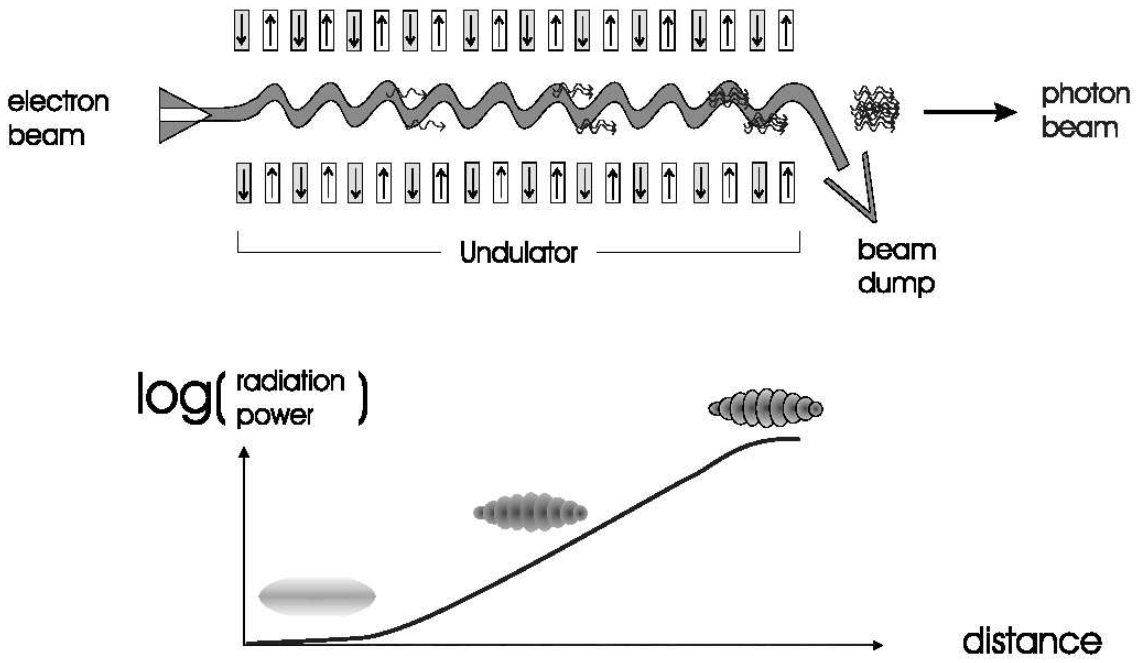

Figure 2.3: SASE principle and exponential increase of radiation power by electron microbunching

When the electron bunches enter the undulators, all electrons have the same energy. The electrons emit radition due to their acceleration by the no longer linear direction of motion. However, the electrons interact with the emitted radioation such that some the electrons receive energy of the radiation and other electrons submit energy to the radiation.

Thus, it comes to an effect called *microbunching*: The electrons formate spatially to groups where an energy exchange is no longer possible. The reason for this is that the energy of the electrons and the undulator period, i.e. the period the electrons' sinusoidal or helix shaped trajectory, are matched such that a resonance condition (see [1]) is fullfilled[2]. Electrons receiving energy of the radiation are accelerated and electrons submitting energy are decelerated until they have formed microbunches. Physically speaking microbunching is a longitudinal charge density modulation of the electrons, [18].

Due to microbunching the electrons emit radiation synchronously and the already emitted radiation is amplified. This effect is called *Self Amplified Spontaneous Emission (SASE)*. The radiation's electromagnetic waves have a defined phase relation because of the emission's synchronicity in time and space leading to coherence. The radiation power in the undulator grows exponentially with length because more and more electrons are ordered longitudinally in the undulator with increasing distance from the undulator entrance, [1].

[2]This resonance can be compared to the effect of the resonator structure at conventional lasers where mirrors are used to superimpose the laser light.

The phenomenon is in physical terms also called a "collective instability". The principle of the SASE effect and the exponential power increase is shown in Figure 2.3.

2.1.2 The DESY XFEL-Project

The XFEL-project is a european joint venture project to be realized at the Helmholtz facility DESY in Hamburg, Germany. Participating countries are France, Germany, Greece, Italy, Poland, Spain, Sweden, the United Kingdom and Switzerland. It is planned to construct an X-ray FEL using a 2.6km long linear accelerator. This extremely brilliant FEL light source should start operation in 2012. For the XFEL project synergy effects with the project *TESLA - Tera Electron Volt Superconducting Linear Accelerator* will be used, which besides supplying the electron beam for the XFEL should be operated as an electron-positron collider. The accelerators total energy is initially specified as 500GeV and will be extendable to 800GeV.

From 1992 to 2003 the fundamentals for free electron lasers operating in the X-ray wavelength range have been layed at the *TESLA Test Facility* (TTF) at DESY. At TTF, inital FEL experiments have shown that the challenging goals of the XFEL-project can be met. Now TTF has evolved to the next state (TTF2). At TTF2 an FEL is already operating in the ultraviolett wavelength range ($\lambda_{FEL} = 30$nm), the so called *VUV-FEL - Vacuum Ultraviolett FEL*. With the VUV-FEL, which is an about 300m long structure, coherent radiation with a wavelength less than $\lambda_{FEL} = 30$ nm has been produced. Gaining insight in the FEL technology with respect to the achievement of lower wavelength at TTF2 is the basis for the realization of the XFEL.

2.2 Linear accelerator

In the current construction state the linear accelerator at TTF2 is about 260m long. The acceleration of electrons is realized by superconducting Niobium cavities which are resonators for the RF-fields (see Figure 2.2). The acceleration process is further described in Section 2.2.1. The cavities are evacuated such that the accelerated electrons do not collide with air molecules. To enable the Niobium's superconductivity the cavities must be cooled to a temperature of $-271°$C. Superconductivity of the cavity walls leads to very low electrical energy dissipation and therefore lower temperature increase of the cavity walls compared to normalconducting cavities. Moreover, the cells of the cavities can be designed bigger which is an advantage because the influence of disturbance waves occuring when an electron bunch passes the RF-fields in the cell is reduced, [29]. The cavity walls have a low thickness of about 2.8mm to reduce the still present energy dissipation because of a finite electrical resistance. The thin walls however make the resonator structure susceptible to mechanical disturbances (see Section 2.2.5).

At TTF2 eight cavities are housed in each *cryomodule*, which is a cooling structure with

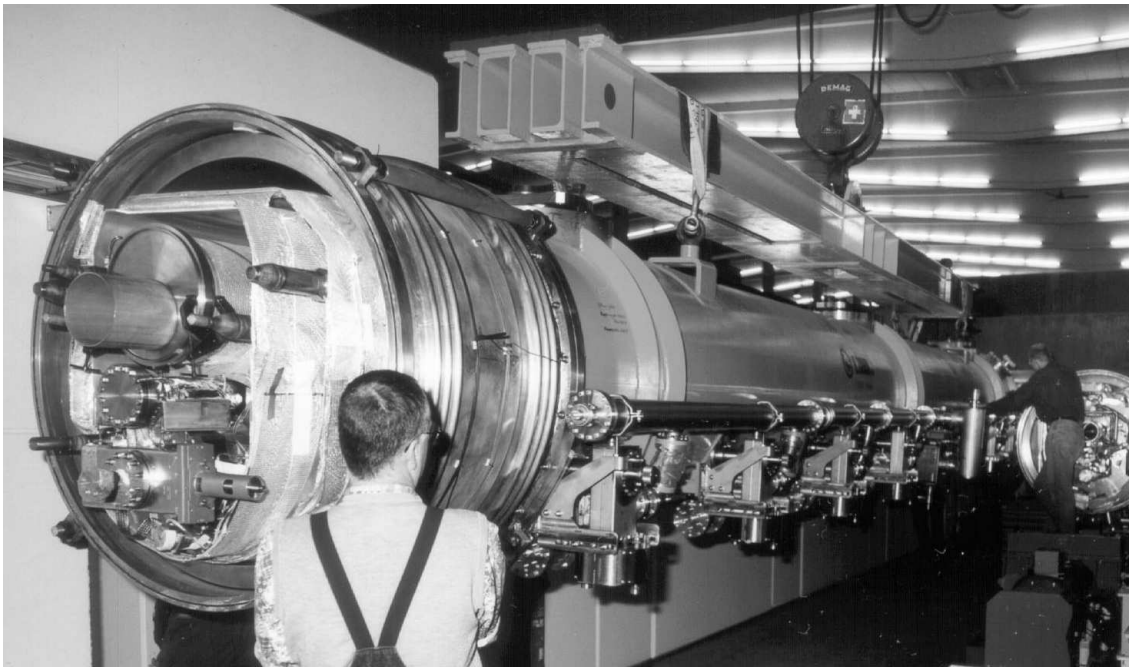

Figure 2.4: Assembly of a cryomodule at TTF2, DESY

pipelines of liquid Helium. In total six cryomodules are assembled at TTF2 such that the total number of cavities is 48, however in the current state only 40 cavities, i.e. five modules, are in operation. The system section in focus of this thesis is the first accelerator cryomodule, which will be abbreviated *ACC1*. During operation of the accelerator access to the tunnel is prohibited because of radiation emission on the one hand and because of magnets with high fieldstrength and high currents (> 200A) on the other hand.

2.2.1 Accelerating principle in superconducting cavities

The superconducting nine-cell cavities have nine electrical resonance modes (schematically shown in Figure 2.5). For the operation of TTF2 the cavities are driven in the so-called π-mode which is also called T_{M10} mode and has a resonance frequency of 1.3GHz. The bandwidth of the cavity is very narrow ($\omega_{1/2} = 2\pi \cdot 216.7$ rad/s) and the unloaded quality factor, which is a measure for the "sharpness" of the resonance peak, is very high (in the range of $Q_0 = 10^{10}$). These terms will be explained in detail in Chapter 4.

Driving the cavity in the π-mode means that the electromagnetic RF-waves with a frequency of 1.3 GHz form a standing wave inside the nine cavity cells and the fields in adjacent cells have a phase difference of $\phi = \pi\,\text{rad} = 180°$. The task of the RF-fields is to supply energy to the electron bunches of the electron beam by interaction. A very important point is that the electrons are already relativistic, i.e. they nearly travel with the speed c of light. when they enter the linear accelerator. In the acceleration process the energy of the electrons is

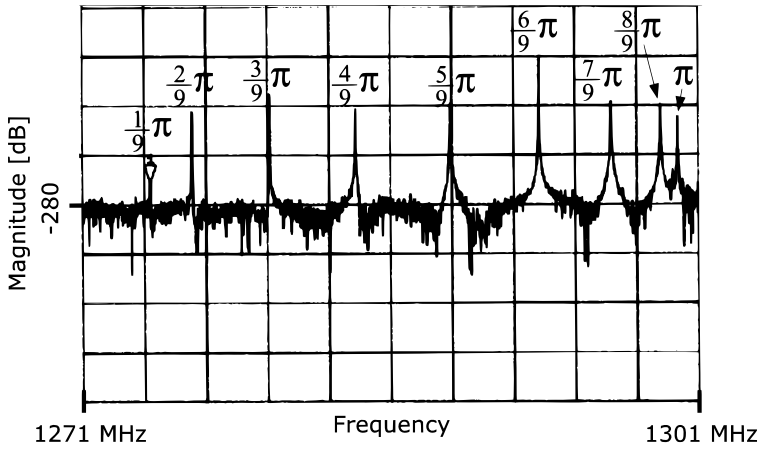

Figure 2.5: Electrical resonance modes of superconducting 9-cell cavities at TTF2, [20]

increased and the *relativistic* γ defined as

$$\gamma = \frac{1}{\sqrt{1 - \frac{v^2}{c^2}}}$$

increases when the magnitude of the electrons' velocity v asymptotically approaches c, [23].

The resonance frequency of the π-mode has been specified in the cavity design such that an electron bunch takes exactly half the resonance period of that mode to move from one cell to the next. In this time the field vector of the RF-field in the next cell has turned by 180°. If the injection time of the beam is adequately synchronized with the RF-fields, the electrons encounter in each cell an RF-field vector directed in the same direction as the cavity velocity vector $\boldsymbol{v}$. Therefore, the electrons are accelerated in the sense that they receive energy by the RF-fields. This process is shown in Figure 2.6.

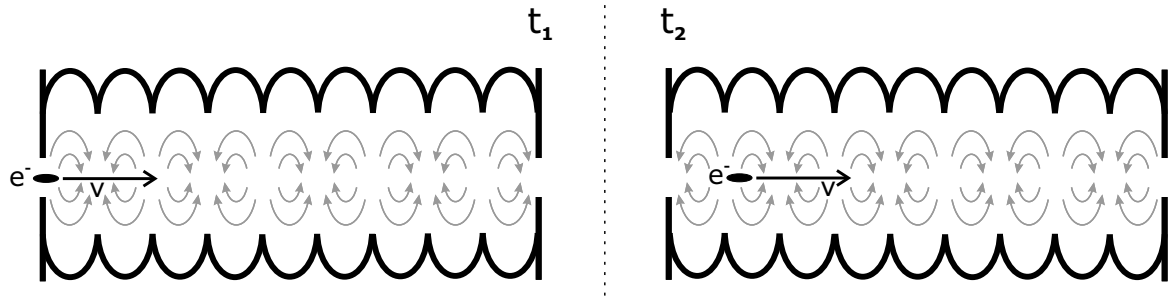

Figure 2.6: Acceleration principle of cavities driven in π-mode

2.2.2 System structure

Figure 2.7 shows one part, an *RF-station.* of the linear accelerator as planned for the XFEL and its so-called *Low Level Radio Frequency (LLRF)* control system. The LLRF control

system has the task to stabilize the pulsed RF-fields in the superconducting cavities of the RF-station during the flat top phase of one RF-pulse (see Figure 1.2).

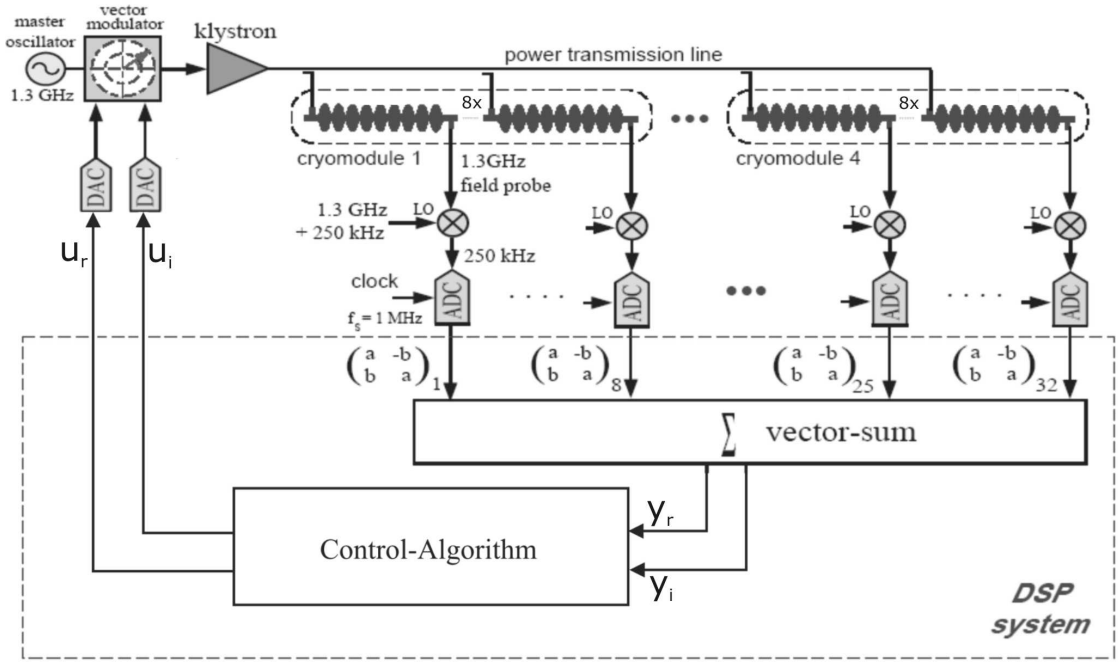

Figure 2.7: Scheme of the Low Level RF control system of one RF-station (here the planned scheme for the XFEL is shown, where one RF-station contains up to four cryomodules, i.e. 32 cavities)

A *klystron*, which is basically an amplifier for RF-waves (see Section 2.2.3), supplies the RF-fields for the number of cavities included in the RF-station. For the XFEL-project it is planned that one klystron supplies up to four cryomodules, each housing 8 cavities. At TTF2 however, one RF-station contains only up to two cryomodules, i.e. 16 cavities. The RF-station ACC1 of TTF2 which is focussed in this thesis contains eight cavities. The block diagram of ACC1 is shown in Figure 2.8. All signals are represented by means of their real and imaginary part[3]. The signal names are classified as follows:

- *Input signals* u_r,u_i: The sum of the control signals resembling the input signals of the actuator system, the vector modulator in particular.
- *Output signals* y_r,y_i: The real and imaginary part of the RF-field voltage vectors' sum of eight cavities. The vector sum signal is also called V_r and V_i.
- *Reference signals* r_r,r_i: The reference signals are given by tables in the signal processing system and specify the reference trajectories of the real and imaginary part of the vector sum of the RF-field's voltage vectors during an RF-pulse for the specified field gradient.

[3]In radio frequency theory and at DESY the real part of an RF-signal is also called *in-phase signal(I)* and the imaginary part *quadrature signal (Q)*. To avoid confusion, in this thesis the complex signals are denoted in real and imaginary part.

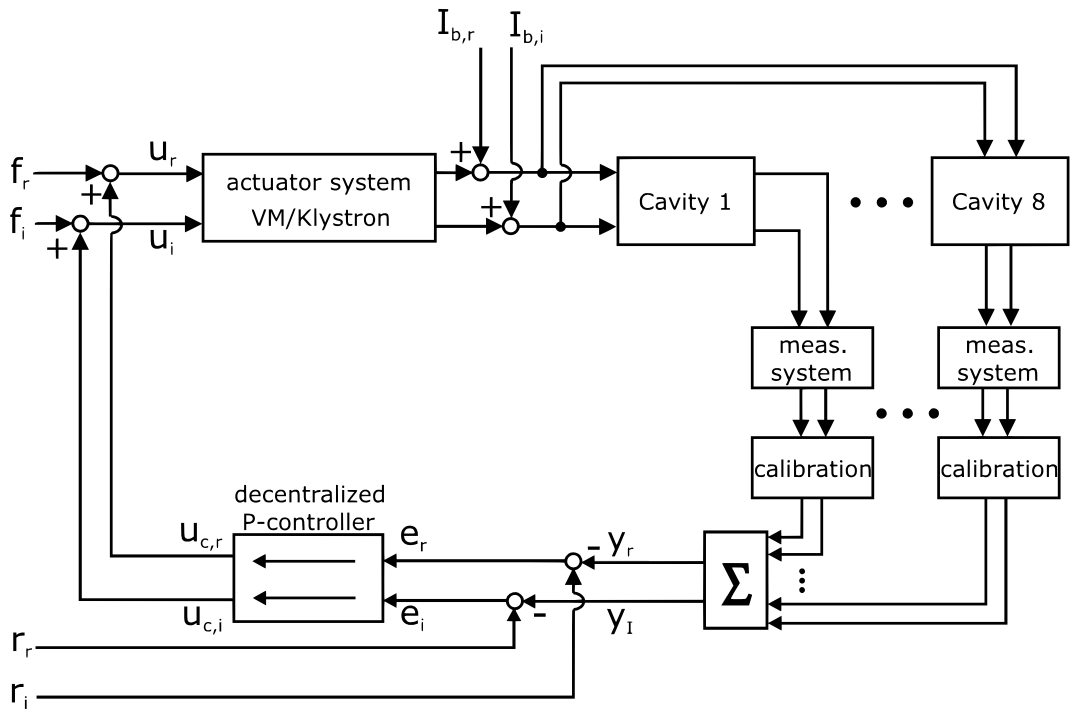

Figure 2.8: Block diagram of ACC1

- *Feedforward signals* f_r,f_i: The system is driven by the field forward signals that mark the input signals (u_r and u_i) in openloop.
- *Control signals* $u_{c,r}$,$u_{c,i}$: The feedback controller's output signals which are superimposed on the feedforward signals.
- *Electron beam current* $I_{b,r}$,$I_{b,i}$: Real and imaginary part of the electron beam current (see Chapter 4).
- *Control error signals* e_r,e_i: Deviations in real and imaginary part of the output signals from the reference signals.

2.2.3 Actuator system

The 1.3GHz RF-fields oscillating in the cavities are supplied by the actuator system consisting of a *vector modulator (VM)* and a *klystron*. This actuator system receives a stable RF-signal of 1.3 GHz from the *master oscillator (MO)*. This low power sinusoidal signal can be changed by the vector modulator in amplitude and phase. The output signal of the vectormodulator is amplified by a klystron, which is a radio frequency amplifier. A klystron consists of resonator structures for RF-waves as well. The term *LLRF-control system* thus denotes that the RF-fields are modulated in amplitude and phase on the low power side of the system before they are amplified and guided into the cavities by a transmission system.

The amplified RF-waves are transferred from the klystron to the cavities inside the cryomodules via a transmission system. The cable structures of this system are also called *waveguides*. Via *couplers* which are the connection between the waveguide and the cavity the RF-waves are injected into the cavities where they form a standing wave structure. The sinusoidal oscillation of a standing electromagnetic wave with a fixed frequency ω can be described by means of amplitude and phase or in the complex plane by the real and imaginary part of the field vector rotating with ω, [30].

Inside each cavity an antenna is assembled to measure the real and imaginary component of the RF-field vector oscillation. This measurement signal is transmitted to a digital signal processing (DSP) system. Signal processing of the masurement signals is described in Section 2.2.4.

Vector sum output signals

A very important point is that for economical reasons one high power klystron supplies all cavities of an RF-station with RF-fields: Providing a separate klystron for each cavity would be very expensive. The result is that it is not possible with this actuator system to influence the RF-fields real and imaginary parts (or amplitudes and phases respectively) in each cavity separately. Hence, the system is called *underactuated*. Therefore, the measurement signals of real and imaginary parts of all cavities contained in the RF-station are added in the DSP such that the real and imaginary part of the vector sum of the complex cavity field vectors are the variables to be controlled.

Dynamical behaviour of the actuating system

With respect to the operating frequency $f_{res} = 1.3\text{GHz}$ the vector modulator can be modelled as a first order low pass with a corner frequency of $f_{vm} = 10\text{MHz}$. The klystron is a high power RF-amplifier that can be considered as well as a first order lowpass filter with a corner frequency of $f_{kly} = 8\text{MHz}$. The bandwidths of both actuator elements are very large compared to the narrow cavity bandwidth $\omega_{1/2} = 2\pi \cdot 216.7\text{rad/s}$, and the dynamical behaviour of the accelerator system is neglectable in the frequency range considered (up to 100kHz) for control.

2.2.4 Measuring system

Downconversion and signal processing

The frequency of the RF-fields measured in each resonator is 1.3GHz. The LLRF system is a digital control system, i.e. all signals in the DSP involved in the control algorithm (measurement signals that are read in, control signals for the actuator system that are

written out of the DSP etc.) are processed at discrete time instants. The interval between those time instants is called the sampling time (see Chapter 3.1 for details).

Since it is impracticable to sample the highfrequent RF-fields for measurement directly, the 1.3GHz oscillation is *downconverted* to an intermediate frequency of 250kHz. This means that the signal is transformed to a signal with lower frequency by mixing it with a higher frequent signal of a so-called *Local Oscillator (LO)* and applying low pass filtering, [20]. To illustrate this, two sinusoidal signals are assumed:

$$V_{RF}(t) = \hat{V}_{RF} \cdot \sin(\omega_{RF} t + \varphi_{RF}) \,, \quad V_{LO}(t) = \hat{V}_{LO} \cdot \sin(\omega_{LO} t + \varphi_{LO})$$

The numerical values for the frequencies in this case are $\omega_{RF} = 2\pi \cdot 1.3 \cdot 10^9 \text{rad/s}$ and $\omega_{RF} = 2\pi \cdot 1.30025 \cdot 10^9 \text{rad/s}$. An ideal RF mixer operates as a multiplicator of two signals. Therefore, the output (intermediate signal) of the RF mixer for these two input signals is

$$\begin{aligned} V_{IF}(t) = \quad & \tfrac{1}{2} \quad \hat{V}_{RF}\hat{V}_{LO} \left(\cos\left((\omega_{LO} - \omega_{RF})t + (\varphi_{LO} - \varphi_{RF})\right)\right) \\ & - \quad \left(\cos\left((\omega_{LO} + \omega_{RF})t + (\varphi_{LO} - \varphi_{RF})\right)\right) \,. \end{aligned}$$

If a low pass filter is applied to remove the high frequency component of $V_{IF}(t)$ a signal $V(t)$ remains with a frequency that is the difference frequency of the input signals:

$$V(t) = \hat{V} \cos(\omega_{IF} t + \Delta\varphi)$$

with

$$\begin{aligned} \hat{V}(t) &= \frac{1}{2}\hat{V}_{RF}\hat{V}_{LO} \,, \\ \omega_{IF} &= \omega_{LO} - \omega_{RF} \,; \\ \Delta\varphi &= \varphi_{LO} - \varphi_{RF} \end{aligned}$$

The down-converted signal contains the information about amplitude and phase of the RF-signal if the amplitude and phase of the local oscillator is constant with respect to a master oscillator, [20]. In this case the intermediate frequency is $\omega_{IF} = 2\pi \cdot 2.5 \cdot 10^5 \text{rad/s}$. The intermediate signal is sampled with a sampling frequency of 1 MHz such that four samples per period are obtaines and Shannon's sampling theorem is fullfilled, (for further details see [16]). The conversion of the measurement signals is realized by analog to digital converters (ADCs) and the control signals for the vector modulator coming from the DSP are converted by DACs respectively. Detailled data about the signal processing system can be found in [20].

Calibration aspects

The measurement and control signals are transmitted by cables of different length which have capacitances, inductances and resistances. Therefore, the signals entering the DSP are modulated in amplitude and phase. For the control of the RF-fields it is however crucial

to have "true" measurement signals, i.e. to know what the values of amplitude and phase of the RF-fields inside the cavities are.

To compensate the modulations of the transmission system the measured RF-field vector of each cavity j is multiplied with an individual matrix $\boldsymbol{M}_j$ that implies a transformation involving a rotation and scaling of the vector. By the rotation the phase change shall be adjusted and by the scaling the amplitude change. This rotation and scaling matrix $\boldsymbol{M}_{cal}$ is denoted in Figure 2.7 as

$$\boldsymbol{M}_{cal} = \begin{pmatrix} a_j & -b_j \\ b_j & a_j \end{pmatrix}; \quad a_j, b_j \in \mathbb{R}. \tag{2.1}$$

Additional aspects of calibration involve a rotation of the measured vector sum itsself by an angle called *loop-phase* and a normalization of the open loop steady state gain by a factor called *system gain*:

- For physical reasons not further explained here the phase of the RF-fields' "true", i.e. perfectly calibrated, vector sum is zero at the beginning of each RF-pulse. If the measured vector sum differs at the beginning of the RF-pulse from zero, the vector sum is rotated by the angle called *loop-phase* to adjust the phase shift and to ensure that negative feedback is applied when the control loop is closed, [12].
- Each electrical component in the control loop has a static gain, i.e. an amplification factor of the input signals. In Section 2.2.6 the currently used control algorithm will be presented. The basic underlying control law is proportional feedback of the control error. During the evolution of TTF2 (electronic-) components in the loop are changed such that a different steady state gain of the open-loop system results. To ensure comparability of feedback gains applied at different construction stages, the open-loop steady state gain is normalized to one by multiplication with the *system gain* factor.

For further details on calibration see [20] and [12].

Consequences of calibration for control

It should be mentioned that calibration errors can have fatal effects on the closed loop system behaviour. An example is the loop phase that causes a rotation of the vector sum before the actual control error is computed: In the worst case a wrong loop phase can imply positive feedback of the control signal and thus an unstable closed loop system. At the present state of operation the calibration of the TTF2 system is usually only performed if major changes happened to the system, e.g. new components are installed. However, effects like temperature drifts can also change the system behaviour and should be taken into account for the calibration. Tools for online-calibration are developed at DESY and are partially already used.

For the model building the calibration of the focussed RF-station ACC1 of TTF2 has been assumed to be optimal. This assumption is reasonable because measurements at TTF2 have been made immediately after a new calibration of the system was done.

2.2.5 Disturbance sources

A multitude of disturbances decrease the quality of the laser beam. Here the focus is put on disturbances of the RF-fields inside the cavities. The cavities are resononators for standing RF-waves and their resonance frequency is determined by their geometry: If the length of the cavity changes, the resonance frequency changes as well. The problem is that due to the relatively thin cavity walls for low electrical energy dissipation, the resonators become susceptible for mechanical vibrations.

In Figure 2.5 the resonance modes of a cavity are shown. The quality factor Q (see Chapter 4) is defined as the quotient of resonance frequency and width of the resonance peak, which is two times the bandwidth $\omega_{1/2}$ of the resonator

$$Q = \frac{\omega_{res}}{2\omega_{1/2}} \,. \tag{2.2}$$

If the cavity is driven with a field gradient of 25MV/m at the resonance frequency of the cavities π-mode, the cavity bandwidth is $\omega_{1/2} = 2\pi \cdot 216.7\text{rad/s}$, [20]. The loaded quality factor (considering all energy losses while driving the cavity, see Chapter 4) is very high $Q_L \approx 3 \cdot 10^6$ and thus the resonant peak of the π-mode is very "sharp".

If the resonance frequency of the cavity's π-mode changes due to changes of the cavity's shape caused by mechanical vibrations, more power is needed to drive the cavity with the frequency of 1.3GHz. If this change in resonance frequency called *detuning* is in the order of the cavity bandwidth $\omega_{1/2}$ the drive power increases by 25%. Two main disturbance sources causing detuning are destinguished, *Microphonics* and *Lorentz Force Detuning*.

Microphonics

Mechanical vibrations caused by the accelerators environment are transferred by mechanical mounts to the cavities. The sources for microphonics are:

- System inherent sources: The vacuum pumps or the helium pums of the cryogenic system cause meachanical vibrations.
- Man-made: This can be vibrations caused by traffic or other human activity (sometimes also referred to as *cultural noise*) or machinery etc.
- Ground motions: Vibrations caused by seismic activities, ocean waves or elastic motion produced by the moon.

The typical frequency range for microphonics is below 1kHz. Therefore, microphonics can be considered a disturbance that only weakly influences the cavity fields during the 1.3ms long RF-pulse but mainly influences the resonance frequency from RF-pulse to RF-pulse. Microphonics can be considered as an uncorrelated disturbance.

Lorentz Force Detuning

The oscillating electromagnetic fields inside the cavities induce currents in the cavity walls. These currents lead to Lorentz forces acting on the cavity walls and deforming the cavities. The magnitude of the Lorentz forces is proportional to the square of the accelerating field gradients such that Lorentz force detuning can be considered as a correlated disturbance.

The frequency range of Lorentz Force detuning ranges up to 10kHz. In [20] it has been proposed that Lorentz force detuning can be considered repetitive from RF-pulse to RF-pulse. This will be further investigated in the modelling process (see Chapter 4). Approaches for modelling Lorentz force detuning are described in Chapter 4.2.

To reduce the effect of Lorentz force detuning two methods are used. The first is to stiffen the cavity section in between the cells by stiffening rings, i.e. a passive method of vibration reduction. The next method is still object of research. In [13] and [11] an approach to actively compensate the vibrations by piezo-actuators mounted on the cavity structure is proposed. The first experimental results with this active vibration control method have been very promising but this method is so far not regularly applied at TTF2.

Besides these mechanical disturbances further disturbances must be taken into account. These are noise produced by sensors and other electronic components, higher order electrical resonant modes of the cavities etc. .

In this thesis the influence of the electron beam on the RF-fields has not been taken into account. If this is done additional disturbances causing an energy spread like charge fluctuations of the electron bunches emitted by the electron gun will have to be considered.

2.2.6 Vector sum control algorithm

The currently used control algorithm at the LLRF system, a combination of decentralized proportional feedback and a feedforward component for both channels, is shown in Figure 2.9. Initially the vector sum signals are filtered by a digital low pass filter to remove sensor noise of the signals. In the present configuration the corner frequency of this filter is $f_{LP} = 220$ kHz.

The reference values for real and imaginary parts of the vector sum are listed in tables for each time step of the RF-pulse. These tables are scaled according to the specified

accelerating field gradient for the flat top.

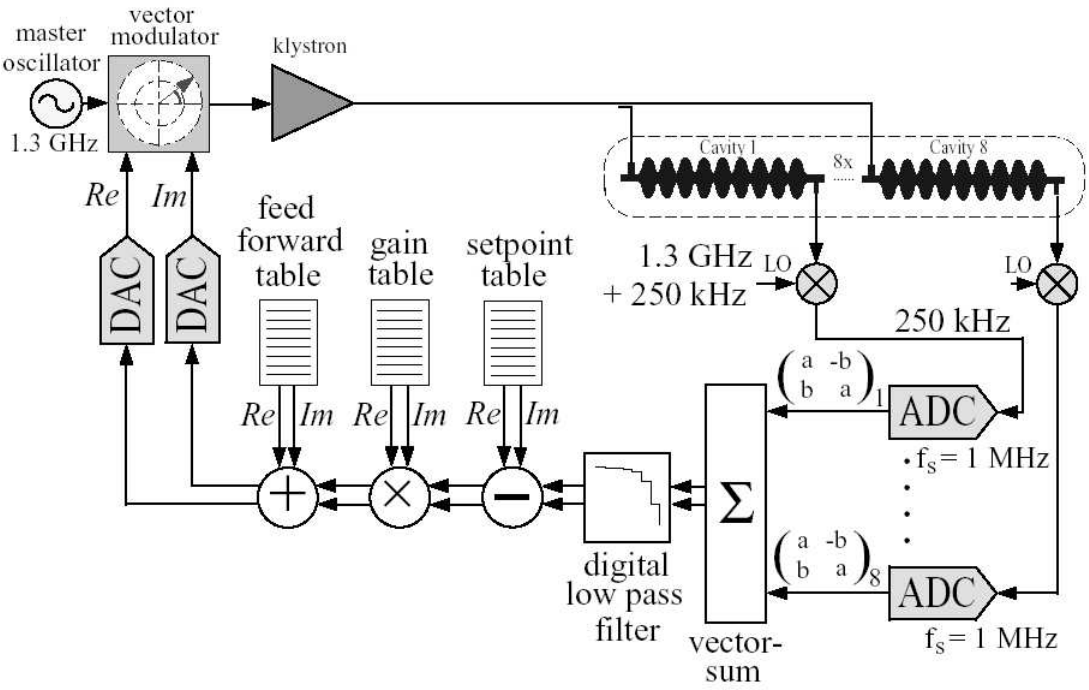

Figure 2.9: Currently used TTF2 control scheme for eight cavities

Proportional feedback

The currently used controller structure C_c is a decentralized proportional feedback. The errors in real and imaginary part of the vectorsum are multiplied with the same gain and no coupling between real input channel and imaginary output channel and vice versa are included in the controller structure. The discrete time transfer function matrix (see 3.1) of the digital P-controller has the following form

$$C_c(z) = K_p \cdot \begin{pmatrix} 1 & 0 \\ 0 & 1 \end{pmatrix} . \tag{2.3}$$

The controller structure will be discussed in more detail in chapter 6. In principle the DSP system provides gain tables for real and imaginary parts, i.e. not only different gains for both channels but also for different time steps can be used. However, so far no *gain scheduling techniques* (see section 3.1.2) for control have been used.

Feedforward tables

The feedforward signals are added on the output signal of the P-controller and are the input signals of the TTF2 system in open loop. Their levels are listed in tables in the DSP system and usually the signals are partwise constant for the phases filling, flat top and decay. A different feedforward table is used for the channels of real and imaginary signal. Thus one purpose of the feedforward tables is to provide the driving signals for the cavities such that the shape of the field amplitude during the RF-pulse shown in Figure 1.2 is approached even in open loop. Figure 2.10 shows controller output and feedforward signals in closed loop. It can be seen that the dominating parts of the plant input signals are the feedforward signals.

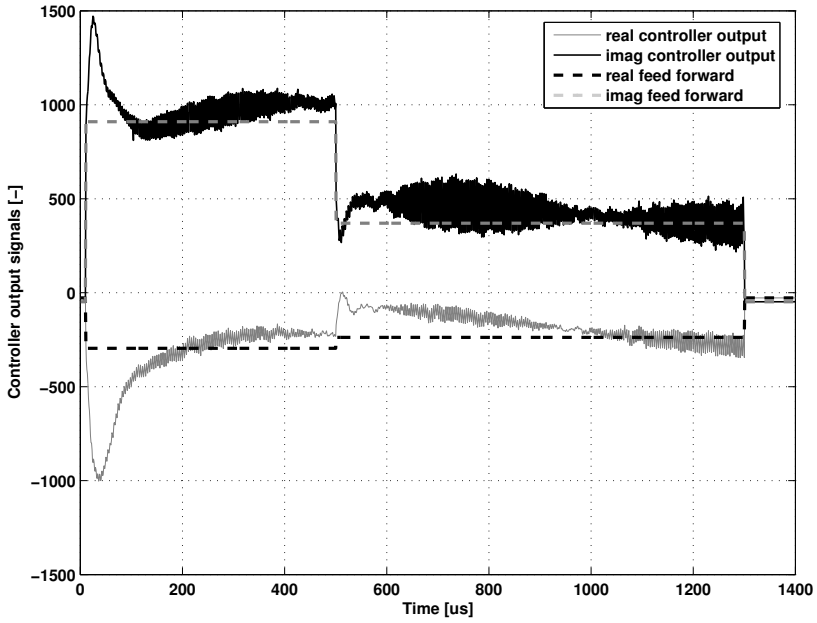

Figure 2.10: Controller output signals (u_r, u_i) and feedforward signals (f_r, f_i)

Moreover, attempts have been made to use the feedforward to compensate for so-called *beam induced transients*. Due to the acceleration of the electron beam, each electron bunch drains energy from the RF-fields in the cavities thus leading to a decay in amplitude everytime an electron bunch passes the cavity, which is called *transient*. Because the injection time of the beam is fixed at the begining of the flat top interval these repetitive disturbances can be compensated by use of feedforward control.

In [12] an approach is described to implement an adaptive feedforward algorithm that compensates the beam induced transients more efficiently by changing the feedforward tables iteratively in a learning fashion. However, this technique is not yet used regularly at TTF2 and uses non standard adaptation laws.

2.2.7 Control objectives for the XFEL

It has been shown in this chapter that the real and imaginary part of the vector sum of the RF-fields are the variables to be controlled. This is an equivalent formulation for controlling the vector sum in amplitude and phase. The real and imaginary parts of the feedforward signals are the input signals of the open loop system.

For the interaction of the electron beam with the RF-fields the amplitude and phase stability of the fields during the flat top phase of the RF-pulse is crucial (shown in Figure 1.2). Recalling the acceleration principle it is obvious that in the worst case for a phase deviation of 180° the electrons are maximally decelerated by the RF-fields[4]. In the formulation of the control objectives for the control error, which is the maximal acceptable deviations in amplitude and phase from the reference trajectories, the *rms-error* (root mean square error) and the *peak-to-peak error* is specified. These terms shall be defined using amplitude and phase for the description of the complex signals.

We define the reference trajectory for amplitude and phase as $r_a(t)$ and $r_\varphi(t)$ and respectively the vectorsum's amplitude and phase signals as $y_a(t)$ and $y_\varphi(t)$. The errors in amplitude ($e_a(t)$) and phase ($e_{phi}(t)$) are then given by

$$e_a(t) = y_a(t) - r_a(t) \quad e_\varphi(t) = y_\varphi(t) - r_\varphi(t)\,. \tag{2.4}$$

Considering $e_{a,f}(t)$ and $e_{\varphi,f}(t)$ the error values for the $T_f = 800\mu$s samples long flat top interval beginning at sample $t_{0,f}$ and respectively $r_{a,f}(t)$ and $r_{\varphi,f}(t)$ the constant reference values during this interval the peak-to-peak control error for the flat top interval is defined as follows

$$e_{a,p2p} = \frac{|\max(e_{a,f}(t)) - \min(e_{a,f}(t))|}{|r_{a,f}|}\,, \quad e_{\varphi,p2p} = \frac{|\max(e_{\varphi,f}(t)) - \min(e_{\varphi,f}(t))|}{|r_{\varphi,f}|}\,. \tag{2.5}$$

The rms-error for the flat top interval is defined as

$$e_{a,rms} = \sqrt{\frac{1}{T_f} \cdot \int_{t_0}^{t_{0,f}+T_f} e_a^2 dt}\,, \quad e_{\varphi,rms} = \sqrt{\frac{1}{T_f} \cdot \int_{t_0}^{t_{0,f}+T_f} e_\varphi^2 dt}\,. \tag{2.6}$$

The specified control objectives regarding the RF-field stability for the XFEL project to be successful are the following:

[4]If *on-crest* acceleration is assumed, i.e. the injection of the electron is done when the phase difference between RF-field vector and electron velocity vector is 0°

Control objectives for the XFEL's RF-field stability of the vector sum:
During the flat top interval of each RF-pulse the control errors in amplitude and phase of the vector sum must be within the following tolerances:

- Peak to peak amplitude precision: $e_{a,p2p} \leq 0.1\%$.
  RMS amplitude precision: $e_{a,rms} \leq 0.01\%$.
- Peak to peak phase precision: $e_{\varphi,p2p} \leq 0.1°$.
  RMS phase precision: $e_{\varphi,rms} \leq 0.01°$.

A further control objective not directly concerning the RF-fields is the minimization of the RF-field driving power. Reducing the detuning e.g. by active vibration control with the piezo actuators, which is a topic of research at TTF2, is one important aspect to deal with the multiobjective goals.

The current status achieved with the decentralized proportional feedback and feedforward is $e_{a,p2p} \approx 0.5\%$, $e_{\varphi,p2p} \approx 1°$, $e_{a,rms} \leq 0.1\%$ and $e_{\varphi,rms} \approx 0.1°$. The control error must be lowered by approximately one degree of magnitude to fullfill the control objectives for the XFEL.

2.2.8 Actuator constraints

An issue that must be considered for high performance controller design are limitations of the actuator system. Due to physical constraints on input and output signal levels of the actuators the controller signals which are the input signals of the plant can not be of arbitrary large magnitude. In case of TTF2 the main actuator constraint results from limited klystron output power.

The values of the feedforward signals for each sampling instant are saved in tables contained in the DSP system and are normalized such that their maximal value is one. These tables are called *feed forward reference tables*. The tables are then automatically scaled depending on the RF-field gradient specified for the vector sum of the accelerator module's cavity voltages. In Figure 2.11 the trajectories of the input signals u_r and u_i of the actuator system are shown which resemble the feedforward signals (f_r and f_i) in openloop. They have been generated by the feedforward reference tables by scaling such that a field gradient of 14MV/m is obtained.

It has been experimentally found out that the real and imaginary parts of the closed loop input signals of the actuator system can maximally have twice the maximal values of the feedforward signals of the respective signal. The maximal values may only occur for approximately 2-4 samples. The "usual" values of the input signals should be in the level range of the feedforward signals such that the rms-value of the feedback control signals

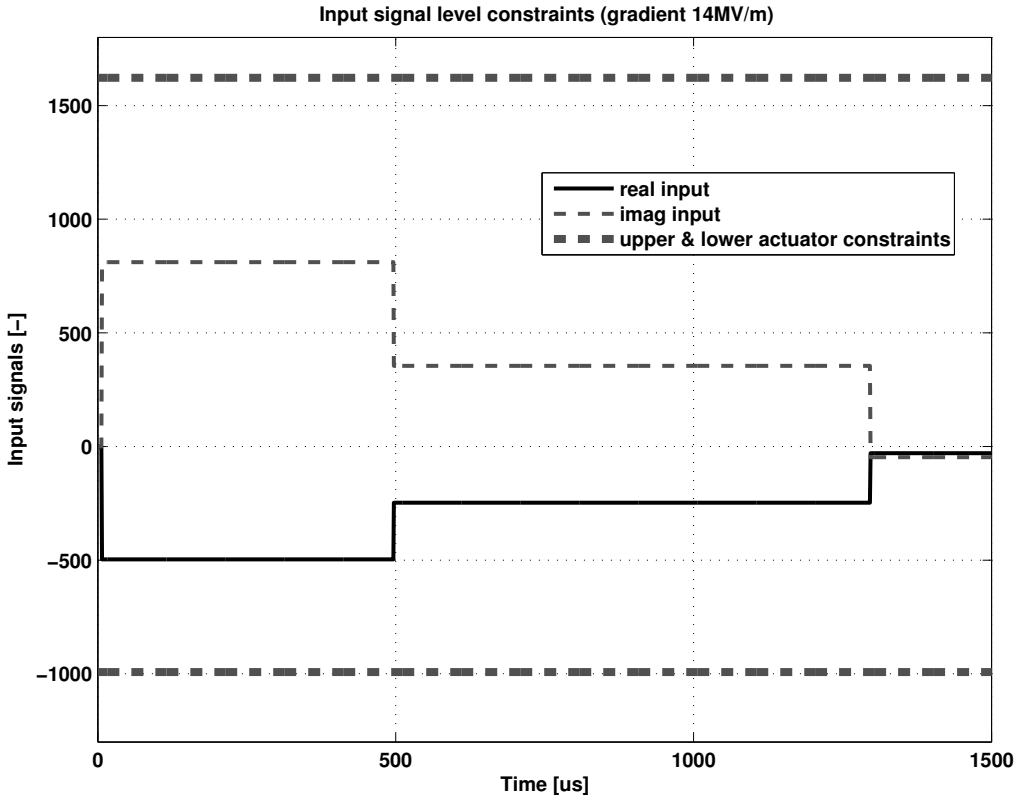

Figure 2.11: Actuator constraints for a field gradient of 14MV/m

are low compared to the rms-values of feedforward control signals. A precise mathematical formulation of actuator constraints is not possible because of lack of detailled technical specifications for the actuators. The mentioned constraints have however been taken into account for experiments at TTF2 in order not to damage the system.

Chapter 3

Methods for modelling of system dynamics

In general, a dynamic system can be described by its input/output (I/O) behaviour. A set of time varying signals are considered as inputs of the system that cause internal variables (*states*) to change. A subset of measured signals is considered as outputs. The purpose of a model of the system is to describe the process inherent mapping from the input signals onto the output signals.

In order to meet the severe control objectives for the field stability of the superconducting cavities for the XFEL the VUV-FEL is constantly optimized technically. A part of this evolution is planned to be the development of a more sophisticated controller than a proportional feedback. Methods for the synthesis of high performance controllers are model based. Unlike heuristic tuning methods used to obtain controller parameters e.g. with only one characteristic response of the plant used as a model, the dynamics of the system's mathematical model are resembled in the high performance controller structure. As a result it is necessary to develop an appropriate model of the low level RF system to be able to make use of this methods. An overview on two analytical model structures (linear time invariant models and linear parameter varying models) is given in section 3.1.

Of course, it is not possible to describe the behaviour of the real-life system by a model in all details, i.e. for every operating condition. Therefore one has to focus on a set of situations that should be described by the model. Examples for constraints resulting from special situations are frequency ranges or levels of operation for the input and output signals.

This chapter describes two different ways of modelling a dynamic sytem: The modelling by first principles based on physical insight into the system dynamics and an experimental based way of modelling, the *system identification*. The system to be modelled is the low level radio system of the the first linear accelerator section (ACC1) of the VUV-FEL at TTF2. The main focus is the behaviour of the superconducting cavities. In section 3.2 modelling by first principles is discussed and in chapter 4 the techniques are applied to

model superconducting cavities.

The system identification process is described in section 3.3. Especially the choice of input signals and a method to parametrize a model structure based on experimental data is illustrated (see 3.3.4). In chapter 4 the resulting models of system identification of ACC1 are presented.

3.1 Model structures

The system or plant structure and its application for the process that should be described by the mathematical model lead to a certain model type. Model types can be classified by attributes like linear/nonlinear, time invariant/time variant, models with concentrated/distributed parameters etc.. In this thesis two model types are used: Linear Time Invariant (LTI) models and Linear Parameter Varying (LPV) models. LTI models are the most frequently used models for controller design because their analysis is relatively simple compared to more complex model structures. For a lot of control applications the plant behaviour can be described by an LTI model accurately enough because often the nonlinear behaviour will be approximated by local linearized models for an operating point of interest. A variety of controller design methods for LTI models have been established by now. LPV models contain time varying parameters and are more complicated to analyse. Controllers for LPV models are often *scheduled*, i.e. the controller parameters are adjusted over time to meet the alterating plant dynamics.

Generally speaking the model structures that are dealt with in this thesis can be characterized by a finite number of parameters and are therefore called *parametric models*. The frequency response or the impulse response of a dynamical system are models for the plant behaviour as well but can not be characterized by a finite number of parameters and are hence called *nonparametric models*, [28].

3.1.1 Linear time invariant models (LTI)

The I/0 behaviour of LTI models is linear and the model parameters do not vary over time. In the following description of some LTI model structures the focus is put on discrete time models. In modern digital control, measuring of system output signals and applying actuator signals on the plant takes place at equidistant time intervals, the sampling instants. Continuous time models and the conversion between discrete and continuous time LTI models is only discussed briefly. For a more detailed presentation of this topic see e.g. [16].

Figure 3.1: System with input and output signals

ARX models

Considering a process with one input signal $u(t)$ and one output signal $y(t)$ (see figure 3.1) a simple relationship between the actual output at time t and the past input and output values is a linear difference equation. If the application of the inputs and the measurement of the output only takes place at discrete time instants

$$t = kT \tag{3.1}$$

with T as sampling time and k as the index of the samples, the linear difference equation can be written as

$$\begin{aligned} y(kT) &+ a_1 y(kT-T) + a_2 y(kT-2T) + \cdots + a_n y(kT-nT) \\ &= b_1 u(kT-T) + b_2 u(kT-2T) + \cdots + b_m u(kT-mT)\,. \end{aligned} \tag{3.2}$$

If a normalized unitfree sampling time of $T = 1$ is assumed, eq.(3.1) becomes $t = k$ and this can be substituted in eq.(3.2) as follows

$$\begin{aligned} y(k) &+ a_1 y(k-1) + a_2 y(k-2) + \cdots + a_n y(k-n) \\ &= b_1 u(k-1) + b_2 u(k-2) + \cdots + b_m u(k-m)\,. \end{aligned} \tag{3.3}$$

An important assumption in eq.(3.3) is that the system is not corrupted by any form of noise (process noise or measurement noise). If an output disturbance is present the disturbance term $d(t)$ has to be added to the right hand side of eq.(3.3) (see the description about *output error models* at the end of this section for more details).

The described model structure contains an *AutoRegressive* part (the past outputs) and *eXogeneous* inputs (the system excitation by the input signals). Such a structure is called *ARX* model.

State space models

Equation (3.3) can be transformed into an equivalent representation in discrete time domain, the state space model. To obtain the actual value of the output signal at the sampling instant k the last n output samples and the last m input signal samples must be known. Introducing new variables x_j called *states*

$$x_1(k) = y(k-n)\,,$$

$$
\begin{aligned}
x_2(k) &= y(k-n+1)\,, \\
&\cdots \\
x_n(k) &= y(k-1)
\end{aligned}
$$

and substituting for the output values state variables

$$
\begin{aligned}
x_1(k+1) &= x_2(k)\,, \\
x_2(k+1) &= x_3(k)\,, \\
&\cdots \\
x_{n-1}(k+1) &= x_n(k)
\end{aligned}
$$

leads to the following relation for the last state space variable

$$
\begin{aligned}
& x_n(k+1) = y(k) \\
\Leftrightarrow \quad & x_n(k+1) = [b_1 \quad b_2 \cdots b_m] \begin{bmatrix} u(k-1) \\ u(k-2) \\ \cdots \\ u(k-m) \end{bmatrix} - \sum_{i=1}^{n} a_i y(k-i) \\
\Leftrightarrow \quad & x_n(k+1) = [b_1 \quad b_2 \cdots b_m] \begin{bmatrix} u(k-1) \\ u(k-2) \\ \cdots \\ u(k-m) \end{bmatrix} - \sum_{i=0}^{n-1} a_{i+1} x_{n-i}(k) \quad . \qquad (3.4)
\end{aligned}
$$

Assuming $n = m$, eq.(3.4) can be written in matrix format (for a detailed deduction see [15],[16]) using the following matrices:

$$
\boldsymbol{A} = \begin{pmatrix} 0 & 1 & 0 & \cdots & 0 \\ 0 & 0 & 1 & \cdots & 0 \\ \vdots & \vdots & \vdots & \ddots & \vdots \\ 0 & 0 & 0 & \cdots & 1 \\ -1 & -a_1 & -a_2 & \cdots & -a_{n-1} \end{pmatrix}, \qquad (3.5)
$$

$$
\boldsymbol{b} = \begin{pmatrix} 0 \\ 0 \\ \vdots \\ 1 \end{pmatrix}, \qquad (3.6)
$$

$$
\boldsymbol{c'} = (-b_n, b_1 - b_n a_1, \ \ldots \ , b_{n-1} - b_n a_{n-1})\,, \qquad (3.7)
$$

$$
d = b_n\,. \qquad (3.8)
$$

The state space model form for a single input single output system then becomes

$$
\begin{aligned}
\boldsymbol{x}(k+1) &= \boldsymbol{A}\boldsymbol{x}(k) + \boldsymbol{b}u(k)\,, \\
y(k) &= \boldsymbol{c'}\boldsymbol{x}(k) + du(k)\,, \qquad (3.9) \\
\boldsymbol{x}(0) &= \boldsymbol{x}_0\,.
\end{aligned}
$$

where $\boldsymbol{x}_0$ denote the initial state of the system. An important point is that the state space representation of a system is non-unique: The states of a system are internal variables that need not have any physical meaning and can be choosen convenient for the modelling procedure. By using similarity transforms a new basis for the state space can be generated. For a detailed description of these transformations, see [15]. A state space model whose matrices have the structure shown in eq.(3.5) - (3.8) is called to be in the *controllable standard form*. Transfer functions on the contrary are a unique description of a dynamical system and will be presented in this section as well.

If the system is multivariable, i.e it has q inputs ($\boldsymbol{u}(t) \in \mathbb{R}^q$) and r outputs ($\boldsymbol{y}(t) \in \mathbb{R}^r$), the dimensions of the matrices become $\boldsymbol{A} \in \mathbb{R}^{n\times n}$, $\boldsymbol{B} \in \mathbb{R}^{n\times q}$, $\boldsymbol{C} \in \mathbb{R}^{r\times n}$, $\boldsymbol{D} \in \mathbb{R}^{r\times q}$ such that the state space model for a multivariable system is given by

$$\begin{aligned} \boldsymbol{x}(k+1) &= \boldsymbol{A}\boldsymbol{x}(k) + \boldsymbol{B}\boldsymbol{u}(k)\,, \\ \boldsymbol{y}(k) &= \boldsymbol{C}\boldsymbol{x}(k) + \boldsymbol{D}\boldsymbol{u}(k)\,, \\ \boldsymbol{x}(0) &= \boldsymbol{x}_0\,. \end{aligned} \tag{3.10}$$

Transfer functions

If a discrete time domain signal $x(k)$ should be transformed into frequency domain the z-transform can be used which is defined as follows

$$\mathcal{Z}[x(k)] = X(z) = \sum_{k=0}^{\infty} x(k) z^{-k}\,. \tag{3.11}$$

The relation between the complex variable z and the complex variable s used in the Laplace-transformation is

$$z = e^{sT}\,. \tag{3.12}$$

Taking the z-transform of both sides of eq.(3.3) and factoring out the transformations of the input and output signals yields

$$Y(z)\cdot(1 + a_1 z^{-1} + a_2 z^{-2} + \cdots + a_n z^{-n}) = U(z)\cdot(b_1 z^{-1} + b_2 z^{-2} + \cdots + b_m z^{-m})\,. \tag{3.13}$$

The discrete time transfer function $G(z)$ is defined as

$$G(z) = \frac{Y(z)}{U(z)} = \frac{b_1 z^{-1} + \ldots + b_m z^{-m}}{1 + a_1 z^{-1} + \ldots + a_n z^{-n}} \quad . \tag{3.14}$$

The transfer function in eq.(3.14) has m zeros and n poles[1]. As already discussed in the previous subsection a transfer function is a unique description of a dynamical system. In case of a multivariable system with q input channels and r output channels a frequency domain representation of the system is the transfer function matrix $\boldsymbol{G}(z) \in \mathbb{R}^{r\times q}$. For a

[1]The zeros and poles of course characterize the behaviour of the model but a detailed classification of transfer functions according to poles and zeros is omitted here. In literature on control theory basics like [15] and [16] this classification is thoroughly discussed.

given state space representation of a model a conversion into the systems transfer function is

$$\boldsymbol{G}(z) = \boldsymbol{C}(zI - \boldsymbol{A})^{-1}\boldsymbol{B} + \boldsymbol{D}\,. \tag{3.15}$$

Parametric LTI models in continuous time domain

The models presented up to now are expressed in *discrete time*, i.e. the models describe the system behaviour for each sampling instant defined by eq.(3.1). If the system behaviour should be described in *continuous time* differential equations and continuous time state space models can be used.

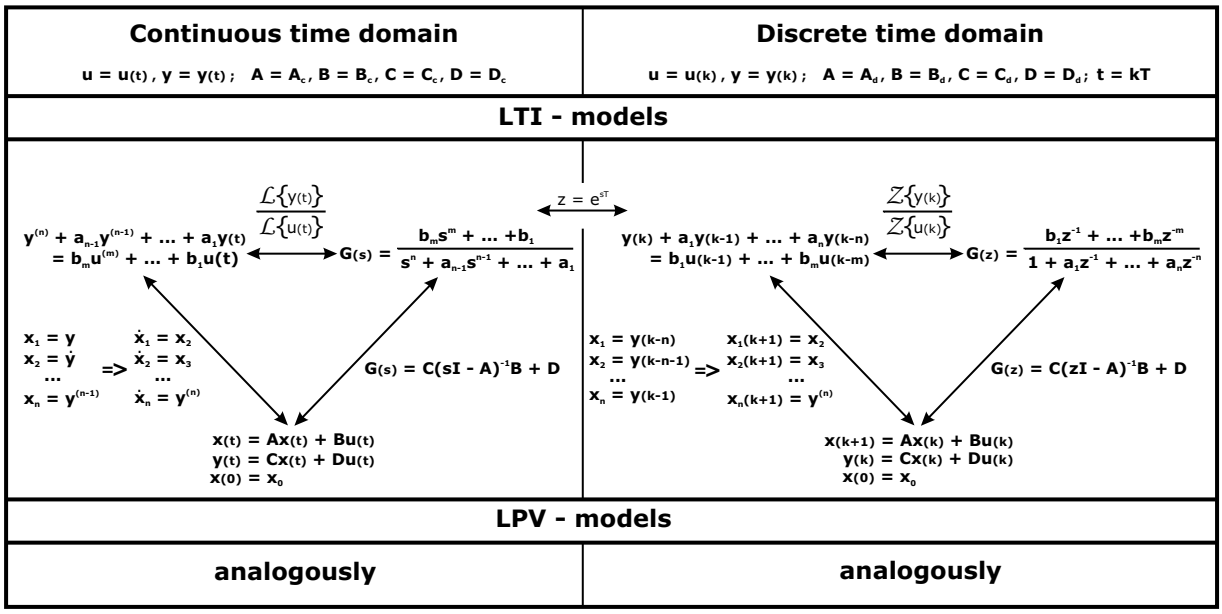

Figure 3.2: Models for LTI and LPV systems and their conversions

The linear differential equation

$$y^{(n)}(t) + \cdots + a_1\dot{y}(t) + a_0 y(t) = b_m u^{(m)}(t) + \cdots + b_1\dot{u}(t) + b_0 u(t) \tag{3.16}$$

describes a single input single output (SISO) system in continous time. The values of the coefficients of eq. (3.16) however are usually not the same as in eq. (3.3).

In [15] a rigorous deduction of the equivalent continuous time state space model can be found which has the structure

$$\begin{aligned} \boldsymbol{x}(t) &= \boldsymbol{A}_c\boldsymbol{x}(t) + \boldsymbol{b}_c u(t)\,, \\ y(t) &= \boldsymbol{c'}_c\boldsymbol{x}(t) + d_c u(t)\,, \\ \boldsymbol{x}(0) &= \boldsymbol{x}_0\,. \end{aligned} \tag{3.17}$$

with the matrices

$$\boldsymbol{A}_c = \begin{pmatrix} 0 & 1 & 0 & \cdots & 0 \\ 0 & 0 & 1 & \cdots & 0 \\ \vdots & \vdots & \vdots & \ddots & \vdots \\ 0 & 0 & 0 & \cdots & 1 \\ -a_0 & -a_1 & -a_2 & \cdots & -a_{n-1} \end{pmatrix}, \tag{3.18}$$

$$\boldsymbol{b}_c = \begin{pmatrix} 0 \\ 0 \\ \vdots \\ 1 \end{pmatrix}, \tag{3.19}$$

$$\boldsymbol{c'}_c = (b_0 - b_n a_0, b_1 - b_n a_1, \ldots, b_{n-1} - b_n a_{n-1}), \tag{3.20}$$

$$d_c = b_n . \tag{3.21}$$

The state space model in eq.(3.17) is again presented in the controllable normal form. For multivariable systems the continuous state space system has the following form

$$\begin{aligned} \boldsymbol{x}(t) &= \boldsymbol{A}_c\boldsymbol{x}(t) + \boldsymbol{B}_c\boldsymbol{u}(t), \\ \boldsymbol{y}(t) &= \boldsymbol{C}_c\boldsymbol{x}(t) + \boldsymbol{D}_c\boldsymbol{u}(t), \\ \boldsymbol{x}(0) &= \boldsymbol{x}_0 . \end{aligned} \tag{3.22}$$

The matrices of eq.(3.22) have the same dimensions as the state space matrices of eq.(3.10) if again q inputs and r outputs are considered. In the following the indices for the state space matrices are omitted although discrete time and continuous time state space matrices are not equal. The context of the following chapters however should make clear if discrete or continuous time state space matrices are meant.

An overview on the models for LTI and LPV systems is shown in figure 3.2. Presented are only parametric models because they are mainly focussed on in the model building procedures in this thesis. The models of LPV systems, which are described in more detail in section 3.1.2, can be structured analogously to LTI models.

Disturbance sources and parameter disturbance input

The models presented so far do not include any kind of disturbances or noise. Their absence is an unlikely case because in real systems every electronic component induces noise on the signal it transmits and mechanical components are excited by environmental vibrations. These disturbances lead to unwanted signal behaviour and are one of the main reasons why feedback control is applied.

It has to be specified for the disturbances where they enter into the control loop (see Figure 3.3). *Output Disturbances* $d(t)$ like vibrations changing a position to be controlled are superimposed on the plant output signal $y(t)$. *Measurement noise* $n(t)$ is caused by the sensor elements that measures the output signals for inducing feedback, [15].

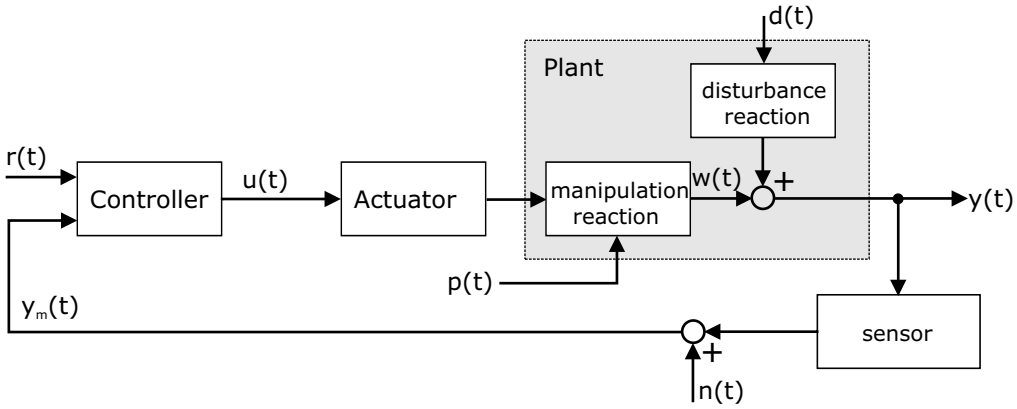

Figure 3.3: Control loop structure with disturbances

Another type of disturbance used in this thesis for modelling the detuning of the superconducting cavities (see section 4.2) is a *parameter disturbance input* $p(t)$. This disturbance signal changes the parameter of the plant continuously.

Output error model structure

A model used for the parameter estimation of the system identification process (see section 3.3.4) is the *output error (OE) model*. In the ARX model presented in section 3.1.1 it was first assumed that the plant's output signal is not currupted by any disturbance. If this assumption is removed the output signal of the plant results from the sum of the undisturbed output $w(t)$ and the disturbance $d(t)$ as shown in Figure 3.4, [14]:

$$\begin{aligned} y(t) &= w(t) + d(t) \\ &= \frac{B(z)}{F(z)} u(t) + d(t) \end{aligned} \tag{3.23}$$

Equation (3.23) is given in time domain because in this context z is the *forward shift operator* defined by

$$zu(t) = u(t+1) \qquad , \tag{3.24}$$

not to be mistaken for the complex variable z of the z-transform

The function $H(z) = \frac{B(z)}{F(z)}$ consists of the polynomials $B(z)$ and $F(z)$ in the forward shift operator z. We assume that the polynomial coefficients of $H(z)$ characterizing the mapping from $u(t)$ into $w(t)$ are not exactly known but shall be identified based on input/output data, and introduce the parameter vector containing the coefficients of $H(z)$ as

$$\theta = [b_1 \quad b_2 \ldots b_m \quad f_1 \quad f_2 \ldots f_n] \,. \tag{3.25}$$

The polynomial $B(z)$ is assumed to be of order m while $F(z)$ is assumed to be of order n. In an OE model, a model structure $\hat{H}(z) = \frac{\hat{B}(z)}{\hat{F}(z)}$ of the same order in numerator and

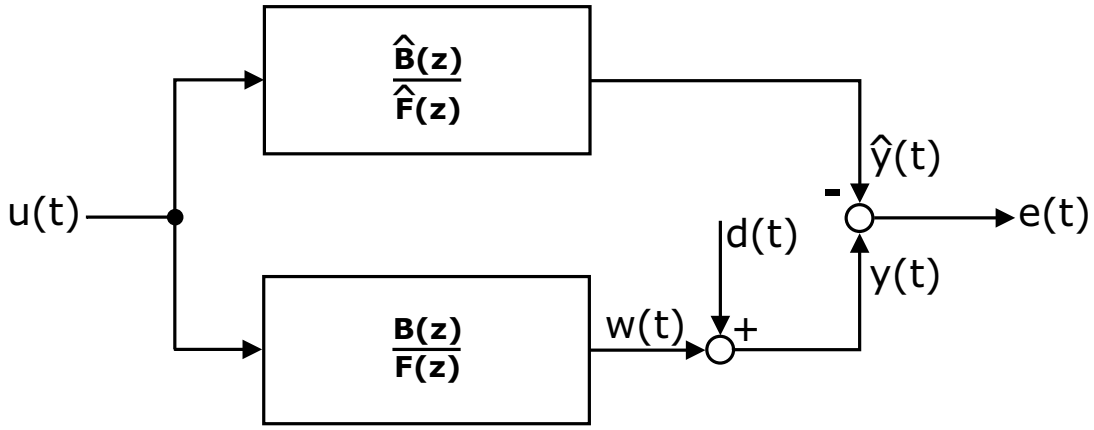

Figure 3.4: Output error model structure

denominator as $H(z)$ is connected in parallel to the model $H(z)$, i.e. the same input data enters both models. The goal of this structure is to adjust the parameters of $H(z)$ such that the output error

$$e(t) = y(t) - \hat{y}(t) \tag{3.26}$$

is minimal with respect to a certain criterion (usually formulated as an error functional). OE model structures are used in *system identification*. The aspects of parameter estimation and a criterion regarding the minimization of $e(t)$ are presented in detail in section 3.3.

The undisturbed plant output $w(t)$ of the plant can be constructed from the difference equation

$$\begin{aligned} & w(t+n,\theta) + f_1 w(t+n-1,\theta) + \ldots + f_n w(t,\theta) \\ = \;& b_1 u(t+m-1) + \ldots + b_m u(t)\,. \end{aligned} \tag{3.27}$$

Because in this case $d(t) = 0$, the plant output be reproduced by $H(z)$ if $\hat{H}(z)$ is parametrized with θ such that

$$w(t) = \frac{B(z)}{F(z)} u(t) = \hat{y}(t|\theta) \tag{3.28}$$

where $\hat{y}(t|\theta)$ is the so-called *natural predictor* of the real plant output, [14].

3.1.2 Linear parameter varying models (LPV)

A possible way of designing controllers for nonlinear systems is to linearize the system with respect to different operating points and use a linear controller for each of them. By switching between the controllers obtained in this way, the overall controller results for the approximated system. This technique is called (linearized) *gain scheduling*.

Linear Parameter Varying (LPV) systems can be considered as nonlinear systems which are linearized along a time varying trajectory. Modelling and identification of LPV systems

is described in various papers of the last years and a textbook, [26]. LPV models can be described by state space models in which the system matrices are fixed functions of a known time varying parameter vector $\boldsymbol{p}_v(t) \in \mathbb{R}^s$. In a continuous time framework the state space equations can be expressed as

$$\begin{aligned} \dot{\boldsymbol{x}}(t) &= \boldsymbol{A}(\boldsymbol{p}_v(t))\boldsymbol{x}(t) + \boldsymbol{B}(\boldsymbol{p}_v(t))\boldsymbol{u}(t) \\ \boldsymbol{y}(t) &= \boldsymbol{C}(\boldsymbol{p}_v(t))\boldsymbol{x}(t) + \boldsymbol{D}(\boldsymbol{p}_v(t))\boldsymbol{u}(t) \\ \boldsymbol{x}(0) &= \boldsymbol{x}_0 \qquad . \end{aligned} \tag{3.29}$$

The parameter vector $\boldsymbol{p}_v(t)$ determines the time varying parameter trajectory used for the linearization of the system.

To overcome various drawbacks of the *gain scheduling* approach (e.g. the often large number of linear models needed and the slow changes between operating points which are required for adequate performance) research concentrates on the design of a *global* controller for LPV systems. The term *global* refers to the fact that one controller should be able to control the LPV system for the whole set of operating points. This is only possible with a nonlinear controller because of the nonlinear system behaviour for different operating points.

The structure of the global controller $\boldsymbol{K}$ can be described by a state space model in the form of eq.(3.29) as well. The controller depends on the systems states $\boldsymbol{x}(t)$ on the one hand. On the other hand, knowledge about the actual parameters $\boldsymbol{p}_v(t)$ is required for the synthesis of such a controller such that $\boldsymbol{K} = \boldsymbol{K}(\boldsymbol{x}(t), \boldsymbol{p}_v(t))$. However, online measurement of the time varying parameters will not naturally be possible. Even if the time varying parameters can be measured, effects of measurement noise and the influence of parameter uncertainties on the controller will have to be taken into account.

System identification and controller design for LPV systems are a focus of actual research. This involves e.g. investigations to which extend analogies to linear identification techniques like subspace methods, which are described in section 3.3.4, are applicable for the identification of LPV systems.

3.2 Modelling by first principles

A model of a process or a dynamic system is a description of its I/O behaviour. This description can be *mental* (an experience based model e.g. the mental model to drive a car in daily life), *graphical* (e.g. tables or plots of characteristics) or *mathematical*. For high performance control applications mathematical models are used which describe the system dynamics most often by differential or difference equations, [14].

A first step for modelling a complex dynamic system is to divide the system into subsystems. The transfer behaviour of the system can then be described by joining the subsystems mathematically, [14]. Often the reason for this subdivision is that the dynamics of the subsystems can be described analytically by first principles. These could be differential

or difference equations based on physical laws. Usually simplifying assumptions about the system have to be made to derive models by first principles.

For the basic equations the following types can be distinguished, [7]:

1. **Conservation equations** for stored energies, masses and impulses.
2. **Component equations** (physical-chemical state equations).
3. **Phenomenological equations** for irreversible processes taking place (e.g. heat transfer, diffusion or chemical reaction).
4. **Entropy conservation equations** if various irreversible processes occur (if not included in 3).
5. **Connection equations** describe the connection of process elements.

Furthermore the dependencies of the system parameters must be clarified. Parameters can either be *distributed* (depending on time and position) or *concentrated* (not position dependent). While systems with distributed parameters must be modelled by partial differential equations, those with concentrated parameters are modelled by ordinary differential equations.

After the description of the single process elements the resulting equations are joined by mathematical connection laws thus often leading to complicated complete systems. Of course, the resulting models are not necessarily linear. Depending on the characteristic of the nonlinearity and the control objectives a linearization with respect to one or more operating points can be done. This is one possible step towards model simplification. Another could be for example the approximation of distributed parameters by concentrated parameters if the operating point is stationary in position, [7].

However, if the system dynamics are not well-understood, the model equations can not be derived easily or effects are neglected in the equations which are important for the system dynamics. Furthermore, physical state equations are usually subject to restrictions (e.g. operating points like power levels etc.). For the resulting model, assumptions have to be made which suppose the underlying equations hold for the physical conditions the system operates in. The alternative to modelling by first principles is system identification which is described in section 3.3.

3.3 System identification

Another way to obtain a model of a dynamic system is system identification. This is an experimental based way of modelling. The basic idea behind it is to excite a system with specifically designed input signals (how these signals are chosen will be explained in section

3.3.2), record input and output data of the plant (usually in open-loop) and estimate the parameters of a choosen model structure by analyzing the recorded data. For the data analysis e.g. MATLAB's *System identification toolbox* can be used.

The following explanations deal with linear system identification only, i.e. the obtained models are linear. Nonlinear systems thus can only be described appropriately by these models for a certain operating point and in a certain frequency range.

3.3.1 Structure of the identification process

The system identification process can be structured into four main steps, [14]:

1. **The data record:** The system to be identified must be excited by well chosen input signals (see the following section) such that the dynamical behaviour of the system is revealed. The experiments are usually done in open-loop because the uninfluenced system behaviour should be identified. The experiments result in sets of measured I/O data.

2. **Choice of set of models or the model structure:** Depending on the previous knowledge of the system to be identified, *gray box* or *black-box* models can be chosen. These terms will be explained in section 3.3.3. The choice of an appropriate model structure involves the dynamic order of the model as well. Techniques to choose the order approriately are presented in section 3.3.4.

3. **Estimation of the model parameters:** Upon all the models included in the chosen model structure one has to be found that reproduces the measured data best with respect to a chosen objective. This objective could be an output error functional that should be minimal for an obtained parameter set of the model. The model is parametrized by analyzing a set of measured data, which will be called *ID data*.

4. **Model validation:** An I/O model of a system must proof its quality of predicting output data of the system sufficiently accurate within the operation range the model has been developed for. Validation means that a data set not contained in the *ID data* set is used to test the performance of the model by comparing the measured output data with the model output for the same input data.

Usually, system identification is an iterative process because it is most likely that the first obtained model will not show good performance in validation. The reasons for this can be e.g. that the input data was not informative enough to reveal certain system behaviour or that numerical problems occurred during the parameter estimation, thus leading to a mismatched parametrization.

Table 3.1: PE orders for standard signals, [28]

Signal type	**Order of PE**
Dirac impulse $\delta(k)$	0
Step function $\sigma(k)$	1
Sine wave $\sin(k)$	2
White noise	∞

3.3.2 Choice of input signals

To choose appropriate input data for the system identification experiments is a very important step in the identification process and mainly responsible for the quality of the inferred model. The input data must excite all dynamic modes of the system that are of interest for the model. That means that the input data must be "rich" enough of excitation, [28].

To classify the excitation properties of a signal the property *persistency of excitation* (PE) can be used. The degree of the persistency of excitation is a measure for the information content of a signal.

Theorem 3.1 *A signal $u(k)$ is persistently exciting of order n if and only if*

$$\lim_{k\to\infty} \frac{1}{k} \left(\sum_{l=0}^{k} a(z)u(l) \right)^2 > 0 \qquad \forall a(z): \quad deg\, a(z) \leq n \tag{3.30}$$

In this theorem $a(z)$ is a polynomial in the *forward shift operator* z that has been defined in eq.(3.24). The structure of $a(z)$ is thus given by

$$a(z) = a_0 + a_1 z + a_2 z^2 + \ldots + a_{n-1} z^{n-1} \,. \tag{3.31}$$

In [14] the following theorem is derived:

Theorem 3.2 *Consider a set $\mathcal{M}$ of models such that their transfer functions $G(z,\theta)$ are rational functions:*

$$G(z,\theta) = \frac{B(z,\theta)}{F(z,\theta)} = \frac{z^{-n_k}\left(b_1 1 + b_2 z^{-1} + \ldots + b_{n_b} z^{-n_b+1}\right)}{1 + f_1 z^{-1} + \ldots + f_{n_f} z^{-n_f}} \,. \tag{3.32}$$

Then an open-loop experiment with an input that is persistently exciting of order $n_b + n_f$ is sufficiently informative with respect to $\mathcal{M}$.

With the help of eq. (3.30) the information content of a signal can be quantified. If a polynomial $a(z)$ of order n can be found that does not satisfy eq.(3.30) the signal has a lower oder of persistency of excitation than n. The PE orders of some standard signals are listed in table 3.1. Hence, a suitable test signal for identification experiments is bandlimited white noise (see chapter 5.2.1).

3.3.3 Model structures for system identification

The model structure specifies the type of model which is obtained by the identification process. With linear system identification linear time invariant model structures such as transfer functions or state space models are parametrized.

In section 3.3.1 the model structures *black box models* and *gray box models* have been mentioned. The terms refer to the structural constraints for the parametrization of the chosen LTI-model. For black box models, the parameters can be considered purely as vehicles for adjusting the fit while the parameters of gray box models incorporate an amount of physical insight into the system behaviour which implies constraints on the model structure, [14].

After the decision is made which model structure model shall be used, the model order must be specified. This can be done by analysis of the recorded data sets using the *singular value decomposition* (see section 3.3.4 and appendix A). Once a defined system order or a range of orders is specified, a *model set* exists whose parameters must be estimated in the identification process. The formal definition of a model structure can be found in [14]. A model structure can be considered as a parametrized set of models.

Structural constraints for parametrization

If gray box models are used, the parametrization of the model structure is constrained to resemble the amount of physical insight of the system behavior in the model. For example, a certain structure for the system matrix $\boldsymbol{A}$ of a state space model can be specified such that some matrix elements have the same value or are common multiples [2].

3.3.4 Estimation of the model parameters

After the experimental data is recorded it has to be analysed to obtain the parameters of the chosen model structure. A variety of parameter estimation methods exists and as literature sources [14], [8] and [9] are recommended. For the parametrization of LTI model structures, direct subspace methods are a well established tool and will be described in he following section. Direct subspace methods are implemented in the *MATLAB System Identification Toolbox*.

[2] In MATLAB commands like `idgrey` in combination with `modreal` can be used to apply constraints on a model set

Direct subspace methods

A powerful method to estimate the parameters of LTI state space models for multivariable systems are *direct subspace methods* [3]. Here only a brief idea of the method shall be outlined at the example of a multivariable (MIMO) system, [28].

The state space form of the model is given by

$$\begin{aligned} \boldsymbol{x}(k+1) &= \boldsymbol{A}\boldsymbol{x}(k) + \boldsymbol{B}\boldsymbol{u}(k) \\ \boldsymbol{y}(k) &= \boldsymbol{C}\boldsymbol{x}(k) + \boldsymbol{D}\boldsymbol{u}(k) \end{aligned} \tag{3.33}$$

and the dimensions of the signals are $\boldsymbol{y} \in \mathbb{R}^n$, $\boldsymbol{u} \in \mathbb{R}^m$ and $\boldsymbol{x} \in \mathbb{R}^l$. A very important point is that the order of the system l is not yet known and has to be determined in the identification process. The measured output data $\boldsymbol{y}$ can be represented for each time instant k as:

$$\begin{aligned} \boldsymbol{y}(k) &= \boldsymbol{C}\boldsymbol{x}(k) + \boldsymbol{D}\boldsymbol{u}(k) \\ \boldsymbol{y}(k+1) &= \boldsymbol{C}\boldsymbol{A}\boldsymbol{x}(k) + \boldsymbol{C}\boldsymbol{B}\boldsymbol{u}(k) + \boldsymbol{D}\boldsymbol{u}(k+1) \\ \boldsymbol{y}(k+2) &= \boldsymbol{C}\boldsymbol{A}^2\boldsymbol{x}(k) + \boldsymbol{C}\boldsymbol{A}\boldsymbol{B}\boldsymbol{u}(k) + \boldsymbol{C}\boldsymbol{B}\boldsymbol{u}(k+1) + \boldsymbol{D}\boldsymbol{u}(k+2) \\ &\vdots \end{aligned} \tag{3.34}$$

If α samples are considered for an output data set the following matrices are introduced

$$\boldsymbol{\mathcal{O}}_\alpha = \begin{pmatrix} \boldsymbol{C} \\ \boldsymbol{C}\boldsymbol{A} \\ \boldsymbol{C}\boldsymbol{A}^2 \\ \vdots \\ \boldsymbol{C}\boldsymbol{A}^{\boldsymbol{\alpha-1}} \end{pmatrix}, \; \boldsymbol{\Psi}_\alpha = \begin{pmatrix} \boldsymbol{D} & \boldsymbol{0} & \boldsymbol{0} & \dots & \boldsymbol{0} \\ \boldsymbol{C}\boldsymbol{B} & \boldsymbol{D} & \boldsymbol{0} & \dots & \boldsymbol{0} \\ \boldsymbol{C}\boldsymbol{A}\boldsymbol{B} & \boldsymbol{C}\boldsymbol{B} & \boldsymbol{D} & \dots & \boldsymbol{0} \\ \vdots & \vdots & \ddots & \ddots & \vdots \\ \boldsymbol{C}\boldsymbol{A}^{\alpha-2}\boldsymbol{B} & \boldsymbol{C}\boldsymbol{A}^{\alpha-1}\boldsymbol{B} & \dots & \boldsymbol{C}\boldsymbol{B} & \boldsymbol{D} \end{pmatrix},$$

$$\boldsymbol{X} = \begin{pmatrix} \boldsymbol{x}(1) & \boldsymbol{x}(2) & \dots & \boldsymbol{x}(N) \end{pmatrix}$$

and with the vectors

$$\boldsymbol{Y}_k = \begin{pmatrix} \boldsymbol{y}(k) \\ \boldsymbol{y}(k+1) \\ \vdots \\ \boldsymbol{y}(k+\alpha-1) \end{pmatrix}, \quad \boldsymbol{U}_k = \begin{pmatrix} \boldsymbol{u}(k) \\ \boldsymbol{u}(k+1) \\ \vdots \\ \boldsymbol{u}(k+\alpha-1) \end{pmatrix}$$

we can write the outputdata of the system as

$$\boldsymbol{Y}_k = \boldsymbol{\mathcal{O}}_\alpha \boldsymbol{x}(k) + \boldsymbol{\Psi}_\alpha \boldsymbol{U}_k \; . \tag{3.35}$$

[3] Developed in the 1990s by De Moor and Van Overschee, see [25] for details

The matrix $\boldsymbol{\mathcal{O}}_\alpha$ is the so-called *extended observability matrix*.

The dimensions of the matrices are $\boldsymbol{\mathcal{O}}_\alpha \in \mathbb{R}^{n\alpha \times l}$, $\boldsymbol{\Psi}_\alpha \in \mathbb{R}^{n\alpha \times m\alpha}$, $\boldsymbol{X} \in \mathbb{R}^{l \times N}$, $\boldsymbol{Y}_k \in \mathbb{R}^{n\alpha \times 1}$ and $\boldsymbol{U}_k \in \mathbb{R}^{m\alpha \times 1}$.

Assuming that a number of $N + \alpha - 1$ samples of I/O data for each channel has been recorded the following matrix can be formed

$$\begin{pmatrix} \boldsymbol{Y}_1 & \boldsymbol{Y}_2 & \dots & \boldsymbol{Y}_N \end{pmatrix} = \begin{pmatrix} \boldsymbol{y}(k) & \boldsymbol{y}(k+1) & \dots & \boldsymbol{y}(k+N) \\ \boldsymbol{y}(k+1) & \boldsymbol{y}(k+2) & \dots & \boldsymbol{y}(k+N+1) \\ \vdots & \vdots & \dots & \vdots \\ \boldsymbol{y}(k+\alpha-1) & \boldsymbol{y}(k+\alpha) & \dots & \boldsymbol{y}(k+N+\alpha-1) \end{pmatrix} . \quad (3.36)$$

The matrix denoted in eq.(3.36) consists only of measurement data and a matrix of this structure is called *Hankel matrix*. It is constructed analogously to the *moving horizon principle*[4]: Each column marks a data sequence of length α and the next column is obtained by stepping (in this case) one sample forward (moving horizont).

If we define

$$\boldsymbol{\mathcal{Y}} = \begin{pmatrix} \boldsymbol{Y}_1 & \boldsymbol{Y}_2 & \dots & \boldsymbol{Y}_N \end{pmatrix} \quad (3.37)$$

and form a Hankel matrix for the input data analogously

$$\boldsymbol{\mathcal{U}} = \begin{pmatrix} \boldsymbol{U}_1 & \boldsymbol{U}_2 & \dots & \boldsymbol{U}_N \end{pmatrix} \quad (3.38)$$

we can write eq. (3.35) as

$$\boldsymbol{\mathcal{Y}} = \boldsymbol{\mathcal{O}}_\alpha \boldsymbol{X} + \boldsymbol{\Psi}_\alpha \boldsymbol{\mathcal{U}} . \quad (3.39)$$

The matrices in eq.(3.39) have the dimensions $\boldsymbol{\mathcal{Y}} \in \mathbb{R}^{n\alpha \times N}$ and $\boldsymbol{\mathcal{U}} \in \mathbb{R}^{m\alpha \times N}$. To identify the parameters of the state space model the matrices $\boldsymbol{\mathcal{O}}_\alpha$ (giving $\boldsymbol{C}$ and $\boldsymbol{A}$) and $\boldsymbol{\Psi}_\alpha$ (from which $\boldsymbol{D}$ and $\boldsymbol{B}$ can be extracted) must be obtained. The value of α should be chosen greater than the expected model order.

For the parameter estimation procedure a projection is used that maps the output data on the *nullspace* of the input matrix $\boldsymbol{\mathcal{U}}$ to eliminate the term $\boldsymbol{\Psi}_\alpha \boldsymbol{\mathcal{U}}$ in eq.(3.39) such that the term $\boldsymbol{\mathcal{O}}_\alpha \boldsymbol{X}$ can be estimated.

Definition 3.1 *The space of all vectors $\boldsymbol{q}$ that result in a null vector when multiplied from the left by $\boldsymbol{\mathcal{U}}$ is defined as the nullspace $\boldsymbol{\mathcal{N}}(\boldsymbol{\mathcal{U}})$:*

$$\boldsymbol{\mathcal{N}}(\boldsymbol{\mathcal{U}}) = \{\boldsymbol{q} : \quad \boldsymbol{\mathcal{U}}\boldsymbol{q} = \boldsymbol{0}\} . \quad (3.40)$$

The matrix

$$\boldsymbol{\Pi} = \boldsymbol{I} - \boldsymbol{\mathcal{U}}^T \left(\boldsymbol{\mathcal{U}}\boldsymbol{\mathcal{U}}^T\right)^{-1} \boldsymbol{\mathcal{U}} , \quad \boldsymbol{\Pi} \in \mathbb{R}^{N \times N} \quad (3.41)$$

[4]The term *moving horizon* has its origin in predictive control, where future control signals are predicted for a specified time interval (horizon) ahead on basis of past I/O data, [3]

is used to project $\boldsymbol{\mathcal{Y}}$ on $\boldsymbol{\mathcal{N}}(\boldsymbol{\mathcal{U}})$, [28]. The condition that $\boldsymbol{\mathcal{U}}\boldsymbol{\mathcal{U}}^T$ is invertible is fullfilled because the input data is assumed to be persistenly exciting of order $m\alpha$. Because of this projection the name *subspace methods* has been given to the identification routine. The projection yields

$$\boldsymbol{\mathcal{Y}}\boldsymbol{\Pi} = (\boldsymbol{\mathcal{O}}_\alpha \boldsymbol{X} + \boldsymbol{\Psi}_\alpha \boldsymbol{\mathcal{U}})\,\boldsymbol{\Pi} = \boldsymbol{\mathcal{O}}_\alpha \boldsymbol{X}\boldsymbol{\Pi}\,. \tag{3.42}$$

The matrix $\boldsymbol{\mathcal{O}}_\alpha$ has l columns, therefore the known matrix $\boldsymbol{\mathcal{Y}}\boldsymbol{\Pi}$ can be factorized into a left matrix with n columns and a right matrix with n rows. This is done with the *singular value decomposition* (see appendix A for a detailed deduction) and yields

$$\boldsymbol{\mathcal{Y}}\boldsymbol{\Pi} = \boldsymbol{Q}_s \boldsymbol{\Sigma}_s \boldsymbol{V}_s^T + \boldsymbol{Q}_n \boldsymbol{\Sigma}_n \boldsymbol{V}_n^T \approx \boldsymbol{Q}_s \boldsymbol{\Sigma}_s^{1/2} \boldsymbol{\Sigma}_s^{1/2} \boldsymbol{V}_s^T\,. \tag{3.43}$$

With the matrices $\boldsymbol{Q}_s \in \mathbb{R}^{n\alpha \times \hat{r}}$ and $\boldsymbol{V}_s^T \in \mathbb{R}^{N \times \hat{r}}$ the matrix $\boldsymbol{\mathcal{Y}}\boldsymbol{\Pi}$ is factored in a left factor with l columns and full rank and a right factor with l rows. This leads to the the following result for the model order and the estimation of $\boldsymbol{A}$ and $\boldsymbol{C}$:

Model order and estimation of $\boldsymbol{\mathcal{O}_\alpha}$
The *numerical rank* (see appendix A) of $\boldsymbol{\mathcal{Y}}\boldsymbol{\Pi}$, that equals the model order l, can be estimated by the investigation of the singular values, i.e. the diagonal elements of $\boldsymbol{\Sigma}$. Furthermore, using the singular value decomposition of $\boldsymbol{\mathcal{Y}}\boldsymbol{\Pi}$ the extended observability matrix $\boldsymbol{\mathcal{O}}_\alpha$ can be estimated. Thus, the state space model's matrices $\boldsymbol{C}$ and $\boldsymbol{A}$ are obtained:

$$\boldsymbol{\mathcal{O}}_\alpha = \boldsymbol{Q}_s \boldsymbol{\Sigma}_s^{1/2} \qquad \Longrightarrow \quad \boldsymbol{C},\ \boldsymbol{A} \tag{3.44}$$

In appendix A it is noted that the factorization matrices $\boldsymbol{Q}$ and $\boldsymbol{V}$ are orthogonal which gives

$$\boldsymbol{Q}\boldsymbol{Q}^T = \begin{pmatrix} \boldsymbol{Q}_s^T \\ \boldsymbol{Q}_n^T \end{pmatrix} \begin{pmatrix} \boldsymbol{Q}_s & \boldsymbol{Q}_n \end{pmatrix} = \begin{pmatrix} \boldsymbol{I} & \boldsymbol{0} \\ \boldsymbol{0} & \boldsymbol{I} \end{pmatrix}\,. \tag{3.45}$$

Because $\boldsymbol{Q}_n^T \boldsymbol{Q}_s = \boldsymbol{0}$ the approximation $\boldsymbol{Q}_n^T \boldsymbol{\mathcal{O}}_\alpha \approx \boldsymbol{0}$ can be done. Multiplying eq.(3.39) by $\boldsymbol{Q}_n^T$ from the left and by $\boldsymbol{\mathcal{U}}^T \left(\boldsymbol{\mathcal{U}}\boldsymbol{\mathcal{U}}^T\right)^{-1}$ from the right yields

$$\boldsymbol{Q}_n^T \boldsymbol{\mathcal{Y}} \boldsymbol{\mathcal{U}}^T \left(\boldsymbol{\mathcal{U}}\boldsymbol{\mathcal{U}}^T\right)^{-1} = \boldsymbol{Q}_n^T \boldsymbol{\Psi}_\alpha\,. \tag{3.46}$$

In eq.(3.46) $\boldsymbol{\Psi}_\alpha$ is the only unknown term and can be calculated by solving a linear system of equations. This gives the missing state space model matrices $\boldsymbol{B}$ and $\boldsymbol{D}$ such that all model parameters are identified. The algorithm can be summarized as follows:

Direct subspace projection algorithm:

- Form the matrices $\boldsymbol{Y}_k$, $\boldsymbol{U}_k$ and the according Hankel matrices $\boldsymbol{\mathcal{Y}}$ and $\boldsymbol{\mathcal{U}}$.
- Calculate the projection matrix $\boldsymbol{\Pi}$ (eq.(3.41)) and perform the projection $\boldsymbol{\mathcal{Y}\Pi}$.
- Calculate the model order by inspecting the singular values of $\boldsymbol{\mathcal{Y}\Pi}$ (eq.3.43) and calculate $\mathcal{O}_\alpha$.
- The first n rows and l columns form $\boldsymbol{C}$ and $\boldsymbol{A}$ can be calculated from $\mathcal{O}_\alpha$ and $\boldsymbol{C}$ solving a linear set of equations resulting from the structure of $\mathcal{O}_\alpha$.
- Calculate $\boldsymbol{\Psi}_\alpha$ using eq.(3.46).
- Extract $\boldsymbol{D}$ and $\boldsymbol{B}$ solving a linear set of equations resulting from the structure of $\boldsymbol{\Psi}_\alpha$.

MATLAB provides with the command `n4sid` a tool to use subspace methods for parameter estimation.

Chapter 4

Physical RF model of ACC1

To model the dynamics of superconducting cavities by first principles, the resonator dynamics can be divided into an electrical part and a mechanical part. In this chapter first, a model of the RF-field behaviour in superconducting cavities is derived using analogies to an electrical resonant circuit. The resultant resonant circuit model is an LPV state space model and its properties are investigated. Moreover, modelling of mechanical vibration modes of the cavities is discussed. The derivation of the resonant circuit model and the modelling of the mechanical dynamics of the cavities is described in the section 4.1 on the basis of [20].

The resonant circuit model is tested in an output error (OE) model structure (see figure 4.7). It has to be clarified whether it is an appropriate model for the large signal cavity behaviour for the aspect of controller design. The model output is compared with open-loop measurement data of TTF2. The parameters of the model like the cavity bandwidth $\omega_{1/2}$ are estimated by two different optimization routines to optimize the model output error in a least squares sense (see 4.3.2). The evaluation of the results, which is presented in section 4.3.3, suggests that a different approach to the modelling of the linear accelerator module ACC1 seems reasonable, the system identification (see section 3.3).

4.1 Electrical resonant circuit model

In [20] it is proposed that the electrical behaviour of a superconducting cavity can be physically modelled using analogies to an electrical resonant circuit consisting of an inductance, a capacitor and a resistor (see Figure 4.1).

The quality of a resonant device can be described by the quality factor Q which is defined as

$$Q = 2\pi \frac{\text{stored energy in resonator}}{\text{dissipated energy per cycle}} = \frac{\omega_0 W}{P_{diss}} \tag{4.1}$$

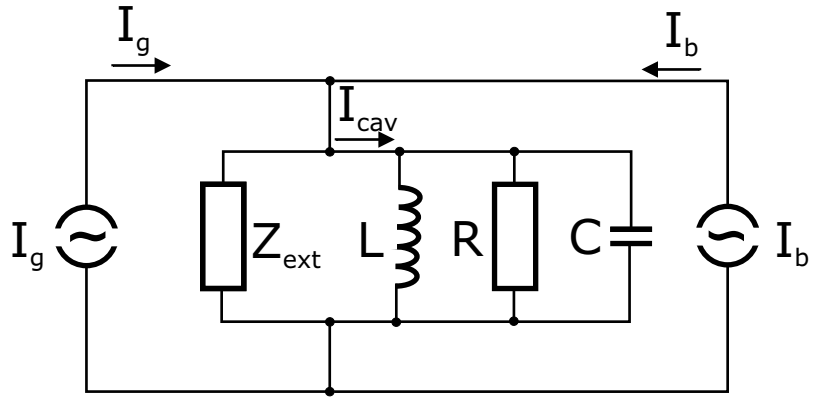

Figure 4.1: Electrical resonant circuit

where W denotes the energy stored in the resonator, ω_0 is the resonance frequency and P_{diss} is the dissipated power, [30]. The unloaded quality factor Q_0 of a superconducting cavity can be obtained if only the (still present) RF resistance R of the cavity walls is considered responsible for the losses. Thus the dissipated power can be expressed as $P_{diss} = V_0^2/(2R)$ and the stored energy as $W = 1/2\, CV_0^2$ where V_0 is the amplitude of the oscillating voltage and C the capacity of the resonator. Inserting these terms in eq.(4.1) and using the equation for the resonance frequency of an LC-circuit $\omega_0 = \sqrt{1/LC}$ yields

$$Q_0 = \frac{2\pi}{T} \cdot \frac{\frac{1}{2} CV_0^2}{\frac{1}{2}\frac{V_0^2}{R}} = \omega_0 RC = \frac{R}{L\omega_0} \tag{4.2}$$

where $T = \frac{2\pi}{\omega_0}$ in this context denotes the oscillation period of the LC-circuit in resonance. Considering further energy dissipation by the power coupler and the transmission lines (the external load) the external quality factor Q_{ext} is defined as

$$Q_{ext} = 2\pi \frac{\text{stored energy in cavity}}{\text{dissipated energy in external devices per cycle}} = \frac{\omega_0 W}{P_{ext}} \tag{4.3}$$

where P_{ext} is the dissipated power in all external devices. The so-called loaded quality factor of a resonantor system is obtained by considering all losses, i.e.

$$Q_L = 2\pi \frac{\text{stored energy in cavity}}{\text{total energy loss per cycle}} = \frac{\omega_0 W}{P_{tot}} \tag{4.4}$$

with the conservation condition such that the total power loss equals the sum of the power loss caused by the external load and the dissipated power in the resonator itsself

$$P_{tot} = P_{diss} + P_{ext}\,. \tag{4.5}$$

The combination of equations (4.2), (4.3) and (4.4) results in

$$\frac{1}{Q_L} = \frac{1}{Q_0} + \frac{1}{Q_{ext}}\,. \tag{4.6}$$

The unloaded quality factor of superconducting cavities is typically several orders of magnitude larger than the external quality factor ($Q_0 \gg Q_{ext}$) and therefore $Q_L \approx Q_{ext}$ holds.

In chapter 2.2.2 the couplers have been be described as electrical transformers. If the external loads are taken into account for calculations on the cavity side of the coupler, these loads must be scaled according to the electrical transformation laws. When this is done, the external power losses can be modelled as caused by a parallel resistor Z_{ext} in the cavity's resonant circuit (for a detailed explanation of the transformation procedure see [20]). The combination of the parallel resistors yields the shunt impedance

$$\frac{1}{R_L} = \frac{1}{R} + \frac{1}{Z_{ext}}\,, \tag{4.7}$$

where Z_{ext} is a real quantity (the characteristic impedance of a coaxial cable is 50Ω).

An approach to model a superconducting cavity is to describe the cavity as an externally driven LCR resonant circuit. In Figure 4.1, I_g denotes the generator current driving the cavity and I_b is the current caused by the moving electrons of the pulsed beam. Considering an harmonic generator current $I_g = \hat{I}_{g,0} \cdot \sin(\omega t)$, for the superposition of I_g and I_b only the Fourier component of the pulsed electron beam at the frequency ω has to be taken into account, [20]. The resulting total driving current is denoted $I(t)$.

Using Kirchhoff's rule, the driving current results in

$$I_{cav} = I = I_C + I_L + I_R\,. \tag{4.8}$$

Differentiating eq.(4.8), inserting the parameters R, C, L and introducing the voltage V of the parallel circuit gives

$$\ddot{V}(t) + \frac{1}{R_L C}\dot{V}(t) + \frac{1}{LC}V(t) = \frac{1}{C}\dot{I} \quad . \tag{4.9}$$

The inductance L and the capacitance C can be replaced by the quantities Q_L and ω_0 ($\frac{1}{R_L C} = \frac{\omega_0}{Q_L}$ and $\frac{1}{LC} = \omega_0^2$) to get

$$\ddot{V}(t) + \frac{\omega_0}{Q_L}\dot{V}(t) + \omega_0^2 V(t) = \frac{\omega_0 R_L}{Q_L}\dot{I} \quad . \tag{4.10}$$

With the assumption of a harmonic generator current $I_g(t)$ the current $I(t) = \hat{I}_0 \sin(\omega t)$ is harmonic as well and thus the driving term of eq.(4.10) is $\dot{I}(t) = \hat{I}_0 \omega \cos(\omega t)$. The particular solution of the differential eq.(4.10) describes the stationary behaviour of the resonant circuit and is given by the harmonic oscillating voltage

$$V(t) = \hat{V} \cdot \sin(\omega t + \psi) \tag{4.11}$$

with the phase relation

$$\tan(\psi) = R_L \cdot \left(\frac{1}{\omega L} - \omega C\right) \tag{4.12}$$

and the amplitude

$$\hat{V} = \frac{R_L \hat{I}_0}{\sqrt{1 + \left[R_L\left(\frac{1}{\omega L} - \omega C\right)\right]^2}} \quad . \tag{4.13}$$

The phase angle ψ between the driving current I and the voltage V is defined as the tuning angle of the cavity [20]. To point up the relation between the drive frequency ω and the cavity's resonance frequency ω_0 again the parameters L and C are replaced with Q_L and ω_0 yielding

$$\tan(\psi) = \frac{\omega_0}{\omega} \cdot \underbrace{\frac{R_L}{\omega_0 L}}_{Q_L} - \frac{\omega}{\omega_0} \cdot \underbrace{\omega_0 R_L C}_{Q_L} = Q_L\left(\frac{\omega_0}{\omega} - \frac{\omega}{\omega_0}\right) \qquad \text{and} \tag{4.14}$$

$$\hat{V} = \frac{R_L \hat{I}_0}{\sqrt{1 + Q_L^2\left(\frac{\omega_0}{\omega} - \frac{\omega}{\omega_0}\right)^2}} = \frac{R_L \hat{I}_0}{\sqrt{1 + \tan^2(\psi)}} \quad . \tag{4.15}$$

The following approximations can be done if the drive frequency is close to the cavity's resonance frequency such that $\Delta\omega = \omega_0 - \omega$ is small:

$$\tan(\psi) \approx 2Q_L \frac{\Delta\omega}{\omega} \tag{4.16}$$

$$\hat{V}(\Delta\omega) \approx \frac{R_L \hat{I}_0}{\sqrt{1 + \left(2Q_L \frac{\Delta\omega}{\omega}\right)^2}} \tag{4.17}$$

The bandwidth where the voltage decreases by a factor of -3dB ($1/\sqrt{2}$) from its maximum $\hat{V}_0 = R_L \hat{I}_0$ is denoted as $\omega_{1/2}$ (the so-called *half-bandwidth* of a superconducting cavity because the energy stored in the cavity drops by half). From eq.(4.15) and (4.17) results

$$|\tan(\psi)| = 1 \qquad \Longleftrightarrow \psi = \pm\frac{\pi}{4} \tag{4.18}$$

$$\omega_{1/2} = \frac{\omega}{2Q_L} \quad . \tag{4.19}$$

With eq.(4.19) a more demonstrative definition of the loaded quality factor Q_L is given because with $Q_L = \frac{\omega}{2\omega_{1/2}}$ the "sharpness" of the resonance peak in the cavity's frequency response is described (see Figure 4.2), [30].

System theoretical analysis of the resonant circuit equation

Further analysis of eq.(4.10) can be done using system theoretical relations for second order differential equations,[27]. A dynamical system of second order with input $u(t)$ and output $y(t)$ (see Figure 3.1) can be described by means of the differential equation

$$\ddot{y}(t) + a_1 \dot{y}(t) + a_0 y(t) = b_0 u(t) \tag{4.20}$$

Substituting the more meaningful parameters natural frequency ω_n, static gain K_{stat} and damping ratio ζ for the coefficients in eq.(4.20) yields

$$\ddot{y}(t) + 2\zeta\omega_n\dot{y}(t) + \omega_n y(t) = K_{stat}\omega_n^2 u(t)\,. \tag{4.21}$$

Inserting the time derivative of the driving term $\dot{I}(t) = \hat{I}_0\omega\cos(\omega t)$ in eq.(4.10) yields

$$\ddot{V}(t) + \frac{\omega_0}{Q_L}\dot{V}(t) + \omega_0^2 V(t) = \frac{\omega_0 R_L \hat{I}_0\omega}{Q_L}\cos(\omega t)\,. \tag{4.22}$$

A comparison of the coefficients of eq.(4.21) and (4.22) yields

$$\omega_n = \omega_0\,, \quad \zeta = \frac{2}{Q_L} \ll \omega_0\,, \quad K_{stat} = \frac{R_L\hat{I}_0\omega}{Q_L\omega_0} \quad .$$

With standard values[1] $Q_L = 3\cdot 10^6$, $\omega_0 = 2\pi\cdot 1.3\cdot 10^9$ Hz and $R_L = 1/2\cdot R_{sh} \approx 521\Omega$ the bode diagram of the resonant circuit equation (4.22) can be constructed (see Figure 4.2). Important to notice is the fact that only the nine-cell resonator's π-mode (see 2.2.2 for details) is considered in eq. (4.22) and its bode diagram.

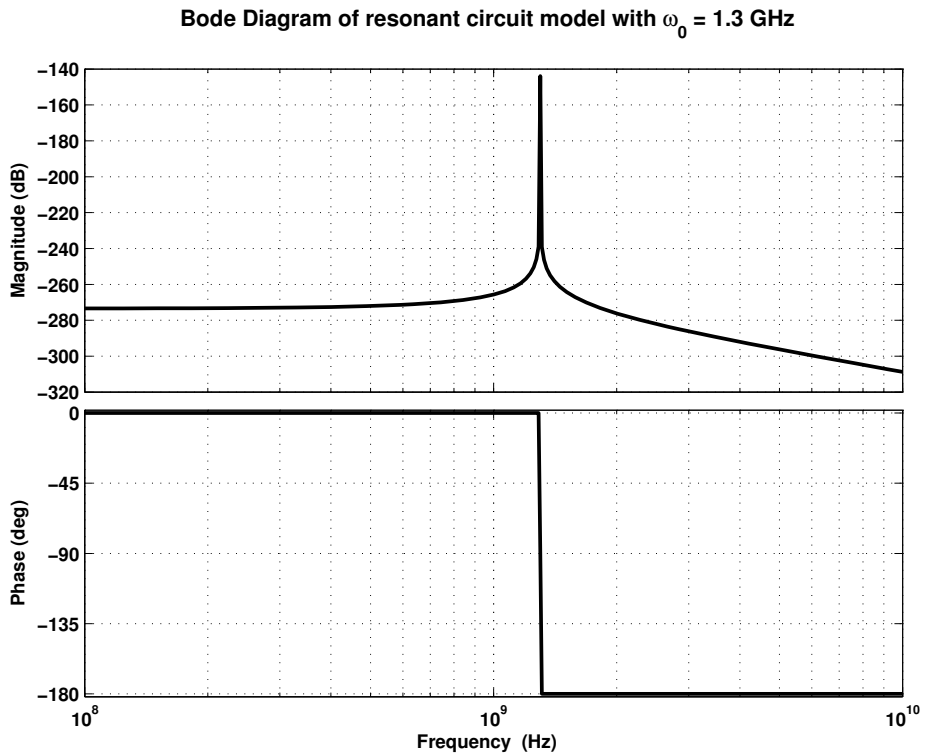

Figure 4.2: Bode diagram of cavity resonator (only π-mode is considered)

In Figure (4.2) it can be seen that the system is weakly damped because $\zeta = \frac{2}{Q_L} \ll \omega_0$ holds and the high Q_L determines the height of the resonance peak at $\omega_0 = 1.3$GHz.

[1]These values for the superconducting cavities of TTF2 were taken from [20]. A description of the so-called shunt resistor $R_{sh} = 1041\Omega$ is omitted because it is not further used in this thesis.

Derivation of the state-space model

To simplify computations with the harmonic voltages and currents they are described by complex numbers denoted in bold letters. The differential equation (4.22) of the driven resonant circuit becomes

$$\ddot{\mathbf{V}}(t) + \frac{\omega_0}{Q_L}\dot{\mathbf{V}}(t) + \omega_0^2\mathbf{V}(t) = \frac{\omega_0 R_L}{Q_L}\dot{\mathbf{I}}\,. \tag{4.23}$$

In [20] it has been shown that the resonant frequency ω_{res} of the superconducting cavities does not exactly correspond with the natural frequency ω_0 because ω_{res} depends on the loaded Q_L in the following way

$$\omega_{res} = \omega_0\sqrt{1 - \frac{1}{4Q_L^2}}\,. \tag{4.24}$$

However, because of the high loaded Q_L the resonance frequency of the TTF2 system can be approximated by its natural frequency such that $f_{res} \approx \frac{\omega_0}{2\pi} = 1.3\text{GHz}$.

For the operation of the free electron laser at DESY with a high beam quality, the main focus of interest lies on the slowly changing amplitudes and phases rather than the high frequent RF-field oscillation. Therefore, one separates the harmonic oscillation of the RF-generator and the appropriate Fourier component of the pulsed beam with a time dependence of $e^{i\omega t}$ from the low frequent changes of the real and imaginary part of the field vectors obtaining

$$\mathbf{V}(t) = (V_r(t) + iV_i(t)) \cdot e^{i\omega t}\,, \tag{4.25}$$
$$\mathbf{I}(t) = (I_r(t) + iI_i(t)) \cdot e^{i\omega t}\,. \tag{4.26}$$

In Figure 4.3 the previous considerations are illustrated: If one considers the turning voltage vector $\boldsymbol{V}(t)$ with the frequency ω_0 to be the frame of reference, only the changes in the *field envelope* e.g. the magnitude and phase changes of $\boldsymbol{V}(t)$ with respect to this frame of reference are of interest for the field quality.

By inserting this into eq.(4.23) and neglecting the second order derivatives a first order cavity differential equation for the field envelope can be deduced (for a detailed derivation see [20]):

$$\dot{V}_r(t) + \omega_{1/2}Vr + \Delta\omega V_i = R_L\omega_{1/2}I_r\,, \tag{4.27}$$
$$\dot{V}_i(t) + \omega_{1/2}Vi - \Delta\omega V_r = R_L\omega_{1/2}I_i\,. \tag{4.28}$$

The bandwidth of the cavity is denoted by $\omega_{1/2}$. The cavity detuning is a function of time during an RF-pulse such that $\Delta\omega = \Delta\omega(t)$ holds. The state space model to be derived depends linearly on the time varying parameter $\Delta\omega$ and is therefore an LPV model. The reasons for the timevarying detuning are disturbances like microphonics and the gradient dependent Lorentz force detuning that change the resonance frequency during the RF-pulse. The real (I_r) and imaginary part (I_i) of the resulting current from the RF-generator and the electron beam are the inputs of the state space model. The resultant field is decribed by the real and imaginary part (V_r and V_i) of the field's voltage vector. The LPV state space model is derived on the basis of eq.(4.27) and eq.(4.28) as follows:

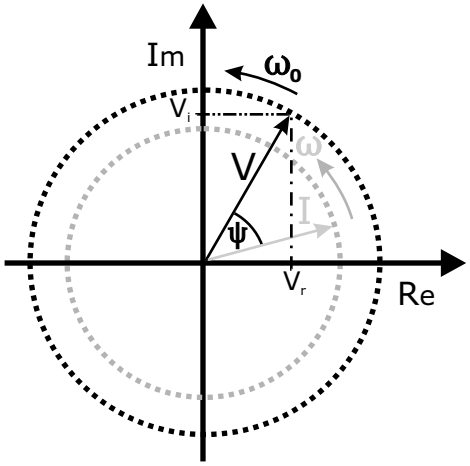

Figure 4.3: Complex driving voltage $\boldsymbol{I}(t)$ and cavity field vector $\boldsymbol{V}(t)$

LPV state space model of electrical cavity dynamics:

$$\begin{pmatrix} \dot{V}_r \\ \dot{V}_i \end{pmatrix} = \begin{pmatrix} -\omega_{1/2} & -\Delta\omega(t) \\ \Delta\omega(t) & -\omega_{1/2} \end{pmatrix} \begin{pmatrix} V_r \\ V_i \end{pmatrix} + R\,\omega_{1/2} \begin{pmatrix} 1 & 0 \\ 0 & 1 \end{pmatrix} \begin{pmatrix} I_r \\ I_i \end{pmatrix}. \tag{4.29}$$

The parameters of the state space model are the bandwidth $\omega_{1/2} \approx 2\pi \cdot 216.7\text{Hz}$ (for the TTF2 superconducting cavities) and the detuning $\Delta\omega$:

$$\omega_{1/2} = \frac{\omega_0}{2Q_L} \quad , \quad \Delta\omega(t) = \omega_0 - \omega(t) \tag{4.30}$$

Analysis of the state space model for the field envelope

In this subsection the state space model of the cavities presented in eq.(4.29) is analyzed with respect to the eigenvalues of the model,the frequency response and the controllability as well as observability of the model. These properties are investigated for both detuned and undetuned cavities but a fixed detuning ($\Delta\omega(t) = \Delta\omega$) is assumed. The assumption is reasonable for low gradients and for the flat top phase in particular where the gradient changes are moderate.

The eigenvalues of the system matrix

$$\boldsymbol{A} = \begin{pmatrix} -\omega_{1/2} & -\Delta\omega \\ \Delta\omega & -\omega_{1/2} \end{pmatrix}, \tag{4.31}$$

are calculated as follows

$$\lambda_{1,2} = \det(\lambda_{1,2}\boldsymbol{I} - \boldsymbol{A}) \tag{4.32}$$

$$= -\omega_{1/2} \pm i\Delta\omega\,. \tag{4.33}$$

In the undetuned case $\Delta\omega = 0\,\text{rad/sec}$ both eigenvalues are real and have the values $\lambda_1 = \lambda_2 = -\omega_{1/2}$. The cavity acts like a lowpass filter with a bandwidth of $\omega_{1/2}$. The I/O

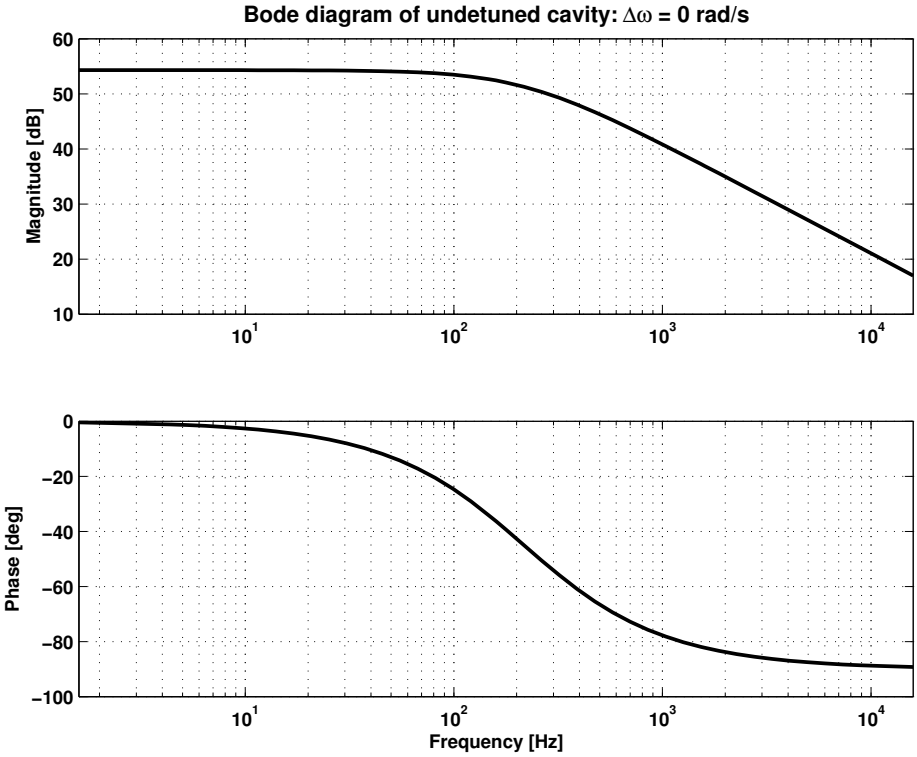

Figure 4.4: Bode diagram of undetuned cavity: $\Delta\omega = 0$ Hz

channels are decoupled and because of the symmetry in the structure of the model matrices the frequency responses from channel $u_1 = I_r$ to $y_1 = V_r$ and from $u_2 = I_i$ to $y_2 = V_i$ look the same. The bode diagram of an undetuned cavity is shown in Figure 4.4.

If the cavity is detuned, both input channels are coupled with both output channels. The eigenvalues become complex conjugated ($\lambda_{1,2} = -\omega_{1/2} \pm i\Delta\omega$). In Figure 4.5 the bode diagram for a detuned cavity with $\Delta\omega = \omega_{1/2}$ is shown. Because of the complex conjugated eigenvalues, resonance peaks can be seen in the transfer function from u_1 to y_1 and u_2 to y_2 respectively.

The following definitions for *controllability* and *observability* of a dynamical system can be found in [16].

Definition 4.1 *A system ($\boldsymbol{A}$,$\boldsymbol{B}$) is controllable if it can be transferred in a finite time interval T_f from an arbitrary initial state $\boldsymbol{x}_0$ to an arbitrary final state $\boldsymbol{x}(T_f)$ by an appropriately chosen input signal vector $\boldsymbol{u}_{[0,T_f]}$.*

It can be checked whether a system is controllable the help of the following definition:

Definition 4.2 *A system ($\boldsymbol{A}$,$\boldsymbol{B}$) is called controllable if its controllability matrix*

$$\mathcal{C} = \left[\begin{array}{cccc} \boldsymbol{A} & \boldsymbol{AB} & \boldsymbol{A}^2\boldsymbol{B} & \ldots \quad \boldsymbol{A}^{n-1}\boldsymbol{B} \end{array} \right] \tag{4.34}$$

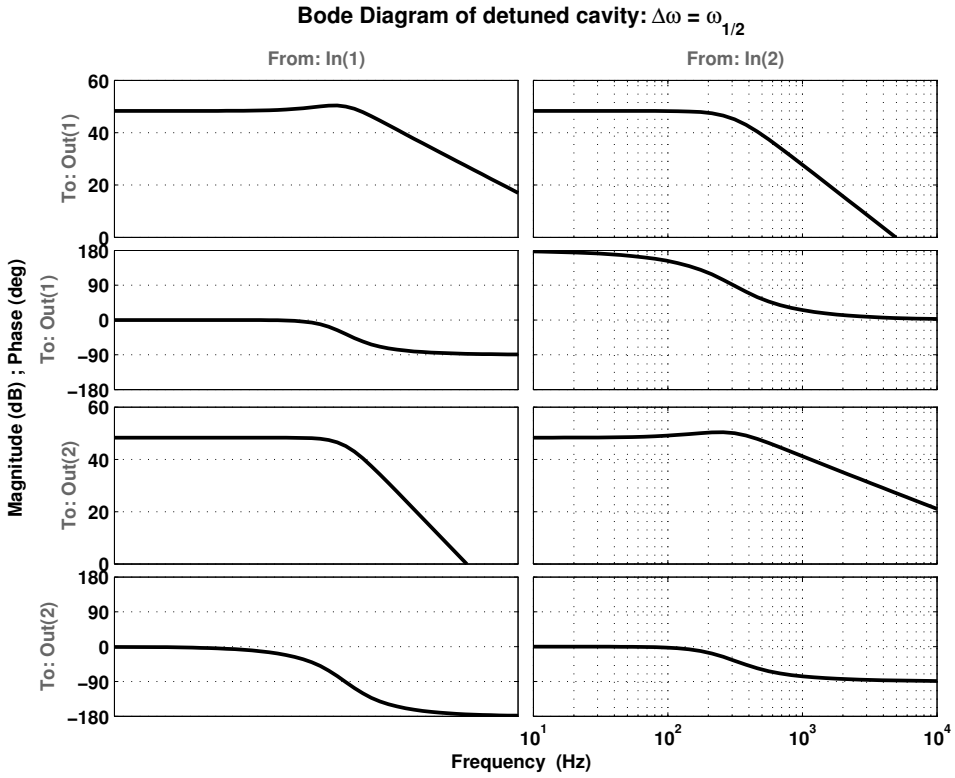

Figure 4.5: Bode diagram of detuned cavity: $\Delta\omega = \omega_{1/2}$ Hz

has full row rank.

The property *observability* of a dynamical system is defined as follows:

Definition 4.3 *A system* $(\boldsymbol{A},\boldsymbol{C})$ *is observable if the initial state* $\boldsymbol{x}_0$ *can be reconstructed from the trajectory of the input signals* $\boldsymbol{u}_{[0,T_f]}$ *and the trajectory of the output signals* $\boldsymbol{y}_{[0,T_f]}$*, both known for a finite time interval* $[0, T_f]$*.*

With the help of the following definition it can be checked whether a dynamical system is observable:

Definition 4.4 *A system* $(\boldsymbol{A}, \boldsymbol{C})$ *is called observable if its observability matrix*

$$\mathcal{O} = \begin{bmatrix} \boldsymbol{A} \\ \boldsymbol{C}\boldsymbol{A} \\ \boldsymbol{C}\boldsymbol{A}^2 \\ \cdots \\ \boldsymbol{C}\boldsymbol{A}^{n-1} \end{bmatrix} \tag{4.35}$$

has full column rank.

The output matrix $\boldsymbol{C}$ in eq. (4.29) is the unity matrix:

$$\boldsymbol{C} = \begin{pmatrix} 1 & 0 \\ 0 & 1 \end{pmatrix}.$$

The controllability and observability of the cavity state space model have been checked with the help of this definitions yielding that the model is controllable and observable for all detunings. The reason are the diagonal structures of $\boldsymbol{B}$ and $\boldsymbol{C}$ and the structure of the system matrix $\boldsymbol{A}$, which has full rank regardless of the value of $\Delta\omega$ such that the observability matrix and the controllability matrix have rank two.

4.2 Mechanical modes of cavities and detuning modelling

The mechanical stiffness of the superconducting cavity structures is low because of the thin walls. Vibrations and Lorentz forces cause changes in the geometrical shape of the cavity. Due to these shape changes the electrical resonance frequency of the cavity changes as well (see Section 2.2.5). Detailed investigations of mechanical properties of superconducting cavities by means of finite element analysis are presented in [5].

The static detuning of a cavity by Lorentz forces is proportional to the square of the accelerating field gradients $E_{acc}^2 = \mathbf{V}^T\mathbf{V}$. Because in the linear accelerator of TTF2 the cavities are operated in pulsed mode, the mechanical resonance modes of the cavity structures must be taken into account. These dynamics can be described by the following system of differential equations, [11]:

$$\begin{pmatrix} \Delta\dot{\omega}_1 \\ \Delta\ddot{\omega}_1 \\ \vdots \\ \Delta\dot{\omega}_N \\ \Delta\ddot{\omega}_N \end{pmatrix} = \begin{pmatrix} 0 & 1 & \cdots & 0 & 0 \\ -\omega_1^2 & -\frac{1}{\tau_1} & \cdots & 0 & 0 \\ \vdots & \vdots & \vdots & \ddots & \vdots \\ 0 & 0 & \cdots & 0 & 1 \\ 0 & 0 & \cdots & -\omega_N^2 & -\frac{1}{\tau_N} \end{pmatrix} \cdot \begin{pmatrix} \Delta\omega_1 \\ \Delta\dot{\omega}_1 \\ \vdots \\ \Delta\omega_N \\ \Delta\dot{\omega}_N \end{pmatrix} + 2\pi \begin{pmatrix} 0 \\ -K_1\omega_1^2 \\ \vdots \\ 0 \\ -K_N\omega_N^2 \end{pmatrix} \cdot \mathbf{V}^T\mathbf{V} \quad (4.36)$$

The parameters of eq.(4.36) are the detuning ω_m of mode m, the mechanical time constant τ_m of mode m and the Lorentz force detuning constant K_m of mode m. The total cavity-detuning resulting from the modes considered is given by $\Delta\omega = \sum \Delta\omega_m$.

This Lorentz force detuning depends on the time varying gradient thus leading to a time varying model for the cavities electrical dynamics: In equation 4.29 the system matrix has the time variant element $\Delta\omega = \Delta\omega(t)$ and the state space model is an LPV model because the system matrix $\boldsymbol{A}$ linearly depend on $\Delta\omega(t)$.

Equation (4.36) is an approach to describe the complex detuning process but this model up to now could not be validated. The detuning of the cavity can not be measured directly.

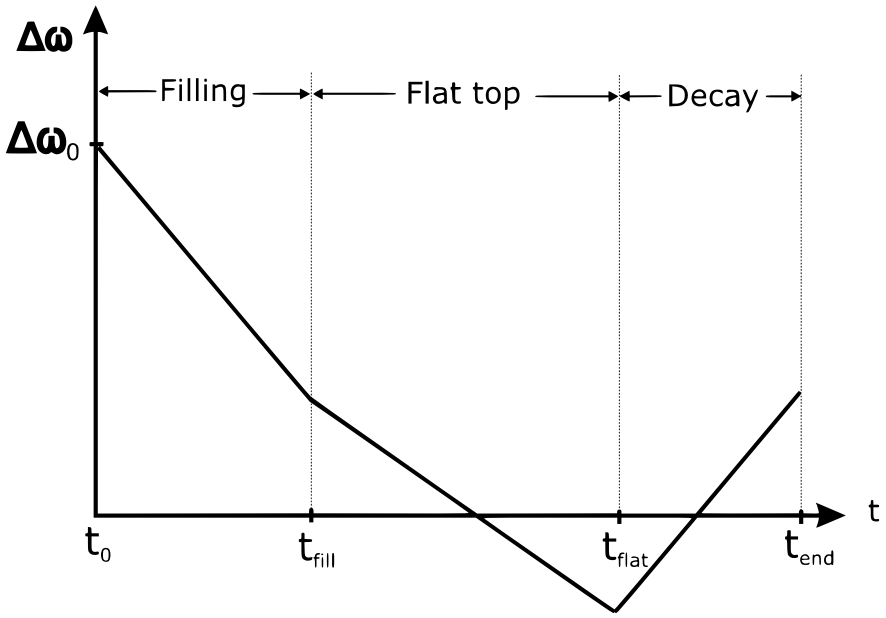

Figure 4.6: Approximation for detuning trajectory of one pulse

Therefore a detuning curve has to be estimated on the basis of the measured input and output signals. A reasonable choice for the qualitative shape of this curve seems to be three continuous lines (one for each time interval filling, flat-top and decay) as shown in Figure (4.6). Such a detuning curve $\Delta\omega(t)$ can be described by four parameters: An initial value $\Delta\omega_0$ (the predetuning) and a slope $d_{\Delta\omega_i}$ for each line. The approximation of the detuning trajectory can be expressed by the following piecewise defined function for $\Delta\omega(t)$:

$$\Delta\omega(t) \approx \begin{cases} \Delta\omega_0 + d_{\Delta\omega_1}(t - t_0) & : \quad t_0 \leq t \leq t_{fill} \\ \Delta\omega_0 + d_{\Delta\omega_1}(t_{fill} - t_0) + d_{\Delta\omega_2}(t - t_{fill}) & : \quad t_{fill} \leq t \leq t_{flat} \\ \Delta\omega_0 + d_{\Delta\omega_1}(t_{fill} - t_0) + d_{\Delta\omega_2}(t_{flat} - t_{fill}) + d_{\Delta\omega_3}(t - t_{flat}) & : \quad t_{flat} \leq t \leq t_{end} \end{cases}$$

The time intervals are defined according to Figure 4.6. The predetuning $\Delta\omega_0$ is adjusted by the operators at TTF2 such that the detuning has a zero crossing during the flat top phase. The adjustment is done by stepper-motors mounted onto the cavities that apply forces on the structure thus changing their length.

4.3 Results of parameter estimation for physical cavity model

By equation (4.29) an LPV model for the behaviour of a superconducting cavity is described:

$$\begin{pmatrix} \dot{V}_r \\ \dot{V}_i \end{pmatrix} = \begin{pmatrix} -\omega_{1/2} & -\Delta\omega(t) \\ \Delta\omega(t) & -\omega_{1/2} \end{pmatrix} \begin{pmatrix} V_r \\ V_i \end{pmatrix} + R\,\omega_{1/2} \begin{pmatrix} 1 & 0 \\ 0 & 1 \end{pmatrix} \begin{pmatrix} I_r \\ I_i \end{pmatrix}.$$

The model has been derived in chapter 4.1. To calculate the deviation of the model output from measured data an OE model structure (see figure 4.7) containing the electrical and mechanical models discussed previously is implemented in SIMULINK. A description of an output error model can be found in chapter 3.1.1.

In the OE structure the parameters are included which are not precisely known (like mechanical time constants τ_m). The goal of the simulations performed with the SIMULINK model is to proove whether the model structure is appropriate. The parameters contained in the model structure (included in the parameter vector $\boldsymbol{\theta}$) are estimated by optimization routines based on genetic algorithms and direct search methods that minimize a cost functional depending on the unknown parameters: The weighted sum of squared errors between model output ($\hat{\boldsymbol{y}}(t)$) and measurement data ($\boldsymbol{y}(t)$) is taken over the sampling instants k of one RF-pulse as a cost functional that denotes the quality of the model in an OE sense. The functional can be written as

$$J(\boldsymbol{e}, \boldsymbol{R}) = \sum_k \boldsymbol{e}_k^T \boldsymbol{R} \boldsymbol{e}_k \tag{4.37}$$

where the error vector $\boldsymbol{e}_k$ is defined for each sampling instant as

$$\boldsymbol{e}_k = \hat{\boldsymbol{y}}_k - \boldsymbol{y}_k \tag{4.38}$$

and $\boldsymbol{R}$ denotes a weighting matrix for the errors of different output channels. In this case, $\boldsymbol{R} \in \mathbb{R}^{2\times 2}$ is a diagnonal matrix weighting the errors of the real and imaginary part of the fields voltage vector.

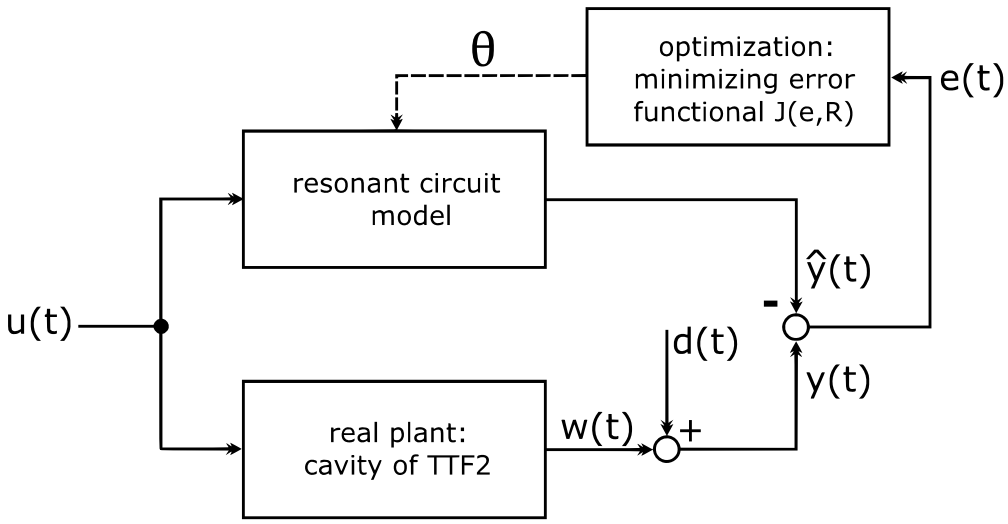

Figure 4.7: Output error model for the parametrization of the resonant circuit model

Signals used for the model parametrization process

In chapter 2.2.4 parts of the calibration procedure for the measurement signals to compensate influences of cable impedances etc. have already been explained. The signal flow of

the input and output signals of one cavity is shown in figure 4.8. The RF-power resulting from the complex generator current $\boldsymbol{I} = I_r + iI_i$ for the supply of the electromagnetic fields is guided by a transmission system based on waveguides to the coupler. The real and imaginary parts of the input current of the test data set is shown in figure 4.9. By the coupler the RF-waves are transported into the cavity.

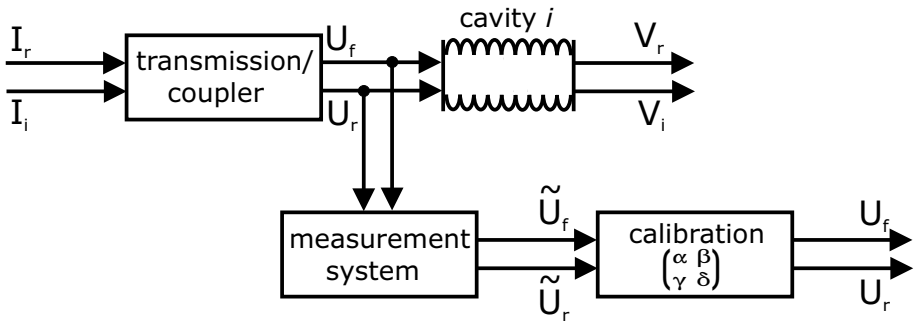

Figure 4.8: Measurement and calibration setup for each cavity in TTF2

A part of the RF-power supplied to the cavity is reflected at the coupler. The amount of power reflected at the coupler depends on properties of the coupler and the presence of the electron beam inside the cavity (for more details see [20]). Therefore, two input signals are distinguished: The *forward* signal which supplies the main part of the field inside the cavity and the *reflected* signal, which is reflected by the cavity. The resultant field inside the cavity is determined by the *crosstalk*, i.e. the interaction, between forward and reflected field that occurs in various hardware elements, about 5% crosstalk occurs in the so called *directive couplers*.

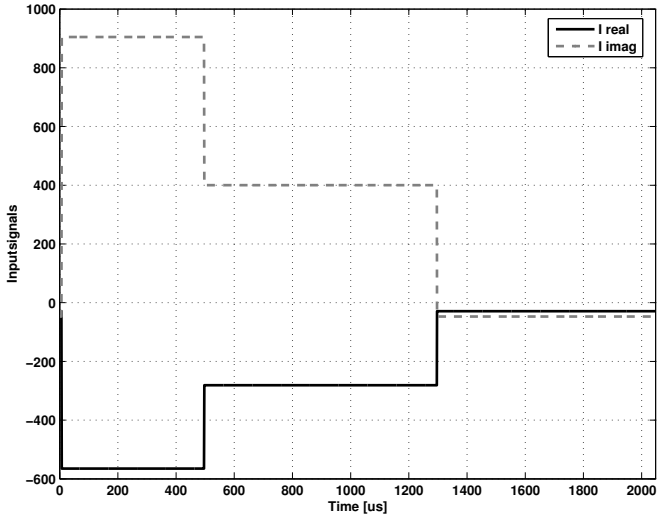

Figure 4.9: Vectormodulator input signals I_r and I_i

Forward and reflected signals are measured (see figure 4.8) but are modulated in amplitude and phase by the transfer behaviour of the measurement system. To recover the "true" $\boldsymbol{U}_f$

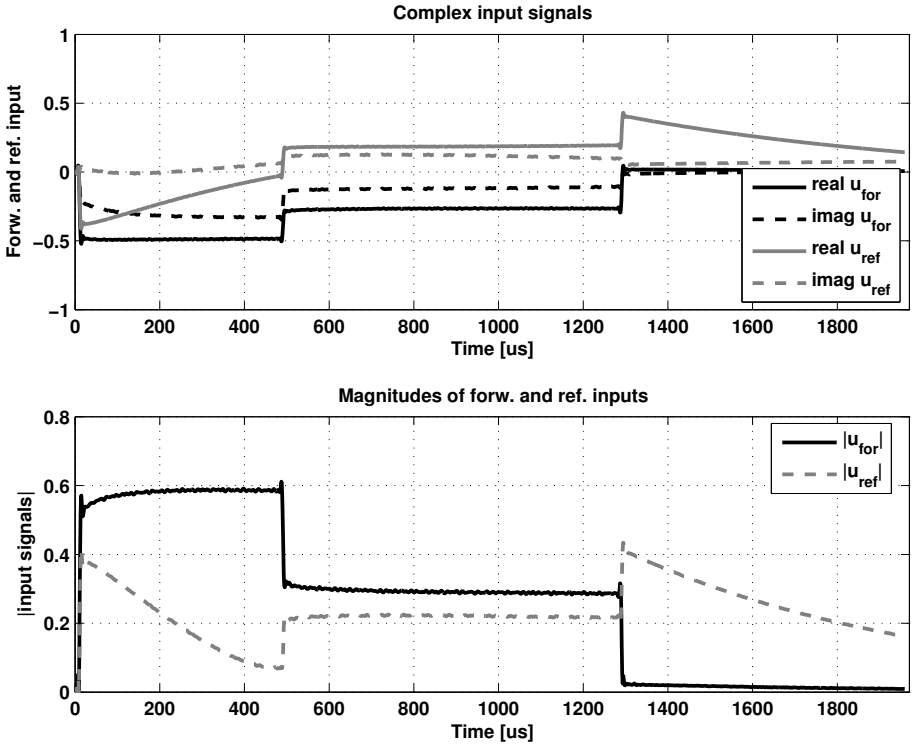

Figure 4.10: Forward ($\tilde{\boldsymbol{U}}_f$) and reflected $\tilde{\boldsymbol{U}}_r$) signals as real and imaginary parts in upper figure and magnitudes of the complex signals in lower figure

driving the cavity, transformation

$$\begin{pmatrix} \boldsymbol{U}_f \\ \boldsymbol{U}_r \end{pmatrix} = \begin{pmatrix} \alpha & \beta \\ \gamma & \delta \end{pmatrix} \begin{pmatrix} \tilde{\boldsymbol{U}}_f \\ \tilde{\boldsymbol{U}}_r \end{pmatrix}, \tag{4.39}$$

is used for calibration where $\alpha, \beta, \gamma, \delta \in \mathbb{C}$.

Thus, assuming that the resultant field in the cavity is a function of the forward power $\boldsymbol{U}_f$ the following relation is used: The actual forward signal driving the field in the cavity equals the sum of the calibrated measured values of forward ($\tilde{\boldsymbol{U}}_f$) and reflected ($\tilde{\boldsymbol{U}}_r$) signals. With $\alpha = a + ic$ and $\beta = b + id$ this complex scaling of the forward signal can be expressed as

$$\boldsymbol{U}_f = (a + ic)\tilde{\boldsymbol{U}}_f + (b + id)\tilde{\boldsymbol{U}}_r\,. \tag{4.40}$$

Using real and imaginary part of $\boldsymbol{U}_f$ as the new input signal, eq.(4.29) becomes

$$\begin{pmatrix} \dot{V}_r \\ \dot{V}_i \end{pmatrix} = \begin{pmatrix} -\omega_{1/2} & -\Delta\omega \\ \Delta\omega & -\omega_{1/2} \end{pmatrix} \begin{pmatrix} V_r \\ V_i \end{pmatrix} + R\,\omega_{1/2} \begin{pmatrix} \mathcal{R}\left\{(a + ic)\tilde{\boldsymbol{U}}_f + (b + id)\tilde{\boldsymbol{U}}_r\right\} \\ \mathcal{I}\left\{(a + ic)\tilde{\boldsymbol{U}}_f + (b + id)\tilde{\boldsymbol{U}}_r\right\} \end{pmatrix}. \tag{4.41}$$

The optimal scaling parameters are estimated by the optimization algorithm used to minimize the sum of squared errors of the OE model. The uncalibrated input data is shown in figure 4.10.

Moreover, two important points for the parameter estimation done shall be mentioned:

1. No continuity equation like

$$|\boldsymbol{U}_f + \boldsymbol{U}_r| = \sqrt{V_r^2 + V_i^2} = |\boldsymbol{V}|$$

is included, which would not be correct in a strict physical approach. However, simulations with such a continuity boundary condition have been done resulting in very high output error functional values and thus bad model performance. The calibration should not be the focus of the model parametrization tests but the model structure of the resonant circuit model.

2. The measurement signals used are not normalized to physical units because the raw measurement data has been used recorded by the DSP system. The output error functionals have been calculated for the unscaled data as well to ensure comparability with the output error functionals used for evaluation of the models developed via system identification. Because the parameters of the resonant circuit model are physically interpretable, the estimated values are listed in the tables 4.2 and 4.1 with the appropriate units to compare the numerically estimated values, e.g. of the bandwidth, with known values. The diagrams showing output data (Figures 4.12 and 4.13) have been scaled according to the adjusted gradient of 14MV/m during flat top by the value 0.005 in order to visualize the parameter estimation results more clearly and their values approximately correspond to field gradients in MV/m.

Detuning trajectory

Two different detuning trajectories are used for the simulation of the resonant circuit OE model: The continuous piecewise linear approach for each of the three time intervals filling, flat top and decay as described in chapter 4.2. The curve is characterized by four parameters: An initial value (predetuning) and 3 slopes (one per interval).

The second approach is an ordinary differential equation for the detuning as proposed by [11]. This approach has been presented in chapter 4.2 as well (see equation 4.36). Here, only one mechanical mode is taken into account

$$\begin{pmatrix} \Delta\dot{\omega}_1 \\ \Delta\ddot{\omega}_1 \end{pmatrix} = \begin{pmatrix} 0 & 1 \\ -\omega_1^2 & -\frac{1}{\tau_1} \end{pmatrix} \begin{pmatrix} \Delta\omega_1 \\ \Delta\dot{\omega}_1 \end{pmatrix} + 2\pi \begin{pmatrix} 0 \\ -K_1\omega_1^2 \end{pmatrix} \cdot \mathbf{V}^T\mathbf{V}\,. \tag{4.42}$$

Equation (4.42) has three free parameters ω_1, τ_1 and K_1, which are estimated by the optimization algorithm to minimize the error functional of eq. (4.37).

4.3.1 SIMULINK block diagram

With the structure of the detuning trajectory the modified cavity state space model of equation 4.41 can be implemented in SIMULINK as shown in figure 4.11. Because the (real) resistance R in the state space equation only scales the input signals and a scaling is already done by the calibration of the input signals, the resistance is normalized to $R = 1\Omega$.

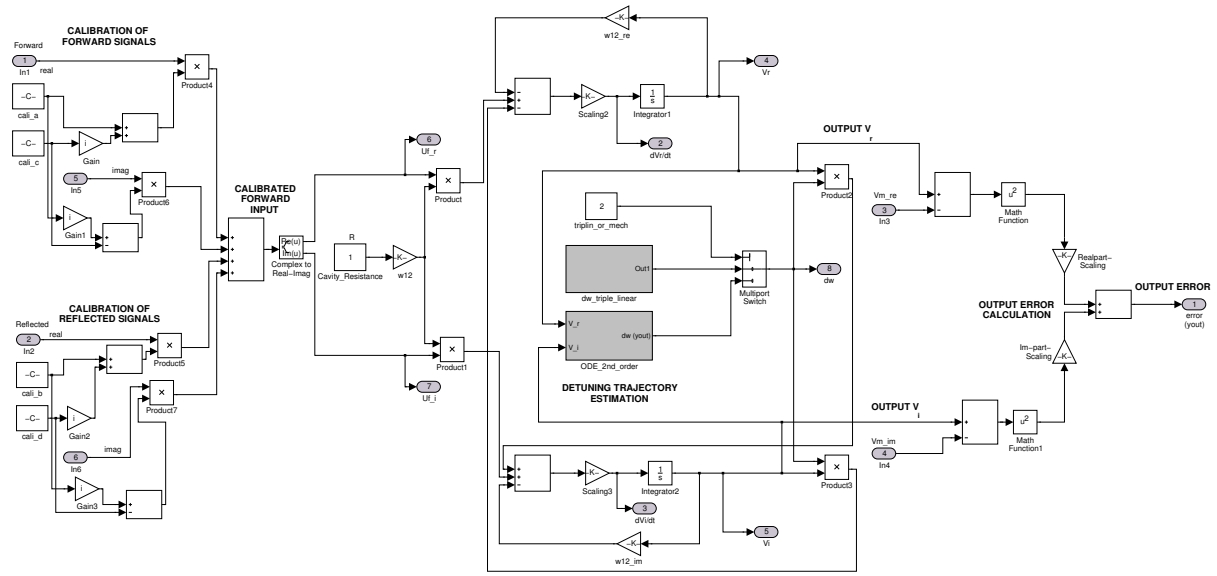

Figure 4.11: SIMULINK output error model for resonant circuit model

4.3.2 Parameter estimation

The free model parameters (9 for the partwise linear detuning approach, 10 for the differential equation approach) are tuned by an optimization algorithm that minimizes the error functional J iteratively. This means that for each parameter vector $\boldsymbol{\theta}$ a simulation run is done and the parameter vector is updated unless the minimum is reached.

To increase the chance the minimum reached at the termination of the algorithm is the absolute minimum of the cost functional J two different optimization methods are combined: A Genetic algorithm (GA) based search method and a direct search based method[2]. The GA based search method is used to determine initial values for the parameters because GA based routines have a lower possibility to get stuck in local minima like gradient based search methods. Direct search based routines usually estimate a minimum with higher absolute accuracy than GA based methods. In the parameter estimation problem at hand the initial values of the parameters are estimated with the GA based method. With this initial values the direct search method is used to locate the minimum.

The weighting matrix $\boldsymbol{R}$ in eq. (4.37) is choosen to be the unity matrix because the model must describe both output channels with equal accuracy.

$$\boldsymbol{R} = \begin{pmatrix} 1 & 0 \\ 0 & 1 \end{pmatrix} .$$

The starting values and estimated optimal values of the simulation parameters are presented in table 4.1 (for partwise linear detuning) and in table 4.2 (for detuning trajectory modelled

[2]Exemplary MATLAB Commands: `ga` for GA and `fminsearch` for direct search based methods that uses a simplex search method, [2]

Table 4.1: Estimated parameters for simulations with partwise linear detuning

Paramter	**Initial value (GA)**	**Estimated optimal value**
Predetuning $\Delta\omega_0$ [rad/s]	4.644	71.103
Scaling factor a	-5.705	20.642
Scaling factor b	8.853	66.245
Scaling factor c	-16.558	-70.660
Scaling factor d	5.095	-37.939
Half-Bandwidth ω_{12} [rad/s]	22.276	818.515
Detuning slope (filling) [Hz/s]	-5.977	189.209
Detuning slope (flat top) [Hz/s]	-2.021	18.714
Detuning slope (decay) [Hz/s]	1.024	6.485

by differential equation). For the predetuning $\Delta\omega_0$ the constraint has been applied that only positive values are permitted. The reason is that the cavities are stretched when the RF-field is applied such that the resonance frequency is lowered and the detuning decreases.

4.3.3 Comparison of simulation and measurements

The data for the model parameter estimation has been measured at cavity 6 of the accelerator module 1 (ACC1)[3]. The flat top gradient has been adjusted for 14MV/m. Simulations for other cavities have been done as well and the results were similar.

The figures 4.12 and 4.13 show the scaled measured and simulated output signals of the cavity. Displayed is the real (V_r) and imaginary part (V_i) of the cavity field voltage vector.

Both results are obtained with the combination of GA and direct search based parameter estimation method. The resulting functional values at which the optimization algorithm converged are:

- Partwise linear detuning: $J(\boldsymbol{e}, \boldsymbol{R}) = 1.14332 \cdot 10^8$

[3]Dataset: `30-Sep-2005T10-03-00gkoch-data.mat`

Table 4.2: Estimated parameters for simulations with detuning as differential equation

Paramter	**Initial value (GA)**	**Estimated optimal value**
Predetuning $\Delta\omega_0$ [rad/s]	-0.278	0.000
Scaling factor a	-3.619	19.12
Scaling factor b	14.297	50.145
Scaling factor c	-15.526	-62.013
Scaling factor d	1.299	-23.670
Half-Bandwidth ω_{12} [rad/s]	20.389	1020.894
Natural mech. freq. ω_1 [rad/s]	$2\pi \cdot 3.347$	$2\pi \cdot 4.507$
LFD constant K_1	-0.209	1.276
Mech. time constant τ_1 [s]	$9.769 \cdot 10^{-6}$	$1.032 \cdot 10^{-3}$

- 2. order differential equation (ODE) for detuning: $J(\boldsymbol{e}, \boldsymbol{R}) = 1.11496 \cdot 10^8$

The model output looks reasonable in the large signal behaviour, e.g. by the sign equivalence of the signals slopes in most of the intervals except in parts of the flat top. During the flat top the largest deviations between model and measured output data are visible. Moreover, it can be seen that the real part of the output signal can be better reproduced by the model than the imaginary part. Although the cost functional of the model with the ODE for the detuning has a lower value, the model outputs for both detuning trajectories look very similar.

The estimated partwise linear detuning curve (figure 4.12) does not look like the expected shape (figure 4.6) with negative slopes during filling and flat top phase and a zero-crossing of the detuning during the flat top. The detuning even increases during the flat top phase.

The shape of the detuning obtained for the ODE model rather resembles the expected trajectory. However, if physical units would be considered the order of magnitude of the estimated detuning is very low (in the range of mHz). The increase of the detuning starts already in the flat top interval not during decay.

For the comparison of the estimated parameters they are assumed to be normalized to the physical values they have in the resonant circuit model. Taking a look at the parameters obtained by the parameter estimation methods leads to significant results:

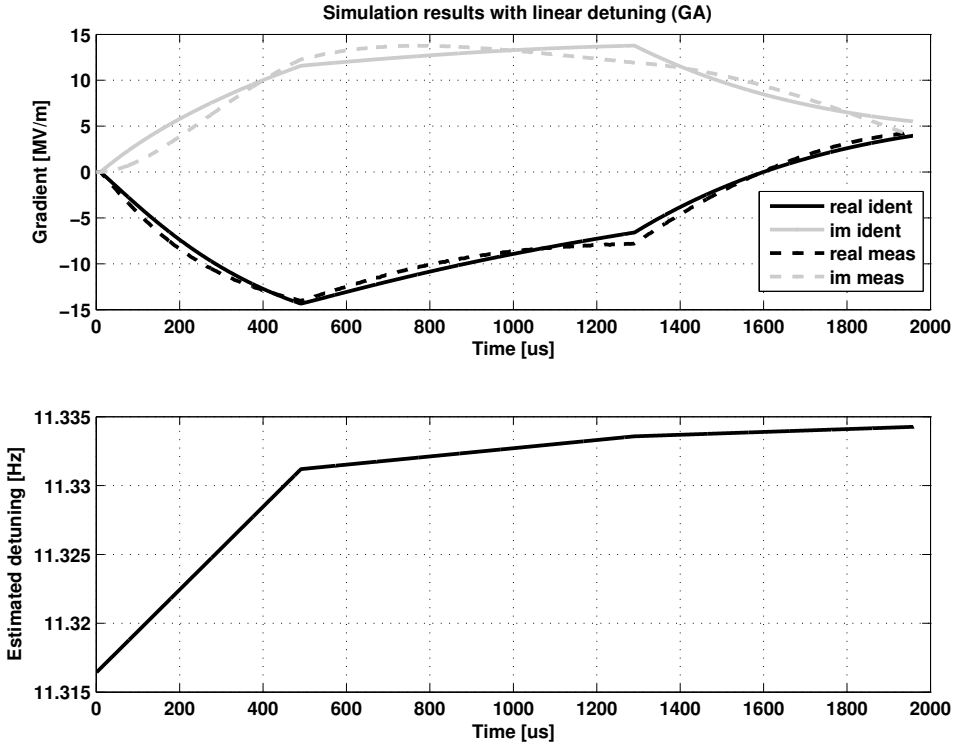

Figure 4.12: Scaled (scaling factor: 0.005) simulation results for linear approximated detuning with GA and gradient based parameter search methods for 9 parameters: The upper diagram shows the comparison between measured and simulated output data, the lower diagram shows the estimated detuning curve

- The predetuning $\Delta\omega_0$ in the simulations with this recent measurement data has never been estimated to be higher than approx. 11 Hz. That is an odd result because the predetuning of the cavities should be in the range of approx. 200 Hz, [11]. Giving a higher predetuning value as an initial value for the gradient based optimization, the estimated optimal parameter is in the range of 0-12 Hz again. Thus the sensitivity for the initial value can not cause the low estimated predetunings.

- Although the initial value for the cavity bandwidth $\omega_{1/2}$ has been estimated by the GA algorithm to be quite low (ca. 20 Hz) the final estimated value lies in the range from 130 Hz to 162 Hz which is closer to the specified bandwidth of 216.7 Hz. An important point is that a constant bandwidth during the RF-pulse is an assumption in the resonant circuit model. Due to mechanical and thermal disturbances deviations in this parameter could make sense.

- The signs and values of the scaling parameters are physically not interpretable because a continuity condition for the sum of forward and reflected input signals whith respect to the measured vector sum signals has not been applied. The parameters are in this context purely seen as vehicles for adjusting the fit.

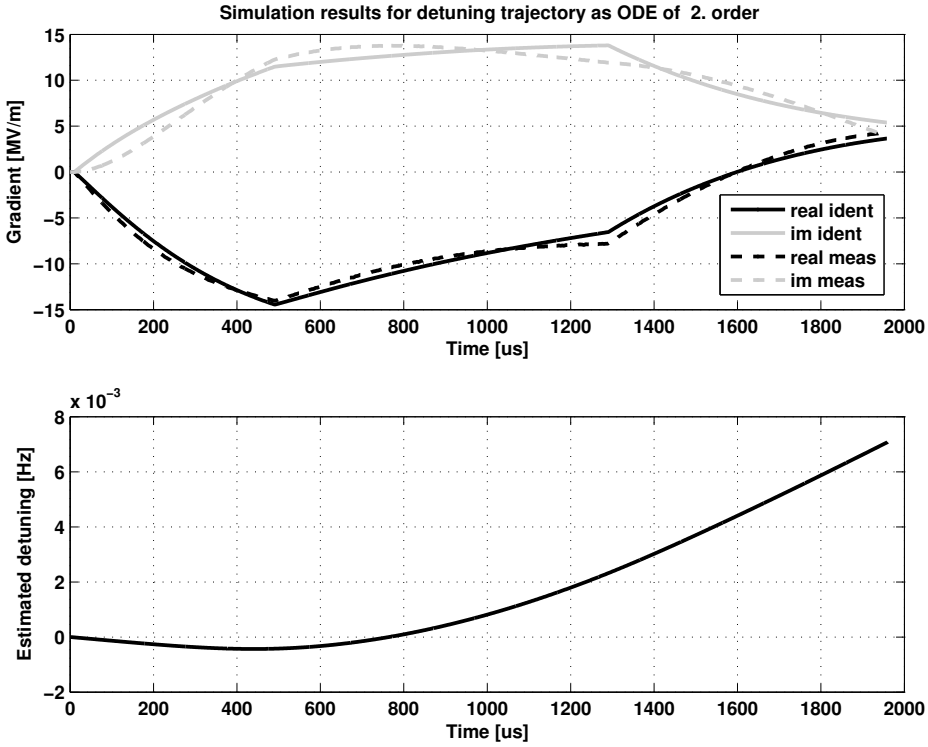

Figure 4.13: Scaled (scaling factor 0.005) simulation results with detuning modelled by second order differential equation and GA and gradient based parameter search methods for 10 parameters: The upper diagram shows the comparison between measured ans simulated output data, the lower diagram shows the estimated detuning curve

Both parameter estimations (piecewise linear detuning and detuning modelled by ODE) have been done with purely direct search based parameter estimation methods and physically reasonable initial values for the parameters (except the scaling parameters) as well. This has been a way to test if the initial parameters found by the GA based optimization method nevertheless led to local minima and therefore unreasonable trajectories of output signals and detuning. The values of the cost functional however were higher for both detuning trajectory models, namely $J(\boldsymbol{e}, \boldsymbol{R}) = 5.277 \cdot 10^8$ (partwise linear detuning) and $J(\boldsymbol{e}, \boldsymbol{R}) = 2.048 \cdot 10^8$ (ODE for detuning).

4.3.4 Conclusion of the results

Modelling based on physical insight into a system becomes more difficult the more complex the system is. For a lot of control applications the I/O behaviour of the models shown in the figures 4.12 and 4.13 would be sufficiently accurate in an output error model sense when it is compared with the measurement data. The lowest achieved cost functional value has been $J(e, \boldsymbol{R}) = 1.14332 \cdot 10^8$ for the parametrization of the resonant circuit model including one mechanical mode for the detuning. The reasons for the deviations between

simulated and measured data need not necessarily be the structure of the LPV model but the simplified approach of crosstalk modelling. Crosstalk can occur in several parts of the hardware and certainly these effects can not be reconstructed from measured forward and reflected power at the couplers.

The severe control objectives for the XFEL though require model based high performance controller design for the RF-fields in the cavities. That means the model structure mainly influences the controller structure and the performance of the controller is directly related to the quality of the model in the frequency range and operating point of interest for control.

Because the XFEL control objectives are formulated only for the flat top, models are needed that resemble the plant behaviour very accurately in an OE model sense especially during the flat top interval. As discussed in the previous section, this is the interval where the resonant circuit model apparently describes the cavity behaviour rather poorly, especially the imaginary part of the output signals.

From a control application point of view the LPV resonant circuit model of the cavity is less suitable for controller design than an LTI model (see chapter 3 for details). If it is possible to find an LTI model describing the behaviour of the TTF2 plant, a variety of high performance controller design methods will be applicable. This implies that the time varying detuning effect has to be considered as a disturbance. In the next step, system identification methods (described in chapter 3.3) are used to develop models for the RF-field behaviour at ACC1 such that the performance of the identified models can be compared to the results with the resonant circuit model structure.

Chapter 5

RF system identification of ACC1

In section 3.3 the fundamentals of the experimental based way of modelling via system identification have been illustrated. In this chapter the system identification of the first accelerator module ACC1 is presented. First, the modelling goals are formulated in Section 5.1 with respect to the gradient and frequency range the models shall describe the I/O behaviour of the system accurately. Section 5.2 describes the design of the system identification experiments, especially the choice of appropriate input signals to receive sufficiently informative measurement data from the system. Moreover, the recorded data is analyzed with respect to high frequent noise sources and time delay between input and output signals.

The recorded data is used to parametrize model structures. The I/O behaviour models to be developed shall especially describe the flat top phase accurately. In the Sections 5.3 and 5.4 the obtained models are presented while two classes of estimated models are distinguished:

- Models with an additional input signal that has been estimated in the identification process. This signal should resemble parameter disturbances e.g. caused by detuning of the superconducting cavities.
- Multivariable state space models in which all disturbance signals are considered output disturbances.

All models presented here are LTI models which makes them well applicable for a variety of high performance controller synthesis methods. The modelling focus on the controller design also implies that only models for the vector sum of the field signals of ACC1 (eight superconducting cavities) are developed because these are the plant outputs to be controlled.

5.1 Modelling goals

Crucial for the free electron laser system at DESY are stable (regarding their amplitude and phase precision) electromagnetic fields in the cavities during the flat top. Because the TTF2 system is *underactuated* (see Chapter 2.2.2) the real and imaginary part of the vector sum of the cavity field signals are the output signals to be controlled. On the one hand, accurate models for the *small signal behaviour*, i.e. in this case for the vector sum I/O behaviour during the flat top phase, are needed for the synthesis of model based RF-field controllers satisfying the severe control objectives that have been formulated to make the XFEL project successful. On the other hand, the *large signal behaviour*, i.e. the behaviour of the vector sum output trajectories during the RF-pulse should be resembled in models. This is of interest because in the present system configuration overshoot in the RF-field vector sum amplitudes and phases occurs at the beginning of the flat top interval due to a step change in the feedforward signals. With a model describing filling and flat top dynamics, a control strategy could be developed that minimizes this overshoot. The models shall describe the behaviour of the RF-fields without presence of the electron beam. The beam would lead to major disturbances because the RF-fields supply energy to the electrons. Developing disturbance models including beam induced RF-field transients will be part of future work.

Range of covered operating points and frequency range

The models have been inferred on the basis of data recorded for gradients from about $13\frac{MV}{m}$ to $15.6\frac{MV}{m}$. The main operating point during the system identification experiments has been set to $14\frac{MV}{m}$ which is comparable with the gradient used when the accelerator system operates as part of the free electron laser system. The gradient range covered by the models should mainly focus of the interval from about $13\frac{MV}{m}$ to $14\frac{MV}{m}$. In Figure 5.1 measured vector sum output signals are shown for different gradients. It can be seen that the trajectory shapes look very similar despite of the different levels.

The small signal I/O behaviour model for the flat top should cover a frequency range up to 100kHz to include information of mechanical modes but exclude high frequent measurement noise. The large signal I/O behaviour of the system is mainly determined by the comparatively low bandwith of the cavities ($\omega_{1/2} = 2\pi \cdot 216.7\text{Hz}$).

5.2 Experimental setup

5.2.1 Design of experiments

The experimental measurement setup used for the system identification of the TTF2 linear accelerator system is shown in figure 5.2. The test setup involves the first accelerator

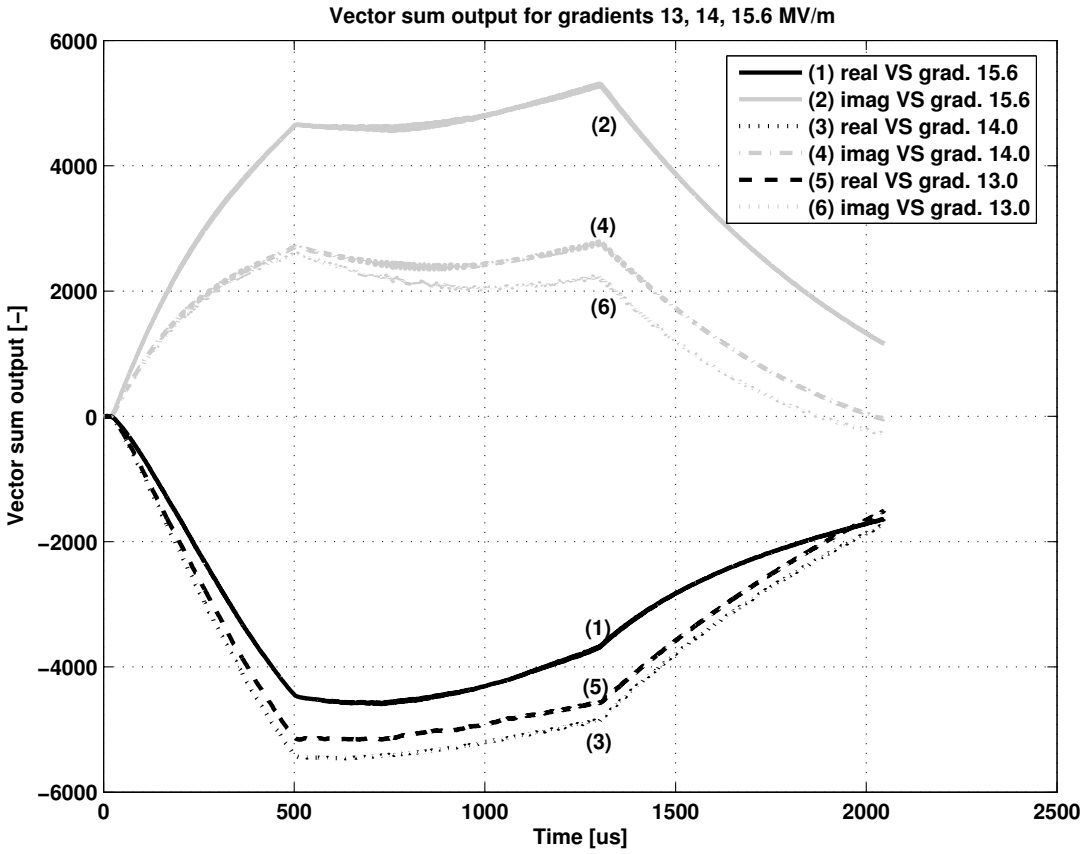

Figure 5.1: Measured vector sum outputs for different gradients

cryomodule (ACC1) of the TTF2 system. In ACC1, eight superconducting nine-cell-cavities are housed, which are driven by one klystron (klystron number 2). The actuator system includes the elements vector modulator, two pre-amplifiers (PA1 and PA2) and the klystron. The RF-gate can be considered a switch that enables the high power amplification of the low-level RF-signals.

As input signals, the real and imaginary parts I_r and I_i of the vectormodulator driving signal are used. All measurements are done in open-loop to identify only the plant behaviour. A variety of signals within the experimental setup is measured to obtain a widespread database for further analysing the system. The main focus regarding these output signals is put on the complex vector sum signal of the eight cavities and on the forward, reflected and probe signals of each individual cavity.

The recorded output data is the calibrated data of each cavity, i.e. the original data multiplied by the rotation/scaling matrix at the output of each cavity. The calibration coefficients have been recorded as well.

Signal units and model normalization

All signals described in the context of system identification in this chapter are not scaled

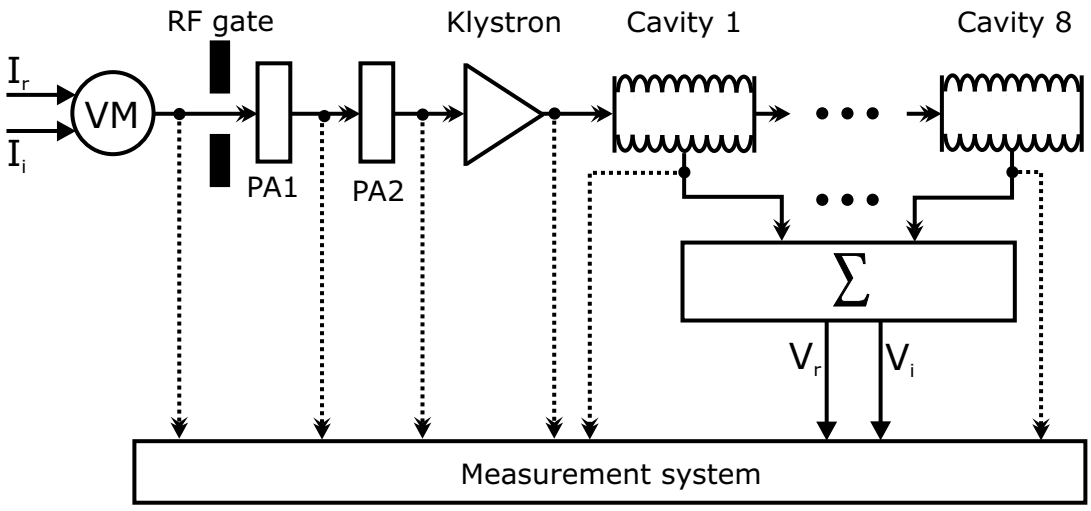

Figure 5.2: Measurement setup for the system identifivation of TTF2. Dotted lines denote measured signals, continuous lines resemble the signal flow in the accelerator system from vector modulator input to vector sum output

by physical units. The normalization of the signals to physical units is not done by the measurement system used at TTF2. Because such a normalization would require more insight into the measurement setup, only the values, that are read out of the measurement system, are used for the data analysis.

This implies that all models developed here by system identification are not normalized to physical units as well. They refer to the raw measurement data recorded via the DSP system.

5.2.2 Input signals

The input signals are applied to the system according to the *feed-forward reference tables*. The standard step profile of the feed-forward table for the real and imaginary input channel is normalized such that the maximum absolute value is one. The obtained normalized table is called *feed-forward reference table*. The mean value and amplitudes of the test signals described in this section refer to the maximum of the reference value. This means for example that a signal amplitude of $\hat{u} = 0.15$ has 15% of the maximum amplitude of the standard piecewise constant feedforward profile that is presented in chapter 2.2.6.

The purpose of the reference tables is that they are scaled automatically by the signal processing system such that the defined flat top operating gradient is reached. To excite the system, the signals have to satisfy two main requirements:

- They must be applicable to the system. That means that the signal level and frequency range must be within the operating range of the actuators (see chapter 2.2.8

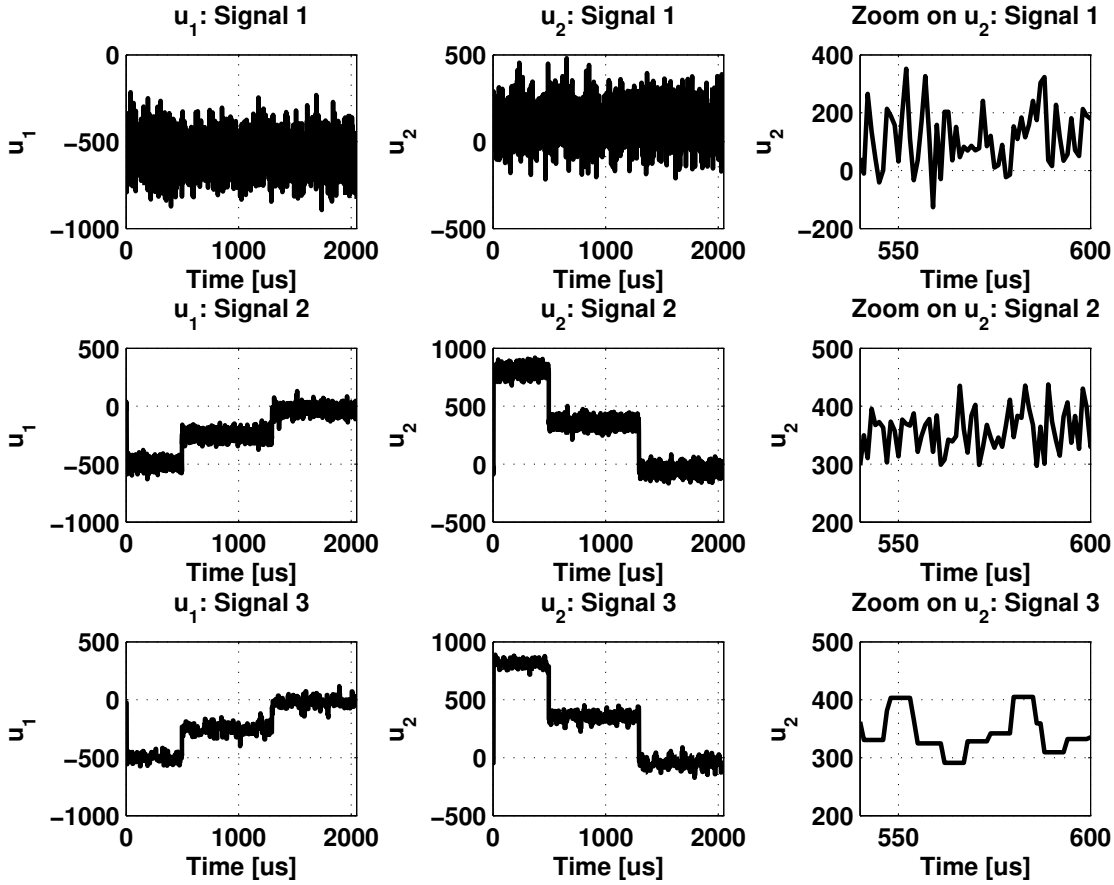

Figure 5.3: Input signals for field gradients of $14\frac{MV}{m}$

for a detailed specification of the actuator constraints). If the amplitudes exceed these levels, either the preamplifiers are overdriven or - in the worst case - the klystron could be damaged.

- The signals must fulfill the excitation condition described in chapter 3.3.2 in order to make the experiments informative enough for model building. Especially the small signal behaviour during the flat top must be revealed by appropriate excitation signals.

Mainly, three different types of input signals are used for the identification experiments that are shown in figure 5.3 and are characterized in table 5.1. Bandlimited white noise has been choosen as input signal for both channels. The order of persistency of excitation of white noise signals can be arbitrary high as shown in chapter 3.3.2.

To basically investigate the large signal cavity behaviour, a noise signal with a bandwidth of $f = 1\text{MHz}$, a relative[1] mean value of $u_0 = 0.4$ and an amplitude of $\hat{u} = 0.15$ is applied during the whole pulse (signal 1). For the identification of the signal behaviour along the filling and flat top trajectories (without feedback), the step-profile of the feedforward

[1]relative with respect to the feedforward reference table

Table 5.1: Inputs signals for system identification

Signal number	Signal type	Comment
1	Bandlimited white noise during whole pulse	Relative mean value: 0.4 Noise amplitude: 0.15 Gradient: 8.8 - 14.25$\frac{MV}{m}$ Bandwidth: 1MHz
2	Superimposed noise on feedforward tables	Noise amplitude: 0.15 Gradient: 12.0 - 15.6$\frac{MV}{m}$ Bandwidth: 1MHz
3	Bandlimited noise superimposed on feedforward tables	Noise amplitude: 0.15 Gradient: 14.0 - 15.6$\frac{MV}{m}$ Bandwidth: 200kHz

tables (see chapter 2.2.6) is used. During the filling and flat top bandlimited white noise is superimposed on the feedforward table profile to excite small signal dynamics (signals 2 and 3). The bandwidth of the noise of signal 2 is $f = 1$MHz while signal 3 has a bandwidth of $f = 200$kHz to emphasize the excitation of lower frequent dynamics. The noise is generated for both input channels seperately to provide that their signals are uncorrelated.

5.2.3 Analysis of exemplary measurement data

In figure B.1 exemplary vector sum signals as responses to the applied input signals are shown. The feedforward reference tables have been scaled to a field gradient of 14.0 MHz.

For signal 1 (bandlimited noise with a fixed mean value) only a filling profile can be seen for the field gradients because the input signals have a constant mean value during the RF-pulse. For the input signals 2 and 3 the gradient trajectories become the classical three phase trajectories (filling, flat top and decay) but their flat tops are perturbed by high frequent noise in the frequency range from 0.1MHz to 1MHz as well as low frequent disturbances in the 1-10kHz range (e.g. caused by Lorentz force detuning).

In figure 5.4 the power spectra of an input signal of type three and the measured output data is shown. A dominant high frequency disturbance can be seen at 250 kHz which is caused by the local oscillators in the downconverter system (see chapter 2.2.4). The grey lines in Figures C.1 and C.2 show the spectra of the real and imaginary input and output signals in logarithmically scaled periodograms.

Investigations regarding time delay τ have been done using cross-correlation of the input and output signals during the flat top phase (see figure B.5). Cross-correlation analysis for system identification is described in [8]. The maximum of the cross-correlation function gives the time delay between input and output signals. The flat top phase has been chosen for these investigations for two reasons: Synchronisation problems can occur at the

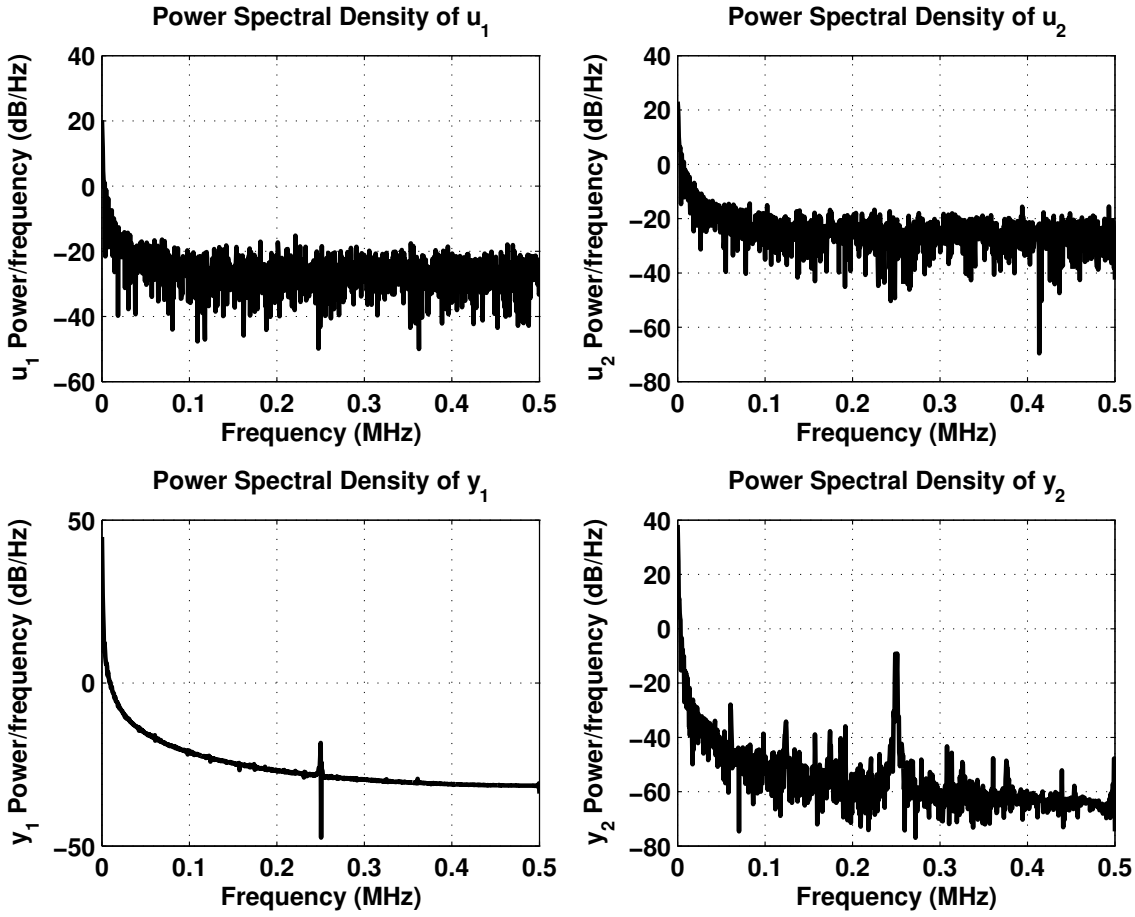

Figure 5.4: Power spectrum density of input signals $u_1 = I_r$, $u_2 = I_i$ and output signals $y_1 = V_r$, $y_2 = V_i$ for input signal 2 (see table 5.1)

beginning of the data recording (before the filling phase starts) due to monitoring system problems leading to errors in the delay calculation and the flat top is the interval the models shall describe most accurately. The result is that the maximum of the cross-correlation function is at $\tau = 0$ and thus no delay has been assumed for the models.

Model name convention

The name convention shown in table B.1 is introduced to classify the developed models. The resulting abbreviations will be helpful for comparisons of models. According to this convention the modelname $GLDB9_x2_u2_y$ would classify a "global linear discrete time black box model with 9 states, 2 inputs, 2 outputs and no disturbance input".

5.3 Model with estimated third input

The first approach for the modelling by system identification is to incorporate aspects of the resonant circuit model structure (see Chapter 4.1) in grey box models. The main aspect is the parameter disturbance caused by the detuning, which is a time varying parameter in the resonant circuit model. In [20] the detuning trajectory during an RF-pulse has been described as a concave curve and in Section 4.2 the approximation of the detuning trajectory by three continuous lines has been presented.

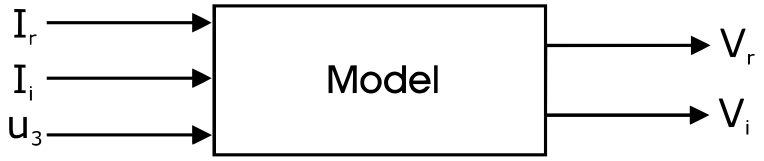

Figure 5.5: Model of the accelerator module ACC1 with additional third input

To incorporate the parameter disturbance that influences the system behaviour a third input signal u_3 is implemented in the model structure (see Figure 5.5). The parametrization of the third input is done by parameter estimation routines that minimize an output error functional including the sum of quadratic errors.

An important point is the discussion about the interpretability of this signal in a physical sense. The signal can certainly not be interpreted as the frequency shift in Hertz of one or several cavities because only limited restrictions considering physical aspects are given for its parameter estimation. However, strictly speaking the term detuning does not make sense anyway when dealing with the vector sum of several cavity field signals because the frequency shifts of several cavities can not simply be added and a "resulting" detuning of ACC1 is not physically interpretable. The sense of the signal u_3 is to resemble a parameter disturbance $p(t) = u_3(t)$ (see Chapter 3.1) of the system, not by varying the system parameters themselves but via an additional input.

For the modelling with an estimated third input two approaches are made: In the first approach the parameter disturbance of the cavities is considered as a system state, i.e. an internal variable. If the trajectory of this state should have the partwise linear shape, several constraints have to be included in the model structure and the shape of the additional input signal $p(t)$. This grey box approach is described in section 5.3.1. The second appoach uses black box modelling and the parameter disturbance is directly resembled in the input signal which leads to a partwise linear shape of $p(t)$ itself. The models obtained by this approach are presented in the Sections 5.3.2 and 5.3.3. Validation, i.e. the test of the model performance with another data set than the one used for the parameter estimation, shows that the resulting models are sufficiently accurate in the sense of residual output error functionals $J(e, \boldsymbol{R})$ for the RF-pulse. The weighting matrix R has for all parameter estimation algorithms used for system identification of ACC1 been choosen to be

$$\boldsymbol{R} = \boldsymbol{I}^{2\times 2}\,. \tag{5.1}$$

The measurement data has not been preprocessed (e.g. filtered or detrended) for this way of modelling because this approach mainly focusses on low order large signal behaviour models. Removing the trends in this case would alter the large signal behaviour and low pass filtering is not necessary because the model order is too low to follow the high frequent disturbances in the range of 250kHz.

5.3.1 Modelling with constraints

The idea for resembling the partwise linear parameter disturbance as a state is to use a piecewise constant trajectory for the input signal u_3 and enforce parametrization constraints in the model structure such that the input signal is integrated and the state trajectory is partwise linear and continuous. The input signal is characterized by three parameters θ_i, namely the step height for each of the three intervals filling, flat top and decay. This implies for the dimension of the parameter vector $\boldsymbol{\theta} \in \mathbb{R}^{(3\times 1)}$.

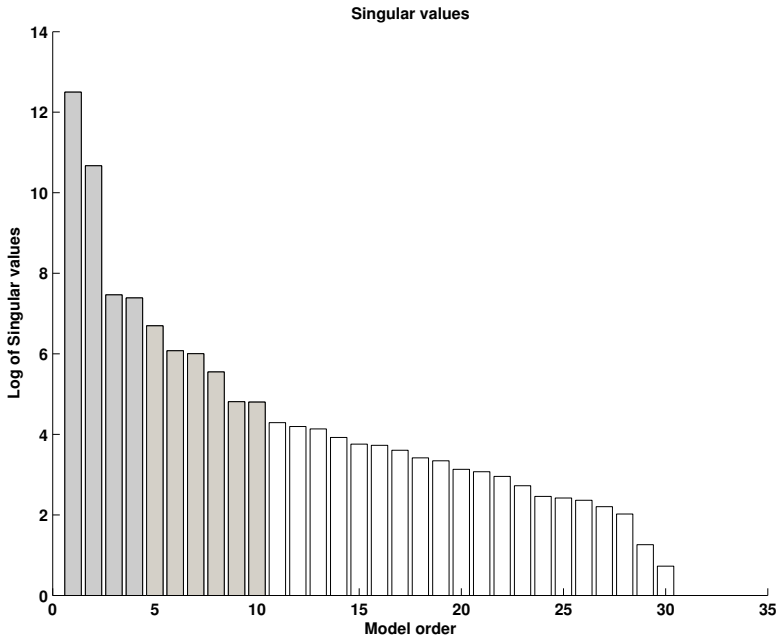

Figure 5.6: Singular values for the estimation of the model order

Moreover, in this approach the basic structure of the state space matrices of the resonant circuit model (eq.(4.29)) should be preserved. To do this the outputs are considered to equal the first two states. The structure of the output matrix C is therefore fixed and the model model has an order of three. For the integration of the input signals constraints on $\boldsymbol{A}$ and $\boldsymbol{B}$ are necessary that will be discussed in more detail.

The applicability of this approach is tested with a measured data set of type 2 (see Section 5.2.2) and a gradient of 14 MV/m. First the singular values of the measurement data matrices are inspected (see Figure 5.6). The most significant drop in magnitude of the

singular values can be seen for model order two such that a model order of three should be a sufficiently high order for the large signal behaviour model.

The model structure used in the following identification process is a state space model of order three with three inputs ($I_r(t)$, $I_i(t)$, $p(t)$) and two outputs ($V_r(t)$, $V_i(t)$). To emphasize the analogies to the resonant circuit model a continuous time state space model is used:

$$\begin{aligned} \boldsymbol{x}(t) &= \boldsymbol{A}_c\boldsymbol{x}(t) + \boldsymbol{B}_c\boldsymbol{u}(t)\,, \\ \boldsymbol{y}(t) &= \boldsymbol{C}_c\boldsymbol{x}(t) + \boldsymbol{D}_c\boldsymbol{u}(t)\,. \end{aligned}$$

with

$$\boldsymbol{y}(t) = \begin{pmatrix} V_r(t) \\ V_i(t) \end{pmatrix}\,,\ \boldsymbol{u}(t) = \begin{pmatrix} I_r(t) \\ I_i(t) \\ p(t) \end{pmatrix}\,.$$

The matrix structures with respect to the discussed constraints have the following form:

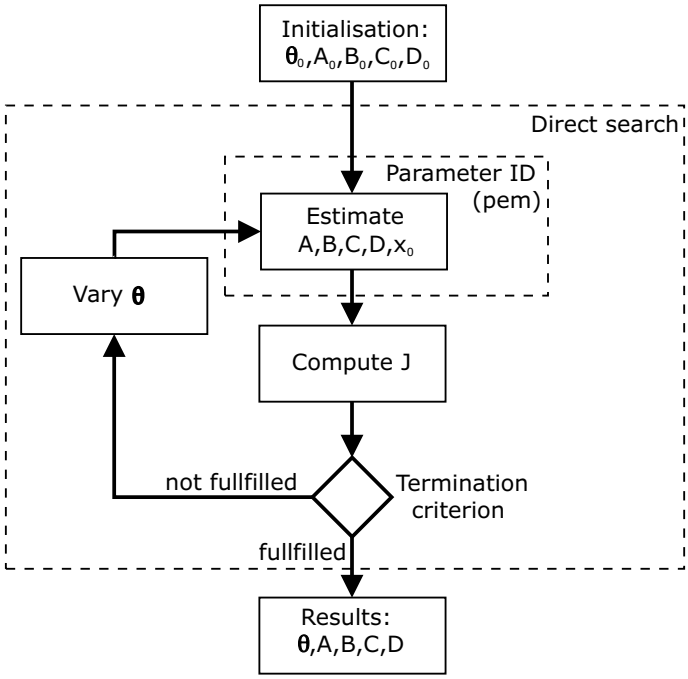

Figure 5.7: Flow diagram of parameter search for grey box modelling

$$\boldsymbol{A}_c = \begin{pmatrix} \star & \star & \star \\ \star & \star & \star \\ 0 & 0 & 0 \end{pmatrix}\,,\ \boldsymbol{B}_c = \begin{pmatrix} \star & \star & 0 \\ \star & \star & 0 \\ 0 & 0 & 1 \end{pmatrix}\,,\ \boldsymbol{C}_c = \begin{pmatrix} 1 & 0 & 0 \\ 0 & 1 & 0 \end{pmatrix}\,,\ \boldsymbol{D}_c = \begin{pmatrix} \star & \star & \star \\ \star & \star & \star \end{pmatrix}\,.$$

The $\star$ sign denotes that this matrix element is freely parametrizable in the parameter identification process. The integration of the third input resulting from this structure can be seen if the equation for the third state is isolated as

$$\dot{x}_3 = u_3 \tag{5.2}$$

because u_3 is a piecewise constant signal. The gain in eq.(5.2) is fixed to 1 in the input matrix $\boldsymbol{B}$. The influence of x_3 on the outputs is thus determined only by the elements in the third column of the system matrix $\boldsymbol{A}$.

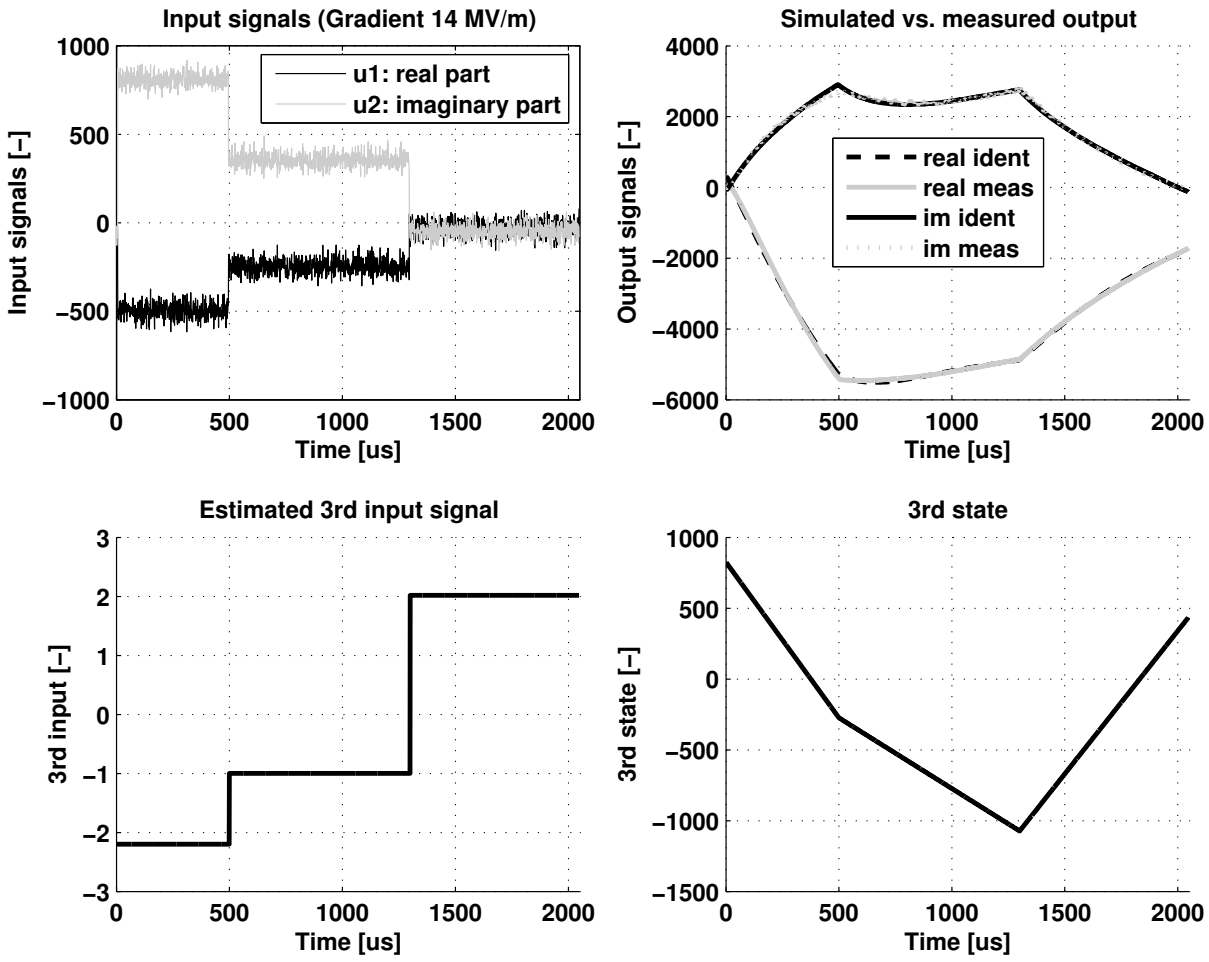

Figure 5.8: Results for constrained model (gradient 14MV/m, residual error functional $J = 1.3725 \cdot 10^7$)

MATLAB offers for the parameter estimation of constrained LTI models or gray box models the commands `pem` and `idgrey`. A detailed description of the embedded algorithms can be found in [14] and [24]. The initial states in our case are estimated by the same parameter estimation algorithm used to identify the state space model matrices. The complete algorithm for the minimization of the error functional $J(e, \boldsymbol{R})$ has the structure shown in Figure 5.7. The termination tolerance of the algorithm is specified as a minimum change in $J(e, \boldsymbol{R})$ during an iteration of $\epsilon = 0.01$. Dealing with output signals in the range of 10^3 in magnitude this tolerance should be sufficient without stretching calculation time (approximately 2 minutes) too extensively. The parameter estimation algorithm main steps can be summarized as follows:

1. Initial values for the unconstrained elements of $\boldsymbol{A}_c$, $\boldsymbol{B}_c$ and $\boldsymbol{\theta}_0 = \begin{pmatrix} \theta_{1,0} & \theta_{2,0} & \theta_{3,0} \end{pmatrix}^T$

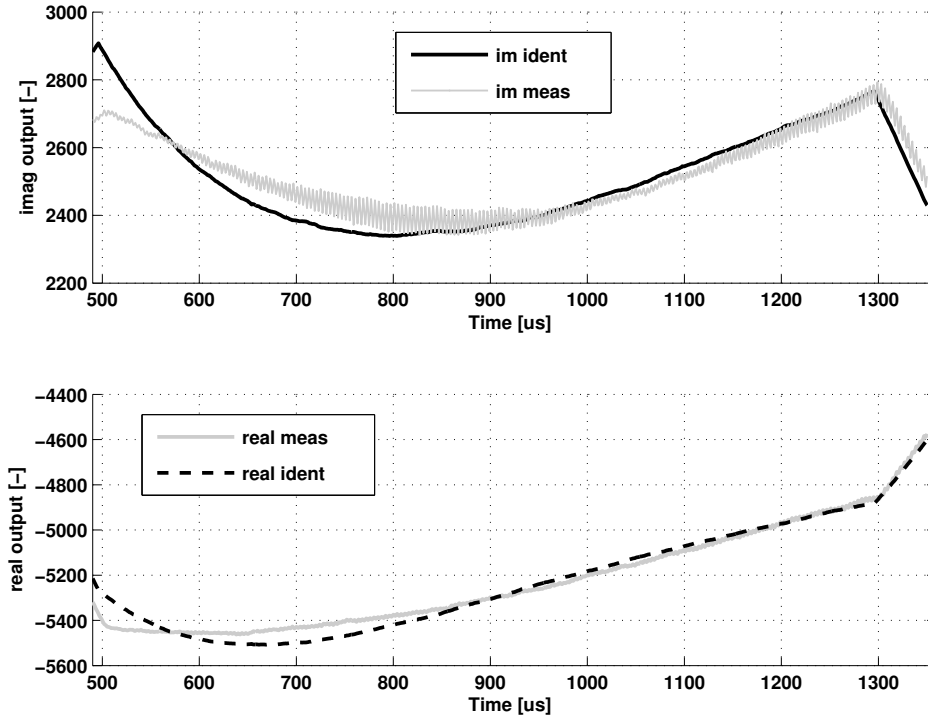

Figure 5.9: Zoom on the vector sum output signals of figure B.4

are set manually[2].

2. Vary $\boldsymbol{\theta}$ by means of a direct search based parameter estimation method (`fminsearch` in *MATLAB*).

3. Estimate state space matrix parameters for each $\boldsymbol{\theta}$ using an iterative prediction error method (`pem`) for the parametrization of LTI model structures.

4. Calculate $J = \sum_k \boldsymbol{e}^T \boldsymbol{R} \boldsymbol{e}$ with $\boldsymbol{R} = \boldsymbol{I}^{2\times 2}$ for the time interval of the RF-pulse.

5. Iterate steps 2-4 until the termination condition $|J_n - J_{n-1}| < \epsilon$ is fullfilled. The termination condition is specified for the direct search based parameter estimation method (n is the iteration index). Here, $\epsilon = 0.01$ has been chosen as a sufficiently tight tolerance resulting in moderate calculation time.

The results are shown in Figure 5.8 and Figure 5.9. The real and imaginary part of the vector sum are approximated acceptably well by the simulated outputs in a large signal sense. The deviations between simulation and measurements are less destinctive in the real part than in the imaginary part. With an equal weighting $\boldsymbol{R} = \boldsymbol{I}^{(2\times 2)}$ of errors in real and imaginary part the residual error functional value is $J = 1.373 \cdot 10^7$. The third state's trajectory looks even numerically reasonable compared with detuning curves described in

[2]The use of genetic algorithms for initial state estimation did not improve the results fairly and here only a general test of the model structure is focussed.

[20] for single cavities but nevertheless should not be interpreted as physically meaningful detuning.

The estimated system matrices are not normed with respect to physical units. They are estimated based on unitfree signals of the DSP system as:

$$\boldsymbol{A}_c = \begin{pmatrix} -0.002131 & -0.004396 & -0.005725 \\ -0.002163 & -0.005215 & -0.00706 \\ 0 & 0 & 0 \end{pmatrix}, \tag{5.3}$$

$$\boldsymbol{B}_c = \begin{pmatrix} -0.001718 & -0.01117 & 0 \\ 0.0002524 & 0.02001 & 0 \\ 0 & 0 & 1 \end{pmatrix}, \tag{5.4}$$

$$\boldsymbol{C}_c = \begin{pmatrix} 1 & 0 & 0 \\ 0 & 1 & 0 \end{pmatrix}, \tag{5.5}$$

$$\boldsymbol{D}_c = \begin{pmatrix} 0 & 0 & 0 \\ 0 & 0 & 0 \end{pmatrix}. \tag{5.6}$$

The eigenvalues of $\boldsymbol{A}_c$ are

$$\boldsymbol{\lambda}_c = \begin{pmatrix} -0.0018 \\ -0.0055 \\ 0 \end{pmatrix}, \tag{5.7}$$

which means the model is at the stability limit (see [15]). The eigenvalue at zero of course has been part of the constraints and resembles the integration of the input but the two other eigenvalues are close to the stability limit, too. This however makes sense for the weakly damped resonator system. The estimated state space model does not have any zeros which seems to be mainly numerically related to the lack of preprocessing (e.g. removal of mean values, filtering etc.). To improve the accuracy of the large signal model in the following sections the structural constraints are removed and black box model structures will be parametrized.

5.3.2 Models for filling, flat top and decay

In the next step, models for the field trajectories during the phases filling, flat top and decay of the pulse structure are identified seperately. The purpose is that the eigenvalues of the model's system matrices should be compared. By doing this it will be clarified if the system behaviour in one of the phases significantly differs from the other phases. Then it can be decided whether individual models for each phase are necessary or if one model is possibly sufficiently accurate for the large signal behaviour of TTF2.

Unlike in the previously described gray box identification process now black box models are used. Moreover, not only one data set is used for modelling but three data sets[3] (two

[3]Of course the usage of signal type 1, which is white noise with a certain mean value does not make any sense for this partwise identification because in the output data only a filling trajectory can be seen.

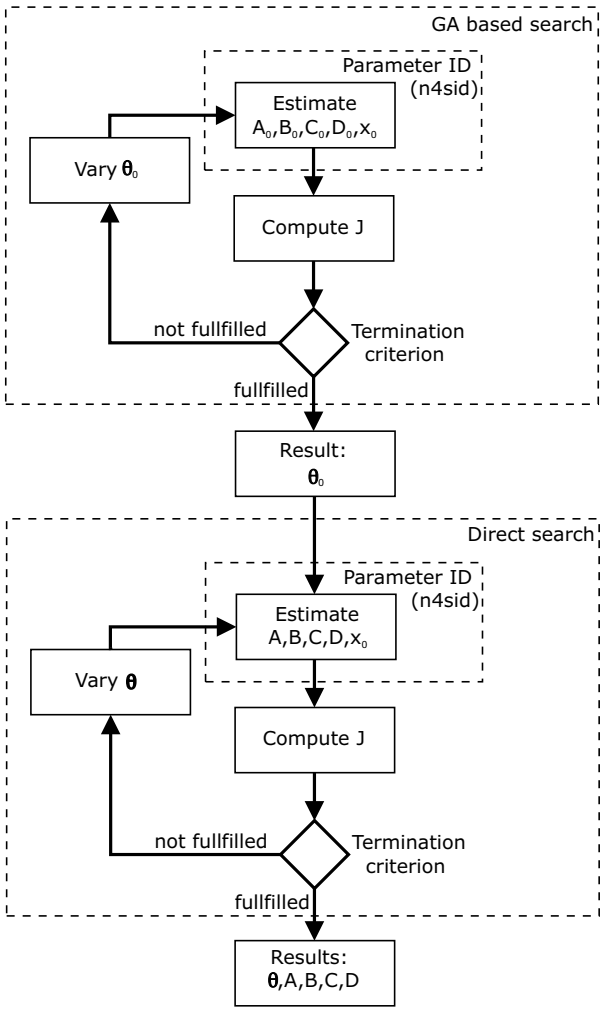

Figure 5.10: Parameter search flow diagram for black box modelling

of signal type 2 and one of signal type 3). The model order again has been specified by an inspection of the singular values and again a model order of three has been chosen. The models are discrete time state space models. The reason is that the controller structure that will be designed on the basis of the models is a discrete time structure as well.

Now the third input signal is considered to be the parameter disturbance itself such that its trajectory consists of three linear parts. This curve is characterized by four parameters: An initial value and a slope for each time interval (see section 4.2). However, because each part is identified separately the third input for each part is only given by one line characterized by an initial value and a slope, i.e. $\boldsymbol{\theta} \in \mathbb{R}^{2\times 1}$. No continuity condition for the parts of the third input between the three time intervals has been given because the focus for this models is the behaviour during the individual phases.

In this approach genetic algorithms (GA) are used for the estimation of the initial values of $\boldsymbol{\theta}$. Then the direct search method via the MATLAB command `fminsearch` is used to find the minimum in the region of the initial value. The complete parameter estimation

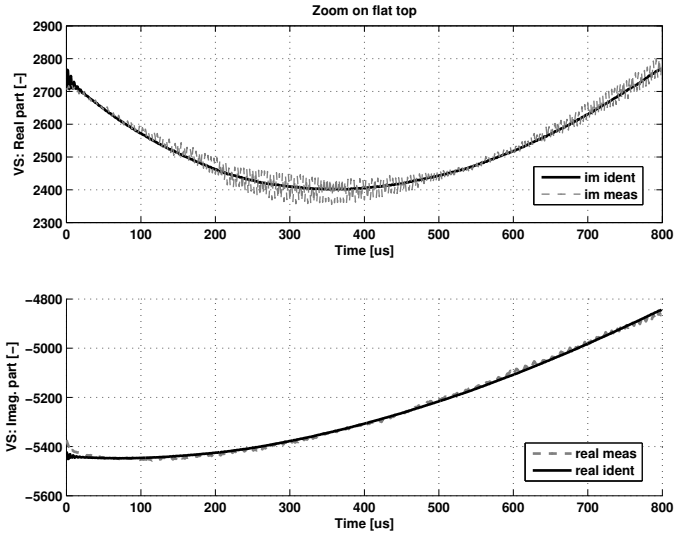

Figure 5.11: Zoom on flat top for partwise identified model

algorithm used for the partwise identification is given by:

1. Use GA to estimate the initial parameter vector $\boldsymbol{\theta_0}$ by minimizing the error functional $J(e, \boldsymbol{R})$. In each iteration the state space matrix elements are estimated by subspace methods (`n4sid`) for the current $\boldsymbol{\theta}$.

2. The termination values of the GA based search are used as initial values $\boldsymbol{\theta_0}$ in the direct search methods. The cost function is the same as the one for the GA based minimization. Initial values for the states are in both cases estimated by the subspace identification algorithm.

3. Iterate 2. until $|J_n - J_{n-1}| < \epsilon$ holds where the tolerance for the termination croterion to be fullfilled has again been chosen as $\epsilon = 0.01$.

Figure B.4 shows an exemplary comparison between model output and measurement data. It can be seen that very accurate fitting is achieved with a third order model for each phase. When the end value of the parameter disturbance trajectory of one phase is compared with the initial trajectory value of the next phase significant discontinuities can be seen but this is obvious because of the lack of constraints. A zoom on the real and imaginary parts of the field vectors during the flat top interval is shown in Figure 5.11. Here the curves of measurement and simulation data can be distinguished. In the unfiltered measurement data the corruption by high frequent noise in the range of 250 kHz can be seen. This behaviour is of course not visible in the output of the low order model. Inspecting the modelling error in frequency domain revealed the dominating 250 kHz noise component.

The eigenvalue distribution of the inferred models for three different data sets are shown in Figure 5.12. All models are stable and do not contain transmission zeros. While the models of the filling phase only have real eigenvalues, the eigenvalues of the flat top and

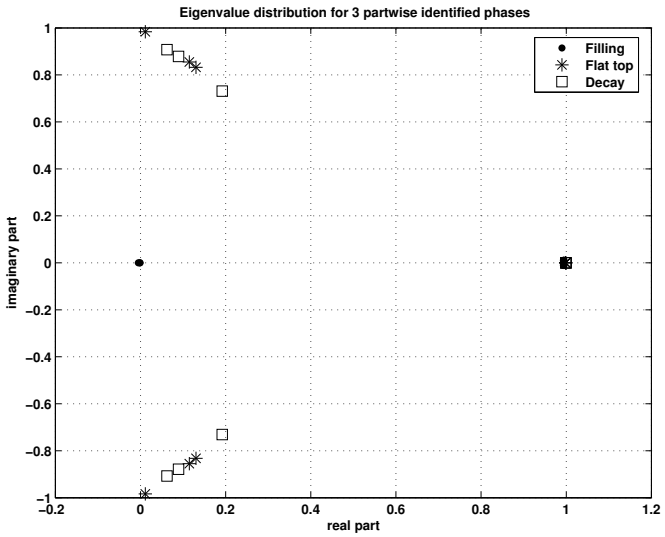

Figure 5.12: Eigenvalue distribution of partwise identified models

decay models are complex and very similar in their distribution. It can also be seen that the spread in eigenvalues of different data sets even with different gradients is moderate. This leads to the assumption that the whole trajectory of the field envelopes can be described sufficiently accurate by one third order black box model. This approach is discussed in the next section.

Higher order model structures have been tested as well for the partwise identification without improving the results significantly, the calculation time has however increased by several factors compared to a model structure of order three.

5.3.3 Third order large signal model

The idea is to find a large signal model of order three which describes all three phases of the vector sum (filling, flat top and decay). The model should describe the plant behaviour sufficiently well for a field gradient of 14 MV/m and should be validated for a field gradient of 13 MV/m. This state space model is a discrete time model as well with a black box model structure. The parameter disturbance is again directly resembled in the third input. Because the model should describe the plant behaviour in a large signal sense, the shape of the parameter disturbance input $p(t)$ is a continuous partwise linear trajectory.

For the parameter estimation the same algorithm as used for the partwise identification with parameter disturbance input is used (see Figure 5.10). In the validation process it should be clarified how well the model maps input data with a different level on the measurement outputs of the vector sum. The validation is done using two different ways: First the state space model matrices and $p(t)$ are fixed and the validation data is entered into the model. Secondly, only the state space matrices obtained for the data set used for identification is

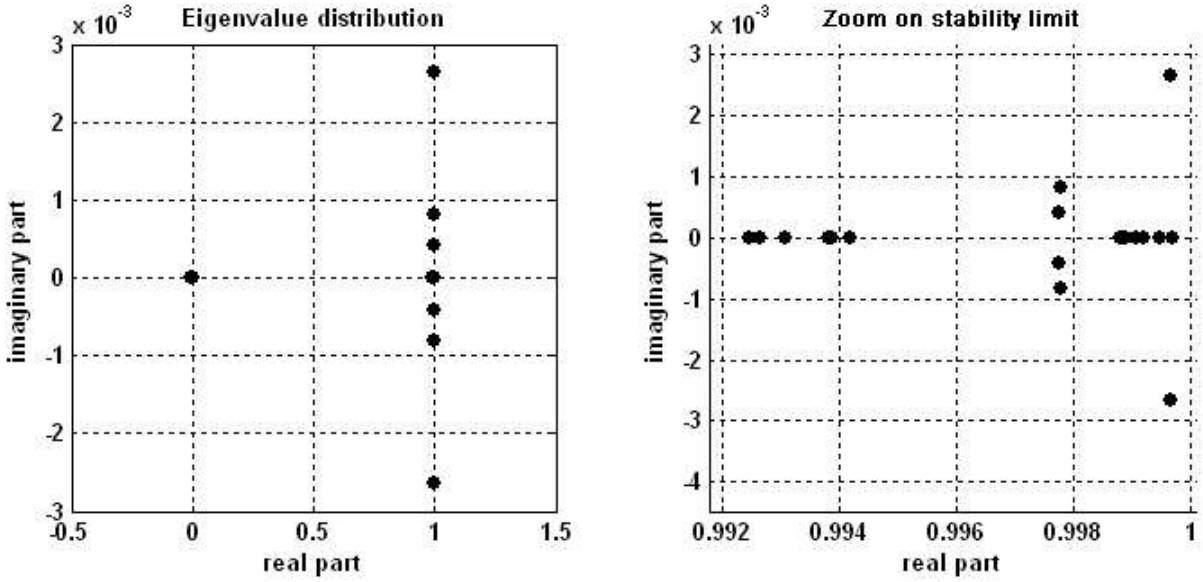

Figure 5.13: Eigenvalue distribution of 3rd order large signal models

fixed and for the validation data a new disturbance input signal is estimated. By comparing the results it can be seen how accurate the state space model itself can handle validation data and to which extend a newly estimated disturbance input improves the validation performance. From a physical point of view, the parameter disturbance depends in a way on the cavity detuning which is gradient dependend. It is therefore assumed that the newly estimated $p(t)$ for a different gradient has a gradient dependent level.

To obtain the model the following strategy is used:

- Parametrize the model structure and $p(t)$ for data (ID data) recorded for different field gradients (13 MV/m, 14 MV/m and 15.6 MV/m) by using the parameter estimation algorithm shown in Figure 5.10.
- 1. validation step: Validate all models with a data set that has not been used for the parameter estimation. Here, data recorded at a field gradient of 13 MV/m is used for validation. In the first step the same $p(t)$ is used as the one estimated for the model on basis of the original ID data.
- 2. validation step: Validate all models again with the validation data set of gradient 13 MV/m but estimate a new $p(t)$ for the validation data while the state space matrices are fixed. Thus, the information about the I/O behaviour contained in the parameter disturbance signal can be isolated.
- Benchmark the models by taking the residual error functionals $J(e, \boldsymbol{R})$ for the original ID data and both validation procedures into account.

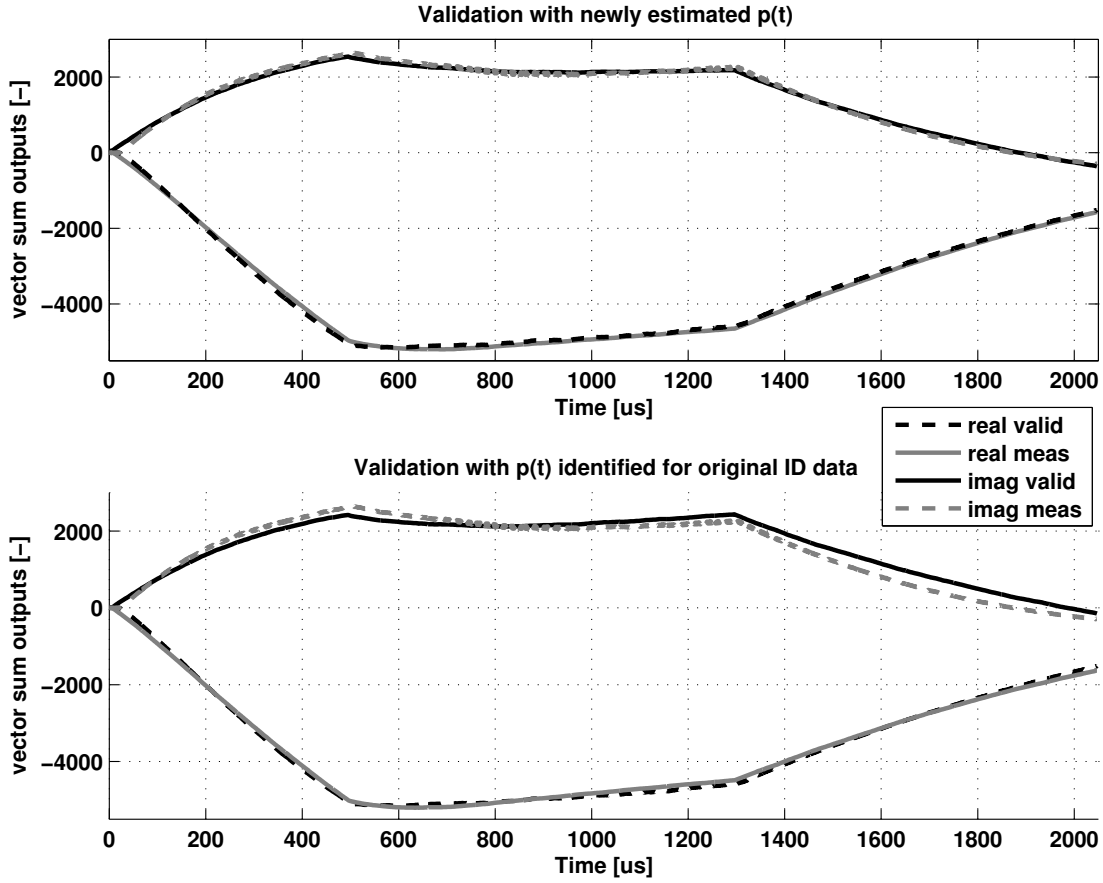

Figure 5.14: Comparison of validations for model $GLDB3_x2_u2_y1_d$ with newly estimated input $p(t)$ and same $p(t)$ obtained by parameter estimation of state space matrices

Discussion of results

The resulting residual error functional values for this procedure are presented in table 5.2. When inspecting the error functional values some interesting results can be seen. Of course, the value of J in the validation procedure is lower if another $p(t)$ is estimated but the residual values significantly differ even for models obtained for the same gradient. This can be seen comparing the values of $J(e, \boldsymbol{R})$ with a newly estimated $p(t)$ in validation of models 5 and 6. The lower the field gradient of the model becomes the lower becomes the values of $J(e, \boldsymbol{R})$ for obtained for validation, which is obvious because validation data of the lowest used gradient (13 MV/m) is used. The eigenvalue distribution of the obtained models for eight different data sets is presented in Figure 5.13. It can be seen that the eigenvalues are distributed in two narrow intervals: The models posess real eigenvalue close to zero and either two real or two complex conjugated eigenvalues with a small imaginary part and a real part close to one. However all models are stable and do not have any transmission zeros. Physically, no transmission zeros have to be claimed for the resonator structure and the reason for the lack of transmission zeros seems to be that the data has not been preprocessed e.g. by filtering or removal of trends, which frequently leads to

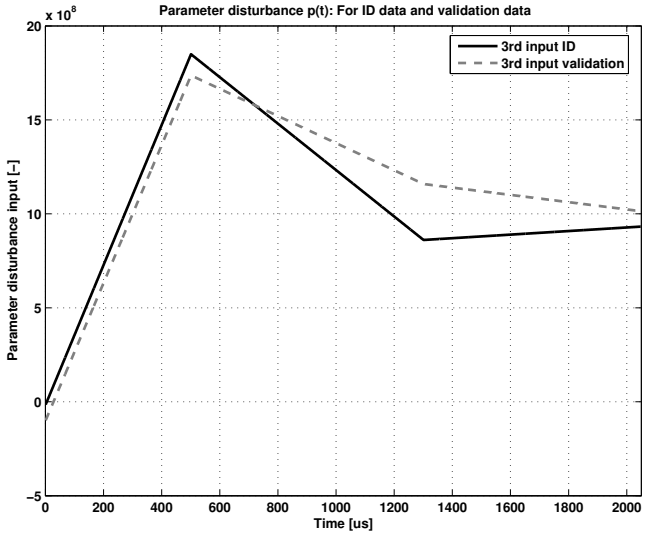

Figure 5.15: Parameter disturbance input $p(t)$ for estimated for ID data and validation data (with same state space matrices)

transmission zeros of the identified model.

The model performance of model 8 for the original ID data is shown in Figures B.2 and B.3 (zoom on flat top). It can be stated that this model describes the large signal behaviour for this data set very well which is emphasized by the lowest value of the error functional for ID data ($J(e, \boldsymbol{R}) = 1.0105 \cdot 10^7$). The validation performance is shown in Figure 5.14. With a newly estimated parameter disturbance input the measured output data of a different field gradient is reproduced acceptably as well while the model performance with the same $p(t)$ as for the ID data becomes visible worse. The signals $p(t)$ for this model are shown in Figure 5.15. Here it can be seen that the basic shape of the signals is similar but that the newly estimated parameter disturbance for the validation data has a lower maximal value. To correlate this with the lower field gradient would make sense but cannot be proven rigorously because of the missing physical interpretability of the values of $p(t)$. The frequency response of the model is shown in figure B.6. The matrices of the discrete time state space model number 8 are:

Table 5.2: Residual error functional values for estimated third order large signal models with parameter disturbance input

Model No.	J **(ID data)**	J **(validation, old** $p(t)$**)**	J **(validation new** $p(t)$**)**
1	$1.1422 \cdot 10^7$	$8.8667 \cdot 10^9$	$3.5612 \cdot 10^8$
2	$1.1525 \cdot 10^7$	$8.5349 \cdot 10^9$	$7.5375 \cdot 10^8$
3	$1.1239 \cdot 10^7$	$6.3027 \cdot 10^7$	$2.5505 \cdot 10^7$
4	$1.0976 \cdot 10^7$	$7.3411 \cdot 10^7$	$1.5509 \cdot 10^7$
5	$1.0997 \cdot 10^7$	$7.8009 \cdot 10^7$	$1.668 \cdot 10^7$
6	$1.0900 \cdot 10^7$	$4.6912 \cdot 10^7$	$3.7562 \cdot 10^7$
7	$1.032 \cdot 10^7$	$5.8842 \cdot 10^7$	$3.2905 \cdot 10^7$
8	$1.0105 \cdot 10^7$	$9.8532 \cdot 10^7$	$1.8547 \cdot 10^7$
9	$1.0776 \cdot 10^7$	$1.1188 \cdot 10^7$	$1.1749 \cdot 10^7$
10	$3.0691 \cdot 10^7$	$4.5856 \cdot 10^7$	$3.4932 \cdot 10^7$

Discrete state space model GLDB3$_\mathbf{x}$2$_\mathbf{u}$2$_\mathbf{y}$1$_\mathbf{d}$

$$\boldsymbol{A} = \begin{pmatrix} 0.998700 & -0.001107 & -0.001634 \\ -0.000692 & 0.9924 & 0.07687 \\ -0.003129 & 0.02193 & 0.001143 \end{pmatrix}, \tag{5.8}$$

$$\boldsymbol{B} = \begin{pmatrix} 4.978 \cdot 10^{-7} & -2.492 \cdot 10^{-7} & 7.811 \cdot 10^{-12} \\ -1.911 \cdot 10^{-5} & -1.487 \cdot 10^{-6} & -3.945 \cdot 10^{-10} \\ 0.0002475 & 2.901 \cdot 10^{-5} & 5.089 \cdot 10^{-9} \end{pmatrix}, \tag{5.9}$$

$$\boldsymbol{C} = \begin{pmatrix} 3.364 \cdot 10^4 & 1709 & 33.94 \\ -2.499 \cdot 10^4 & 7859 & 546.5 \end{pmatrix}, \tag{5.10}$$

$$\boldsymbol{D} = \begin{pmatrix} 0 & 0 & 0 \\ 0 & 0 & 0 \end{pmatrix} \tag{5.11}$$

Sampling time: $T = 1 \cdot 10^{-6} s$

The model has the following real eigenvalues λ_i

$$\boldsymbol{\lambda} = \begin{pmatrix} -0.00055 \\ 0.9989 \\ 0.9939 \end{pmatrix}.$$

This model will be benchmarked against an output error MIMO model without disturbance input that is presented in the next section. According to table B.1 the abbreviating term $GLDB3_x2_u2_y1_d$ is used for the large signal I/O behaviour model with parameter disturbance input.

Comparison of the model GLDB3$_\mathbf{x}$2$_\mathbf{u}$2$_\mathbf{y}$1$_\mathbf{d}$ with the resonant circuit model

Table 5.3: Large signal I/O behaviour model benchmark

Model	J **for ID data**
Parametrized resonant circuit model with ODE for detuning	$1.14332 \cdot 10^8$
$GLDB3_x2_u2_y1_d$	$1.1855 \cdot 10^7$

The developed large signal model with the parameter disturbance input ($GLDB3_x2_u2_y1_d$) describes the RF-field behaviour during the RF-pulse more accurately than the resonant circuit model with the obtained parametrization. The lowest error functional values of the parametrized resonant circuit model and the model with the estimated disturbance input can be directly compared because the models describe the RF-pulse and the decay phase (see table 5.3).

The difference is more than one degree in magnitude. The results are shown only for the simulation results with ID data because the resonant circuit model's validation data performance is certainly poorer than its ID data performance. Moreover, the error functional values for validation of the model $GLDB3_x2_u2_y1_d$ are lower than the resonant circuit models error functional values for simulations with ID data. The good performance is caused by the parameter disturbance input which has been motivated by the time varying detuning parameter in the resonant circuit. However even if the same parameter disturbance input that has been estimated for ID data is used for validation with a different gradient, the model performance of model $GLDB3_x2_u2_y1_d$ is better than the resonants circuit model performance.

5.4 Output Disturbance model

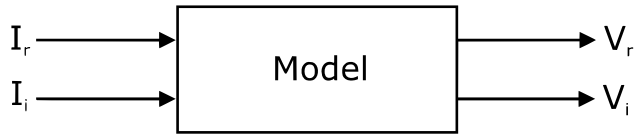

Figure 5.16: Two input two output model of TTF2

The next approach to model TTF2 does not take the structure of the resonant circuit model into account for any kind of constraints. TTF2 is modelled using a multivariable black box model structure with two inputs and two outputs (see Figure 5.16). Disturbances are considered as output disturbances entering the output channels V_r and V_i. Here the more classical way of parameter estimation in system identification is used and applied with MATLABs *System Identification Toolbox*:

1. First the data is preprocessed, which involves the selection of the time interval of the data, prefiltering, removal of means or linear trends etc. and will be further explained for the large and small signal behaviour models.

2. The next step is the choice of the parameter estimation method. Here only discrete time state space models are estimated via subspace methods (`n4sid` command in MATLAB)

3. Model validation can directly be done after the model parameters are estimated using the toolbox.

An accurate low order large signal model has already been presented in the previous section (model $GLDB3_x2_u2_y1_d$) but an additional large signal model obtained with this approach will be presented as well. The performance of the large signal models will be compared. Benchmarking the models int this context is done using residual error functional values.

The main focus however with this MIMO model approach lies on models for the small signal behaviour of the plant during the flat top phase. An accurate small signal model is presented in Section 5.4.2.

5.4.1 Large signal I/O behaviour MIMO model

To compare the two different modelling approaches using a parameter disturbance input vs. using purely output errors a large signal behaviour MIMO model without disturbance input has been estimated. The model should describe the two phases filling and flat top, i.e. the system behaviour during the RF pulse. Because control action takes part during the filling and flat top phase anyway the omission of the decay phase for parameter estimation of the large signal model is reasonable if the RF-pulse time interval is thus described more accurately. However, the third order model $GLDB3_x2_u2_y1_d$ is able to describe all three phases accurately.

The following large signal I/O behaviour model deduced in the subsection will be abbreviated by $GLDB9_x2_u2_y$. It should be denoted that all output disturbance models presented in this chapter have been obtained in an iterative way by varying data preprocessing methods etc.. Here only the best obtained models for large and small signal plant behaviour are presented. The models are identified for a field gradient in the cavities of 14 MV/m and are validated by using data recorded for a field gradient of 13 MV/m.

Preprocessing

The model $GLDB9_x2_u2_y$ is developed on the basis of preprocessed measurement data. The preprocessing steps are:

- Omitting the decay phase (as discussed) by limiting the data time interval on the beginning of the RF-pulse to the end of the flat top. The first 6 samples before the start of the RF-pulse are omitted as well, such that only the samples 6 to 1296 from originally 1 to 2048 are considered for the parameter estimation of the model.

- The measurement data of the output signals is corrupted by a main noise component at 250 kHz caused by electronic components. This has been discussed in chapter 5.2.3. Therefore the measurement I/O data has been filtered by a lowpass filter with a cutoff frequency of 100 kHz. For the large signal model performance the focus on the frequency range up to this cutoff frequency will definitely be sufficient.

Estimating the state space matrices

Before the parameter estimation process a model structure needs to be chosen as described in Chapter 3.3. Discrete time state space models are chosen for the applicability of the subspace method `n4sid` implemented in *MATLAB* and the model order is again chosen by inspection of the singular values of the measurement data Hankel matrix. The singular values can be visualized for different model orders by the *MATLAB System Identification Toolbox* and have exemplarily already been shown in Figure 5.6.

The parametrization of the state space model structure is done using subspace methods (`n4sid`). The initial states are estimated by the algorithm as well. The general form of a discrete time state space model structure in the *System Identification Toolbox is*

$$\boldsymbol{x}(k+1) = \boldsymbol{A}\boldsymbol{x}(k) + \boldsymbol{B}\boldsymbol{u}(k) + \boldsymbol{K}\boldsymbol{e}(k) \tag{5.12}$$

$$\boldsymbol{y}(k) = \boldsymbol{C}\boldsymbol{x}(k) + \boldsymbol{D}\boldsymbol{u}(k) + \boldsymbol{e}(k)\,. \tag{5.13}$$

The matrix $\boldsymbol{K}$ can incorporate properties of the disturbance and how it couples on the states but we will enforce $\boldsymbol{K} = \boldsymbol{0}$ such that the state space model has an output error structure.

Various model orders have been tested according to the singular value distribution in figure 5.6. The resulting models have been benchmarked by means of the residual value of the squared error functional J between model output and measurement data. For the benchmark this error functional is computed for different data sets:

- The data used for the identification of the model (in the following called ID data).

- For validation input data. Validation data is data that has not been used for the identification of the model and ideally has different properties (e.g. amplitude and bandwidth) than the ID data. In this case measurement data for signal type 3 (bandlimited white noise superimposed on the feedforward signal) as input with a gradient of 13 MV/m is used for validation. See chapter 5.2.2 for more details on the signal types used for the system identification of TTF2.

Table 5.4: Residual error functional values for estimated models of different order

Model order	J **for ID data**	J **for validation data**
6	$5.3024 \cdot 10^7$	$4.7873 \cdot 10^7$
7	$5.527 \cdot 10^7$	$4.8307 \cdot 10^7$
8	$4.5337 \cdot 10^7$	$4.2323 \cdot 10^7$
9	$4.3846 \cdot 10^7$	$4.1362 \cdot 10^7$
10	$4.416 \cdot 10^7$	$4.4325 \cdot 10^7$

The residual error functional values for different model orders are presented in table 5.4. The state space model of order 9 has the lowest error functional values for both the ID data and the validation data and will be further investigated. It will be abbreviated $GLDB9_x2_u2_y$ according to table B.1. Remarkable is the fact that the error functional values for the validation data are lower than for the ID data. This is normally not the case but an explanation could be that the validation data set is less corrupted by disturbances. Physically, the Lorentz force detuning of the cavities is gradient dependent, i.e. the disturbance due to detuning has less influence on the validation data with a gradient of 1MV/m less than the ID data's gradient. The validation has been carried out with data of gradient 15.6 MV/m as well and for all models higher residual error functionals have been obtained which would support the assumption. The frequency response of the model is presented in Figure B.7.

The comparison between model outputs of $GLDB9_x2_u2_y$ and measurement data for simulations with ID data and validation data are shown in Figures 5.17 and 5.18. It can be seen that the real part of the measured vector sum is approximated better than the imaginary part. This is also the case with model $GLDB3_x2_u2_y1_d$. The reason could be measurement hardware (so called I-Q-detectors).

The eigenvalues λ_i and transmission zeros of the model $GLDB9_x2_u2_y$ are displayed in Figure 5.19. Their numerical values of the eigenvalues are

$$\boldsymbol{\lambda} = \begin{pmatrix} 0.3593 \\ 0.7359 \pm i0.6098 \\ 0.8562 \pm i0.449 \\ 0.9985 \\ 0.9771 \\ 0.8079 \\ 0.8533 \end{pmatrix}, \quad \begin{pmatrix} |\lambda_{2,3}| \\ |\lambda_{4,5}| \end{pmatrix} = \begin{pmatrix} 0.9557 \\ 0.9668 \end{pmatrix}.$$

The model is stable because $|\lambda_i| < 1, i = 1, \ldots, 9$ holds but it is non-minimum phase because of five transmission zeros with a magnitude larger than one. This must be considered when applying high gains in feedback because the closed-loop system can become unstable (see [15] for more details).

Comparing the model performance of $\mathbf{GLDB9_x2_u2_y}$ and $\mathbf{GLDB3_x2_u2_y1_d}$

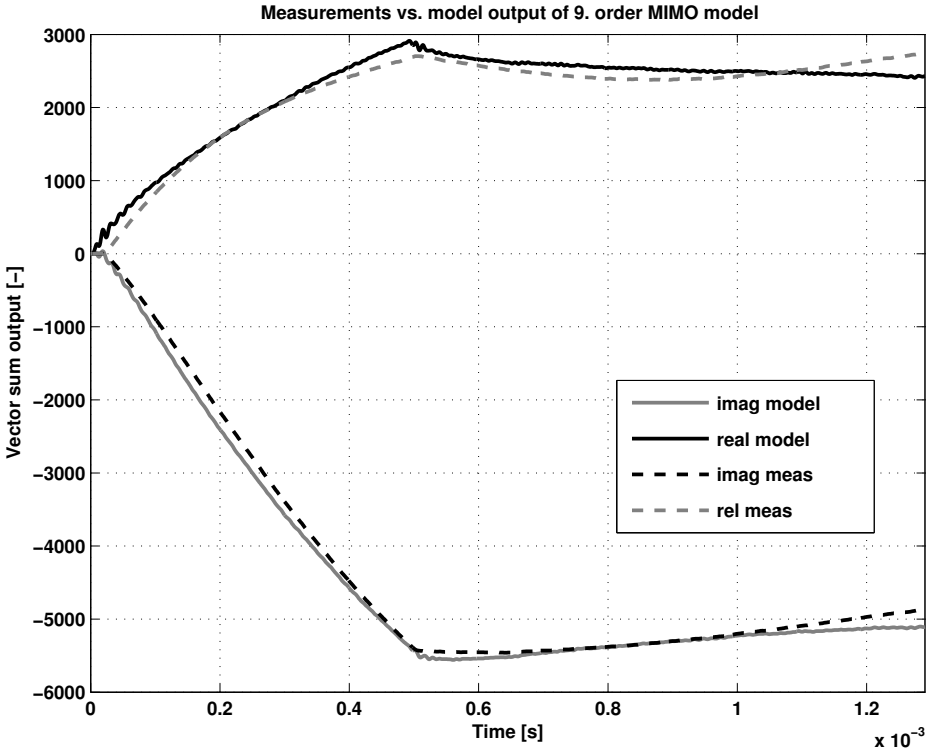

Figure 5.17: Output of model $GLDB9_x2_u2_y$ for ID data

Table 5.5: Large signal I/O behaviour model benchmark

Model	J **for ID data**	J **for validation data**
$GLDB9_x2_u2_y$	$4.3846 \cdot 10^7$	$4.1362 \cdot 10^7$
$GLDB3_x2_u2_y1_d$	$1.1855 \cdot 10^7$	$1.1855 \cdot 10^7$ (if $p(t)$ is newly estimated) $9.8532 \cdot 10^7$ (if $p(t)$ identified for ID data is used)

For the comparison it important to clarify that the error functional values $J(e, \boldsymbol{R})$ of model $GLDB3_x2_u2_y1_d$ contains the model deviations in the decay phase after the RF-pulse. The model $GLDB9_x2_u2_y$ has been developed only for the phase of the RF-pulse. The absolute values of the error functionals are thus not directly comparable. The comparison of the two best large signal I/O behaviour models obtained in this chapter yields that the third order model with the parameter disturbance input $GLDB3_x2_u2_y1_d$ predicts output data more accurately for ID data and validation data than the ninth order model $GLDB9_x2_u2_y$ (see table 5.5). The error functional values are lower for ID data simulation and validation with a newly estimated parameter disturbance input than the error functional values of model $GLDB9_x2_u2_y$ although the deviations in the decay phase are included in the error fuctional of $GLDB3_x2_u2_y1_d$. If the same $p(t)$ is used for the validation process as the $p(t)$ that has been estimated for the ID data the residual error functional value increases and the model performance becomes poorer.

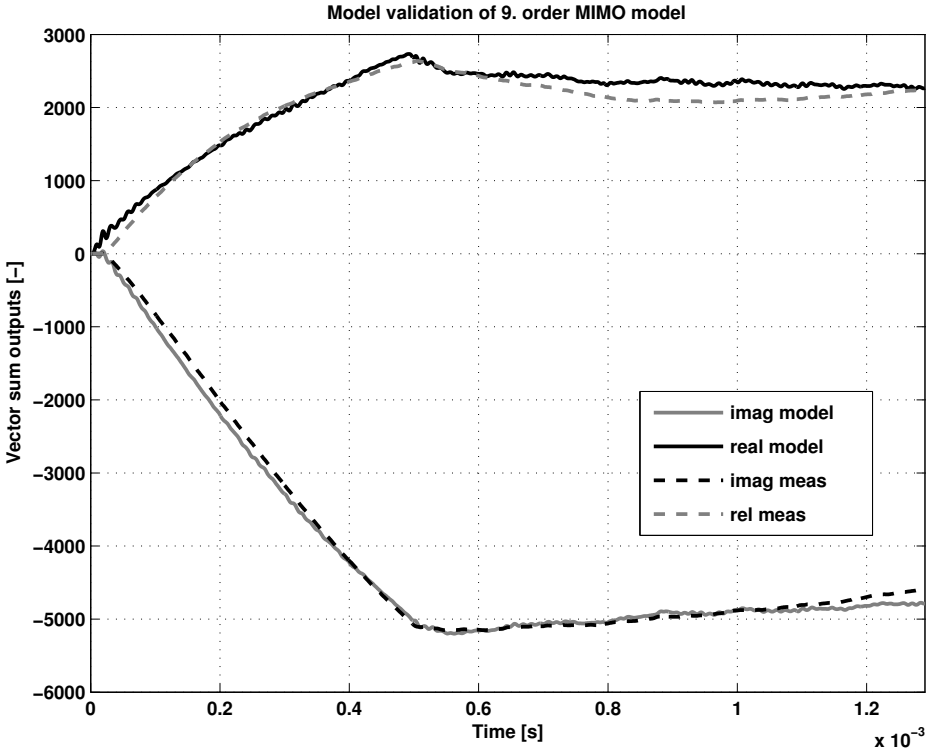

Figure 5.18: Output of model $GLDB9_x2_u2_y$ for validation data (Gradient 13 MV/m)

As it has been discussed in Section 5.3.3 the signal $p(t)$ depends on the gradient. Because for validation data a lower field gradient has been chosen the poorer model performance makes sense. For the practical application of the models for controller design it can be stated that the model $GLDB9_x2_u2_y$ is less sensitive to gradient variations because of its good validation performance. However, if online identification of the plant will be used in the future (see Chapter 7), the parameter disturbance $p(t)$ could be estimated online after an RF-pulse (the calculation takes less than a second) and the model $GLDB3_x2_u2_y1_d$ will be a more precise output data predictor.

5.4.2 Small signal behaviour MIMO model for the flat top

A very important issue for fulfilling the control objectives for the XFEL is a model for controller design that describes the small signal behaviour of the RF-fields during the flat top. The precise field stability during this phase is needed to achieve the required beam quality for the XFEL to operate. In this section a small signal behaviour model is developed using system identification techniques. Various diagrams that illustrate intermediate steps in the identification process are presented in appendix C.

Inferring a small signal model for the flat top phase has been an iterative procedure because of the various preprocessing steps necessary to obtain a representative data set for the small

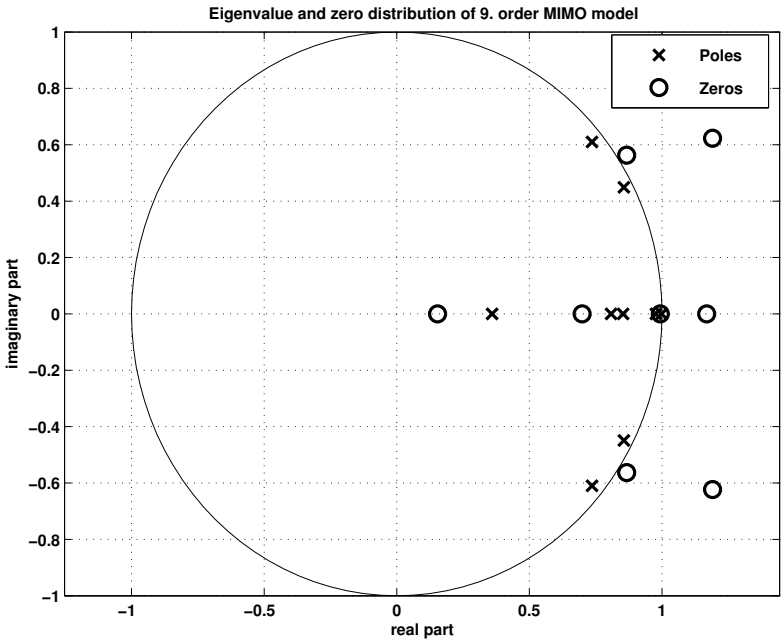

Figure 5.19: Eigenvalues and transmission zeros of 9th order large signal MIMO state space model $GLDB9_x2_u2_y$

signal behaviour of the plant. Representative in this context only means that the dynamical plant behaviour, that should be resembled in the model is included in the data set. Otherwise the state space matrices would include informations about the disturbance and an output error model structure would not be longer present. Of course, this preprocessing can not be realized ideally because in case of the linear accelerator system TTF2 the frequency ranges and levels of the various disturbances are not known precisely enough to remove their effects accurately from the measurement data. The *MATLAB System Identification Toolbox* has prooven to be a very useful tool in the identification process because it offers amongst other various preprocessing procedures for measurement data.

Here, a model for an operating point of 14 MV/m is presented that shows good validation performance for other recorded data with the same field gradient and for data that has been measured for a field gradient of 13 MV/m. The model is a discrete time state space model of sixth order with two inputs and two outputs and will be abbreviated $PLDB6_x2_u2_y$ according to table B.1. All disturbances are considered as output disturbances such that we deal again with an OE model structure. By the iterative procedure of preprocessing data the following steps have appeared to be succeeding:

1. First the range of the I/O data has been selected to pick only the flat top phase out. This phase last from sample 500 to sample 1300. Here, a range from 480 to 1296 (again in samples) has been selected. An interval of 20 samples before the flat top begins has been chosen because filtering will also be a preprocessing step that makes the response of the output signals slower. This delay can then be dealt with limiting the range again after filtering.

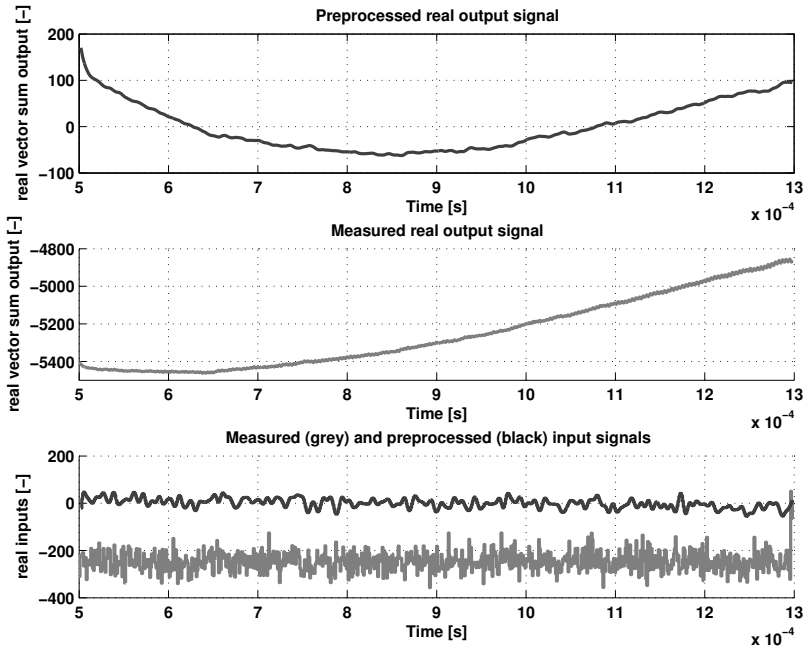

Figure 5.20: Comparison of raw and preprocessed real input and output data

2. Linear trends are removed from the data. Especially in the real part of the vector sum V_r a linear drift can be seen for all measurements that should not be incorporated in the model.

3. Lowpass filtering is applied using a corner frequency of $f_c = 100$kHz. The purpose is to remove high frequent noise from the data, in particular the 250kHz noise component caused by the local oscillators of the downconverter system.

4. Now the range of the data is adjusted again and the first 24 samples are cut off such that the flat top interval remains.

5. As a last step the mean value of the data is removed to be sure no offset is identified. An important point is that the removal of the mean is legitime because we deal with an LTI model structure suitable for a limited range of operating points. The linearity ensure that the output of the small signal model is superimposed the offset value set by the operating point.

The comparison of measurement data and the shape of this input and output signals after these preprocessing steps is shown in Figure 5.20 for the real input and output signals and in Figure 5.21 for the imaginary signals vice versa.

The parametrization of the model structure is done using again the subspace algorithm implemented in *MATLAB*, `n4sid`. First, the model order is selected by inspecting the singular values of the preprocessed datas Hankel matrix of the impulse response (see Figure 5.22). Because of the drop in magnitude for model for model order six first model order

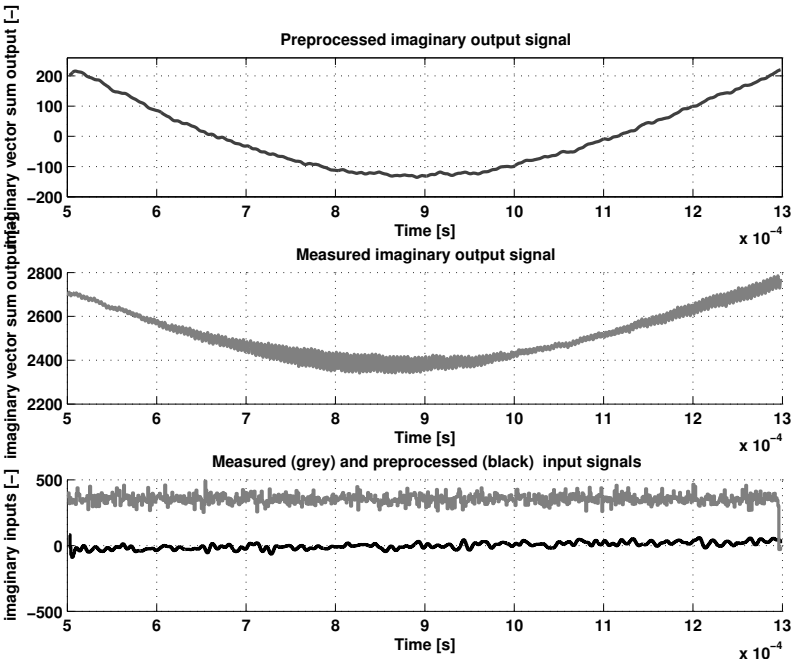

Figure 5.21: Comparison of raw and preprocessed imaginary input and output data

five has been choosen. Even by optical inspection of the model output compared to measurement data the bad model performance was evident because the concave shape of V_i could not be described at all by the model. As a result higher order model structures have been parametrized by `n4sid`. The appropriate model order to describe the small signal I/O behaviour of TTF2 seems to be order six and the resulting model is $PLDB6_x2_u2_y$.

The comparison of model output and measurement data of the data used for the identification of the model is shown in Figure 5.23. The performance so far can be considered adequate but the model must be validated to proove its ability to describe the plant I/O behaviour for other than the ID data. The model has the following eigenvalues λ_i and transmission zeros κ_i

$$\boldsymbol{\lambda} = \begin{pmatrix} 0.8943 \pm i0.4278 \\ 0.8853 \\ 0.9984 \\ 0.9833 \pm i0.1403 \end{pmatrix}, \quad \begin{pmatrix} |\lambda_{1,2}| \\ |\lambda_{5,6}| \end{pmatrix} = \begin{pmatrix} 0.9914 \\ 0.9932 \end{pmatrix}.$$

$$\boldsymbol{\kappa} = \begin{pmatrix} 0.8910 \pm i0.3370 \\ 0.6696 \\ 0.9949 \end{pmatrix} \quad |\kappa_{1,2}| = 0.9526\,,$$

which characterize the model to be stable and minimum-phase.

For the validation of the model two sets of data have been used: Data for a field gradient of 14 MV/m as well as data for a field gradient of 13 MV/m. The assumed reproducibility

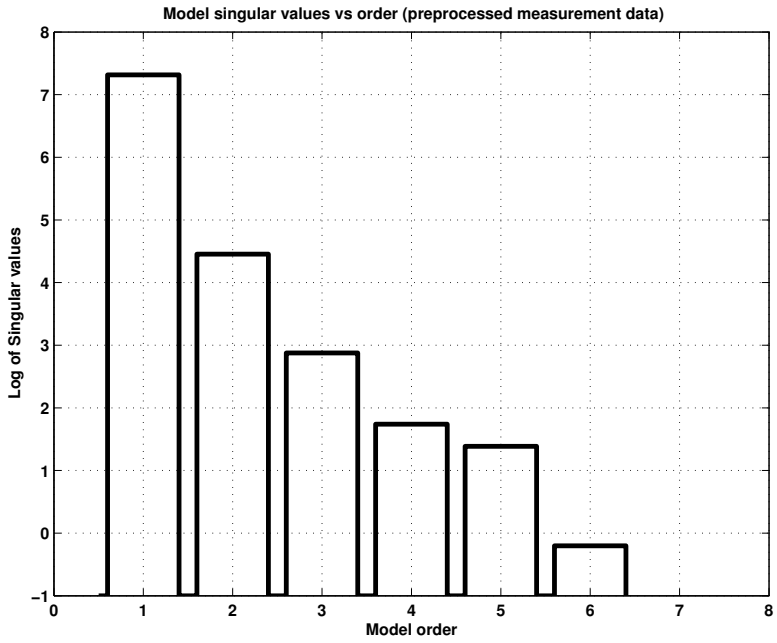

Figure 5.22: Singular values for different model orders of the Hankel matrix of preprocessed measurement data

of plant behaviour because of the gradient dependent detuning lead to the reasonable assumption that the validation performance must be adequate at least for the data set with the same gradient as the ID data. The results can be seen in Figure 5.24 and the model indeed performs well in this first validation test. The validation results for data of type 3 (bandlimited noise superimposed on feed forward tables) with a gradient of 13 MV/m is presented in Figure 5.25.

The model reproduces the output data of this lower gradient data set even more accurate than the validation data with the same gradient and can therefore be considered an adequate small signal model in the frequency range up to 100KHz and for an operating point of 14 MV/m. The frequency response of the model is shown in appendix C.

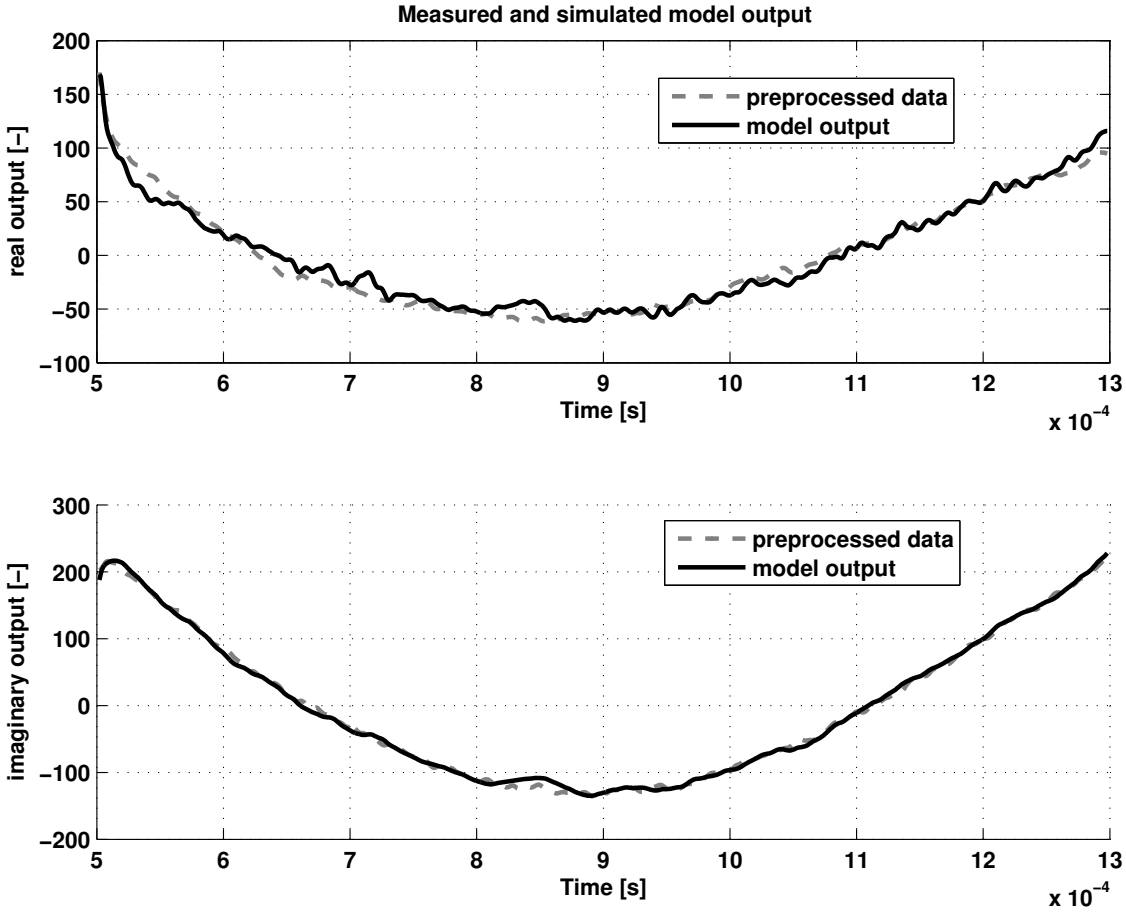

Figure 5.23: Model performance compared to measured ID data

Discussion of results

The small signal model is not compared in the sense of error functionals with the large signal models because it describes only the flat top phase and a variety of preprocessing steps have been used to develop it. All models have in common that they are stable but have eigenvalues located closely at the unit circle. The small signal model $PLDB6_x2_u2_y$ and the large signal model with estimated parameter disturbance input $GLDB3_x2_u2_y1_d$ are minimum phase models, while the model $GLDB9_x2_u2_y$ has transmission zeros with a magnitude larger than one thus it can lead to unstable closed loop behaviour if high gains for control are used. All models show very good validation performance. Because the validation performance of the model $GLDB9_x2_u2_y$ is particularly good if it is considered that it does not contain information about a parameter disturbance it will be used for the design of RF-field controllers using response optimization for the large signal behaviour.

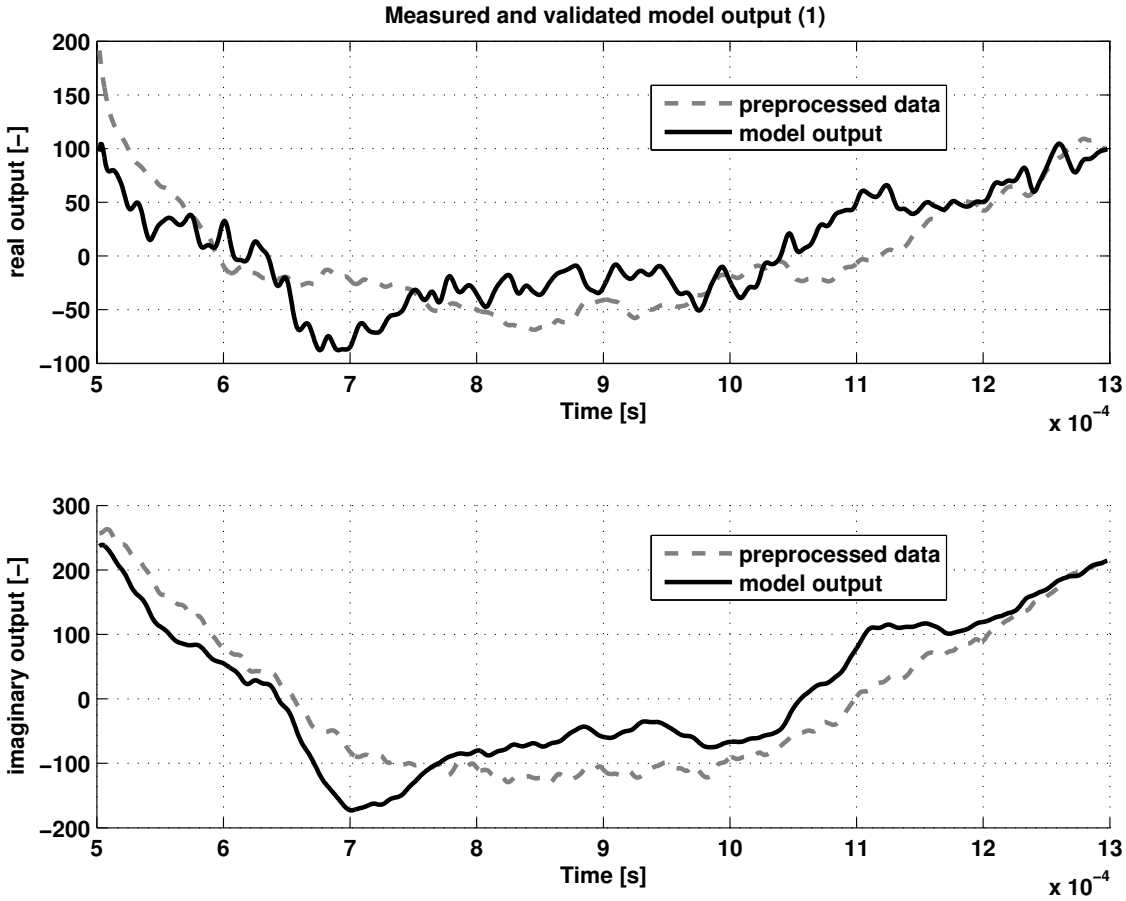

Figure 5.24: First model validation performance (Validation data of type 3 with a gradient of 14 MV/m)

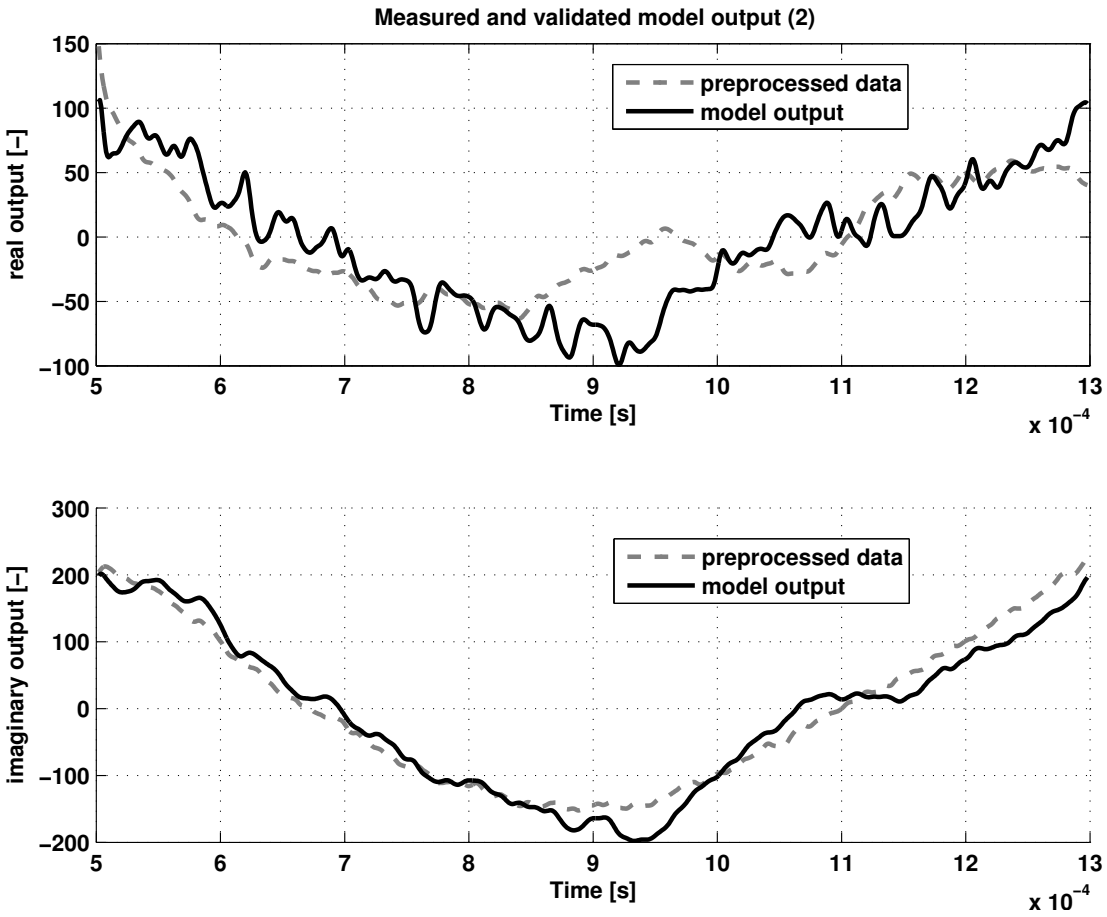

Figure 5.25: Second model validation performance (Validation data of type 3 with a gradient of 13 MV/m)

Chapter 6

Controller design by response optimization

In this chapter approaches to controller design for the RF-fields in the first accelerator module (ACC1) of TTF2 are made using one of the developed and in the previous chapter presented models. Investigations of the performance of multivariable controllers will be pointed out. A special focus shall be the reduction of overshoot during the transient from filling to flat top phase and the inestigation of controller performance with respect to given actuator constraints.

An important point is the choice of an appropriate controller structure, which will be disscussed in Section 6.1. This decision depends mainly on the model structure and the models characteristics. Ideas for the implementation of a freely parametrizable digital filter embedded in an FPGA structure have been developed. With this hardware it will be possible to test various multivariable RF-field controllers at TTF2. A brief outline of this signal processing hardware and its restrictions on the controller structure will be given.

For the parametrization of the controller optimization techniques embedded in the *SIMULINK Response Optimization Toolbox* of *MATLAB* are used. The advantage is that issues like level limitations of hardware components, actuator constraints etc. and signal bounds like maximal overshoot width can be given as constraints for the controller parameter adjustment. This signal constraints resemble nonlinearities in the control loop. The controller parameter estimation is presented in Section 6.2 and the simulation results for different multivariable controllers are shown in Section 6.3. In order to further approach the given control objectives improvement of hardware and the measurement system must be done. High performance controller synthesis methods will have to be applied. An outlook on these topic will be given in chapter 7.

The control objectives regarding amplitude and phase stability during the flat top of the RF-fields are formulated for the fields vector sum are formulated in chapter 2.2.7. They demand precision in amplitude and phase by a factor of 10^{-4}. In case of ACC1 the vector

sum of eight superconducing cavities is to be controlled.

6.1 Controller Structures

In the first instance the controller structure is determined by the number of the variables to be controlled (measured output signals of the plant) and the actuating signals (input signals of the plant). In case of ACC1 of TTF2 we have 2 actuating signals u_r and u_i (which resemble the currents I_r and I_i in the resonant circuit model) and two output signals y_r and y_i which are the real and imaginary part of the vector sum output of the complex RF-field vectors ($y_r = V_r$, $y_i = V_i$). The actuating signals are the sum of the controller output signals ($u_{c,r}$, $u_{c,i}$) and the feedforward signals f_r and f_i. The deviations from the reference trajectories (r_r,r_i) of the vector sum are the input signals of the controller and are calculated as follows

$$e_r = r_r - V_r\,, \tag{6.1}$$

$$e_i = r_i - V_i\,. \tag{6.2}$$

In the framework of this thesis only discrete time controllers are designed. An advantage is that they can easily be implemented in the digital hardware of the signal processing system of TTF2. Therefore in the following considerations only discrete time controllers are considered. The controller structure mapping plant output signals onto actuating signals can be expressed by

$$\begin{pmatrix} u_r \\ u_i \end{pmatrix} = \boldsymbol{C}_c \cdot \begin{pmatrix} y_r \\ y_i \end{pmatrix}\,. \tag{6.3}$$

Each element C_{ij} of the controller matrix $\boldsymbol{C_c}$ can be represented in the discrete time framework as a transfer function in the complex variable z (see Chapter 3.1) as follows

$$\boldsymbol{C}_c(z) = \begin{pmatrix} C_{11}(z) & C_{12}(z) \\ C_{21}(z) & C_{22}(z) \end{pmatrix}\,. \tag{6.4}$$

The order of the transfer functions depend on the control algorithm used which will be discussed in the following sections. The structure of the controller matrix $\boldsymbol{C}_c$ is mainly determined by the coupling of input and output signals of the multivariable plant. Consider a representation of the plant as a transfer function matrix $\boldsymbol{G}_p$ in discrete time domain

$$\begin{pmatrix} y_r \\ y_i \end{pmatrix} = \boldsymbol{G}_c \cdot \begin{pmatrix} u_r \\ u_i \end{pmatrix}\,, \tag{6.5}$$

where $\boldsymbol{G}$ can be expressed by

$$\boldsymbol{G}_p(z) = \begin{pmatrix} G_{11}(z) & G_{12}(z) \\ G_{21}(z) & G_{22}(z) \end{pmatrix}\,. \tag{6.6}$$

If $G_{12}(z) = G_{21}(z) = 0$ holds the plant $\boldsymbol{G}_p$ consists of two decoupled subsystems and a decentralized controller consisting of two SISO controllers in this case can be used.

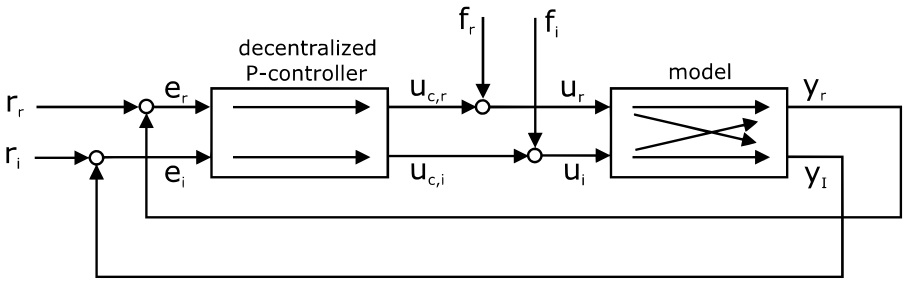

Figure 6.1: LLRF control structure with decentralized proportional feedback controller and feedforward

However, the transfer functions of all models of the RF-field behaviour discussed in this thesis have nonzero coupling elements for plant input and output signals. The only decoupled model structure is the resonant circuit model (see Section 4.1, eq.(4.29)) for the special case that the detuning is zero ($\Delta\omega = 0$ rad/s), which is an unreasonable assumption during an RF-pulse due to the field gradient dependent Lorentz forces causing detuning. It seems to be promising that replacing the decentralized P-controller (see Figure 6.1) by a multivariable controller improves the performance.

Structure of digital PID-controllers

A commonly used controller structure for single input/single output (SISO) systems is the PID controller. In continuous time domain the control law of a PID controller is

$$u(t) = k_p + \frac{1}{T_I}\int_0^t e(\tau)d\tau + k_D\dot{e}(t). \tag{6.7}$$

The output of the controller depends proportionally on the actual control error (P part), on the integral of the control error (I part) and on the actual change with respect to time of the error, the derivative of $e(t)$. Frequently used subsets of the PID controller structure are e.g. P- and PI controller.

The structure of a PID-controller can be transferred to discrete time domain by using numerical approximations for the integral and the derivative in continuous time domain, [16]. Using these approximations and the z-transform the three terms in eq.(6.7) can be representated as the discrete time control law

$$U(z) = \left(k_p + \frac{T}{2T_I}\frac{z+1}{z-1} + \frac{k_D}{T}\frac{z-1}{z}\right)E(z)\,, \tag{6.8}$$

where T denotes the sampling time. The second term in the bracket resembles the approximation of the integration and the third term approximates the continuous time derivative. An important point is that the coefficients of these terms in eq.(6.8) depend on the sampling time. The discrete time transfer function of the controller can be expressed as

$$C_{PID}(z) = \frac{c_2z^2 + c_1z + c_0}{z(z-1)}\,, \tag{6.9}$$

which is a transfer function of second order with the coefficients

$$c_2 = k_p + \frac{T}{2T_I} + \frac{k_D}{T}\,, \tag{6.10}$$

$$c_1 = -k_p + \frac{T}{2T_I} - \frac{2k_D}{T}\,, \tag{6.11}$$

$$c_0 = \frac{k_d}{T}\,. \tag{6.12}$$

The structure of the PID controller can be used for MIMO systems as well. In the framework given by eq.(6.4) each element C_{ij} can be a transfer function parametrized by means of eq.(6.9), thus representing a discrete time PID control law for the respective controller input channel i. In the following section a hardware will be presented which will be used at DESY to implement multivariable controllers for TTF2.

Controller implementation in an FPGA

FPGA is the abbreviation for *Field Programmable Gate Array*. It is a programmable logic device that incorporates integrated digital electronic circuits whose connections are not fixed but can be rearranged by programming. Thus, the FPGA enables configurable computing based on hardware dynamically adapted to a specific problem, [10]. A further advantage besides the reconfigurability of the hardware is that an FPGA allows parallel computing and can perform logical operations orders of magnitude faster than conventional signal processors.

A central focus of research concerning the LLRF control system of TTF2 is the exchange of the DSP system by an FPGA based system to make the signal processing for the control application more versatile and faster. On an FPGA digital filters can be realized that can represent a parametrizable controller structure in discrete time domain .

An FPGA based controller structure has been designed at DESY that resembles a multivariable discrete time transfer function matrix of four biproper[1] second order transfer functions.

$$\boldsymbol{C}_c(z) = \begin{pmatrix} K_{11}\frac{b_{11}z^2+a_{11}z+1}{d_{11}z^2+c_{11}z+1} & K_{12}\frac{b_{12}z^2+a_{12}z+1}{d_{12}z^2+c_{12}z+1} \\ \\ K_{21}\frac{b_{21}z^2+a_{21}z+1}{d_{21}z^2+c_{21}z+1} & K_{22}\frac{b_{22}z^2+a_{22}z+1}{d_{22}z^2+c_{22}z+1} \end{pmatrix} \tag{6.13}$$

Each transfer function matrix $C_{ij}(z)$ is characterized by five parameters that can be chosen by the coefficients. The coefficients of the transfer functions determines the position of two zeros and two poles of the transfer function in the complex plane as well as a gain factor. To be able to enforce derivative action by the controller, the structure illustrated in eq.(6.13) will be enhanced by one coefficient ν_{ij} in the denumerators to be able to place poles at the

[1] Biproper means that the degree of the numerator polynomial in z is as high as the denominator polynomial. A biproper system can follow step signals in the input directly.

origin such that eq.(6.13) becomes

$$\boldsymbol{C}_c(z) = \begin{pmatrix} K_{11}\frac{b_{11}z^2+a_{11}z+1}{d_{11}z^2+c_{11}z+\nu_{11}} & K_{12}\frac{b_{12}z^2+a_{12}z+1}{d_{12}z^2+c_{12}z+\nu_{12}} \\ \\ K_{21}\frac{b_{21}z^2+a_{21}z+1}{d_{21}z^2+c_{21}z+\nu_{21}} & K_{22}\frac{b_{22}z^2+a_{22}z+1}{d_{22}z^2+c_{22}z+\nu_{22}} \end{pmatrix} \tag{6.14}$$

The designed P- and PI-controllers in this thesis are in the form of eq.(6.13) such that the controllers can be implemented immediately on the existing FPGA hardware and tested at TTF2. PID-controllers are developed with respect to the the structure in eq.(6.14). In the next section it is shown how standard control algorithms consisting of proportional (P), integral (I) and derivative (D) feedback of the control error can be transformed to the form of eq.(6.13).

6.2 Optimization of controller parameters

The task is to test multivariable controller structures for the RF-field stabilization in simulation by using one of the developed models for the module ACC1 of the linear accelerator system. The *SIMULINK Response Optimization Toolbox* of *MATLAB* can be used to parametrize a controller structure with respect to constraints. These constraints can be specified reference trajectories that should be tracked by the plant output, actuator limitations, constraints on the step response of a system, signal limitations etc.. Especially actuator constraints and signal limitations resemble nonlinear elements in the control loop. For most linear controller design methods including signal constraints in the design is only in possible to a limited extend. The *SIMULINK Response Optimization Toolbox* is a very versatile tool to test whether a controller structure is adequate to fullfill the control task for an existing model especially if constraints are involved. However, this method can not be considered a high performance controller method like *mixed sensitivity H_2/H_∞ design* (see Chapter 7) and shall be used here to get a first impression of the performance of multivariable controllers for the control problem at hand.

For the model $GLDB9_x2_u2_y$ that has been illustrated in Chapter 5.4.1 multivariable P-,PI- and PID-controller have been designed and benchmarked with respect to their performance regarding the given control objectives. A large signal model has been chosen for these investigations of multivariable-controllers because actuator constraints specified for the whole RF-pulse and the transient behaviour between filling and flat top should be taken into account. The controller shall enforce tracking of the reference trajectories r_r and r_i when the feedforward signals are applied to "drive" the model of the ACC1 system. The feedforward and reference signals are chosen for an operating point of 14MV/m. Open loop measurement data of the vector sum of ACC1, transformed from complex signals to amplitude and phase, for this gradient is shown in Figure 6.2. The control problem is therefore a tracking problem with constraints. Disturbances are considered as output disturbances here such that the MIMO large signal model without disturbance input has been chosen for this initial multivariable controller design.

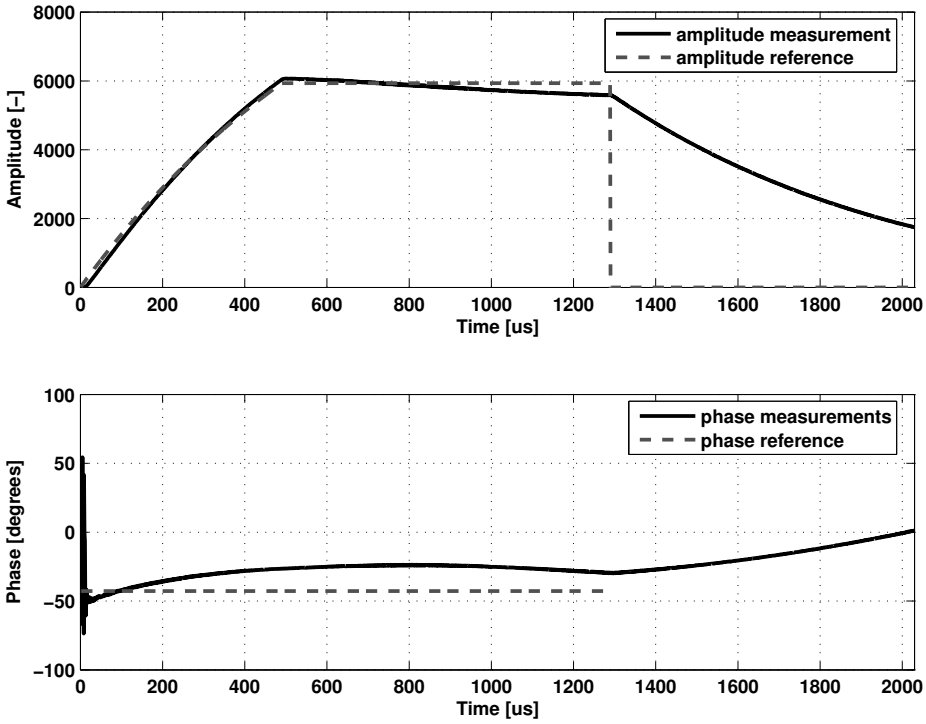

Figure 6.2: Vector sum amplitude and phase of open loop measurement data. The reference trajectories are specified until the end of the RF pulse

The control loop including the model, the controller structure of eq.(6.13) and the input signals is implemented as a SIMULINK model. The estimation of its parameters is done according to specified constraints. Here, tracking of the reference trajectories for real and imaginary part is specified as primary control objective. To specify the tracking objective the output signals of the plant model are applied to a *SIMULINK block* element called *Signal constraint*. In this element reference trajectoried for the block input signals or signal constraints can be specified. Moreover, the free parameters are specified such that simulations of the control loop are run iteratively while varying the specified parameters to optimally match the constraints in the sense of minimizing an error functional similar to the OE-model output error functional in Chapter 5.3.1.

Before the estimation process is started it must be specified what kind of numerical parameter estimation routine shall be used for solving the optimization problem of parameter estimation. For the results presented in this chapter a combination of genetic algorithms (GA), direct search and gradient based search routines has been used because the cost functionals are likely to have several local minima. Therefore the GA based search method is used first to get an appropriate initial parameter vector. Afterwards the direct serach method is used with the termination parameter values of GA as initial values to closer locate the minimum. Finally, a gradient based parameter estimation routine is used with the initial values found by the direct search method to precisely locate the minimum found by the two previous routines.

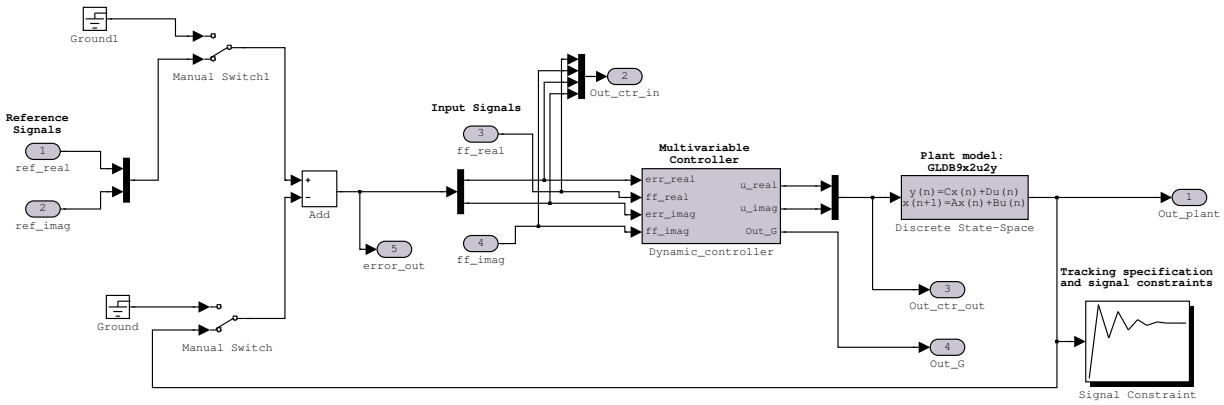

Figure 6.3: SIMULINK model for control loop with tracking controller

However, there is no guarantee given that this is the global minimum of the cost functional but the method used here for controller design should give only a first insught into the performance of multivariable controllers. High performance controllers based on the developed models will be designed in future work.

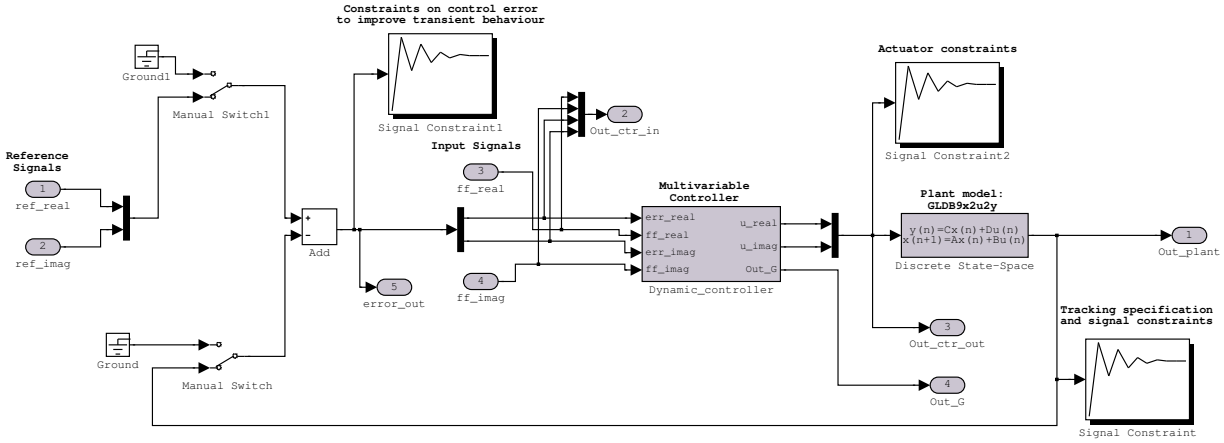

Figure 6.4: SIMULINK model of control loop with constraints

Controller design procedure with respect to constraints

For the controller design the following steps are taken:

1. First the controllers are designed purely for tracking purpose of the RF-field reference trajectory specified for real and imaginary parts of the vector sum. The tracking included in the signal constraint block connected to the output signals of the model in Figure 6.3. The controllers are benchmarked with respect to their peak-to-peak and RMS errors during the flat top.

2. To lower the peak to peak error due to overshoot occurring at the transient between filling and flat top phase, a signal constraint is applied on the control errors for both channels. The SIMULINK block diagramm of the control loop with the Signal constraint blocks is shown in Figure 6.4. The constraint on the error is tuned iteratively such that the lowest overshoot for each controller is reached. Moreover, the actuator constraint (see Chapter 2.2.8) limiting the input of the plant model is included.

The controller structures are compared with respect to the control errors during the flat top and the restriction to the give constraints.

6.3 Simulation results

The performance of the designed multivariable P,PI and PID controllers is presented here. For each controller the fixed coefficients to obtain the structure, the estimated coefficients and the peak-to-peak/rms-error (calculated for the flat top interval according to eq.(2.5) and eq.(2.6)) are specified. The flat top performance is shown in figures here while figures showing the performance for the whole RF-pulse are included in appendix D.

For the P- and the PI-controllers, the controller structure of eq.(6.13) is used, for the PID controllers the structure of eq.(6.14). The parameters are specified in tables. An "(f)" behind a parameter value denotes that this value is fixed and not a free parameter in the parameter estimation process.

For the interpretation of the results it shall be reconsidered that the model $GLDB9_x2_u2_y$ (see Chapter 5.4.1) is stable, does not have any poles with magnitude one (no model internal integrator) but is a nonminimum-phase model because it has zeros in the outer section of the unit circle (see Figure 5.19).

Multivariable P-controller

The basic new controller structure is a multivariable proportional feedback of the control error of each channel:

$$\boldsymbol{C}_c^p(z) = \begin{pmatrix} K_{11} & K_{12} \\ K_{21} & K_{22} \end{pmatrix} \tag{6.15}$$

This control algorithm can directly be realized with the FPGA controller if all coefficients except the gain factors and $\nu_{ij} = 1$ are set to zero ($a_{ij} = b_{ij} = c_{ij} = d_{ij} = 0$). The performance is shown in Figures D.1 and 6.5.

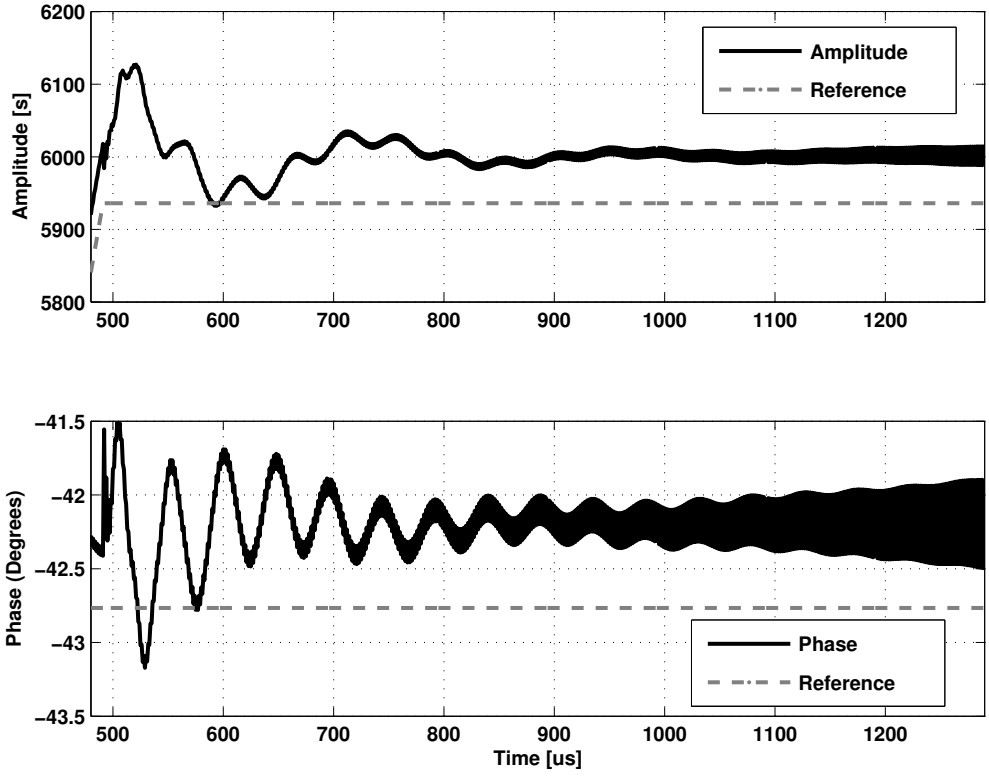

Figure 6.5: Performance of multivariable P-controller zoom (on flat top)

Result

In amplitude and phase significant overshoot can be seen. The closed loop system is unstable because the magnitude and phase perform highfrequent oscillations during the flat top with increasing magnitude. The reason is that the model is nonminimum phase and if the gains are increased further the closed loop poles of the model approaches openloop zeros whose magnitude is larger than one thus leading to instability. Moreover, no asymptotic tracking is achieved because no integral action is enforced by the controller and the model does not contain an internal integrator (pole with magnitude one). Integral action is needed to achieve asymptotic tracking of the the piecewise linear tracejectories of the input signals.

Because of the unsatisfactory asymptotic tracking behaviour which can not be completely achieved for this model by any P-controller the application of constraints on this control loop is omitted.

Table 6.1: Estimated P-controller parameters ($\nu_{ij} = 1$, (f))

Par.	**Val.**	**Par.**	**Val.**	**Par.**	**Val.**	**Par.**	**Val.**	**Par.**	**Val.**
K_{11}	1.7141	b_{11}	0 (f)	a_{11}	0	d_{11}	0 (f)	c_{11}	0 (f)
K_{12}	0.0622	b_{12}	0 (f)	a_{12}	0	d_{12}	0 (f)	c_{11}	0 (f)
K_{21}	5.0731	b_{21}	0 (f)	a_{21}	0	d_{21}	0 (f)	c_{11}	0 (f)
K_{22}	3.8355	b_{22}	0 (f)	a_{22}	0	d_{22}	0 (f)	c_{11}	0 (f)

Table 6.2: P-controller performance

	$\mathbf{e_{a,p2p}}$	$\mathbf{e_{\varphi,p2p}}$	$\mathbf{e_{a,rms}}$	$\mathbf{e_{\varphi,rms}}$
Value in %	3.28	3.89	1.22	1.44

Multivariable PI-controller

Each transfer function in eq.(6.14) has the following transfer function:

$$C_{ij}(z) = K_{ij}\frac{b_{ij}z^2 + a_{ij}z + 1}{d_{ij}z^2 + c_{ij}z + \nu_{ij}}\,. \tag{6.16}$$

For a PI controller the coefficient c_0 in the PID controller structure of eq.(6.9) is zero such that the PI controller structure for one transfer function is

$$C_{ij}^{PI}(z) = \frac{c_2 z + c_1}{z - 1}\,. \tag{6.17}$$

Comparing coefficients of eq.(6.16) and eq.(6.3) yields $b_{ij} = d_{ij} = 0$, $\nu_{ij} = -1$ and the free parameters K_{ij} and a_{ij}. The controller structure in the form realizable with the FPGA harware becomes

$$\boldsymbol{C}_c^{PI}(z) = \begin{pmatrix} K_{11}\frac{a_{11}z+1}{z-1} & K_{12}\frac{a_{12}z+1}{z-1} \\ \\ K_{21}\frac{a_{21}z+1}{z-1} & K_{22}\frac{a_{22}z+1}{z-1} \end{pmatrix} \tag{6.18}$$

The performance is shown in Figures 6.6 and D.2. The corresponding estimated parameters are included in table 6.4. The values of the control errors in amplitude and phase are listed in table 6.3.

Table 6.3: PI tracking controller performance

	$\mathbf{e_{a,p2p}}$	$\mathbf{e_{\varphi,p2p}}$	$\mathbf{e_{a,rms}}$	$\mathbf{e_{\varphi,rms}}$
Value in %	1.79	4.46	0.3	0.63

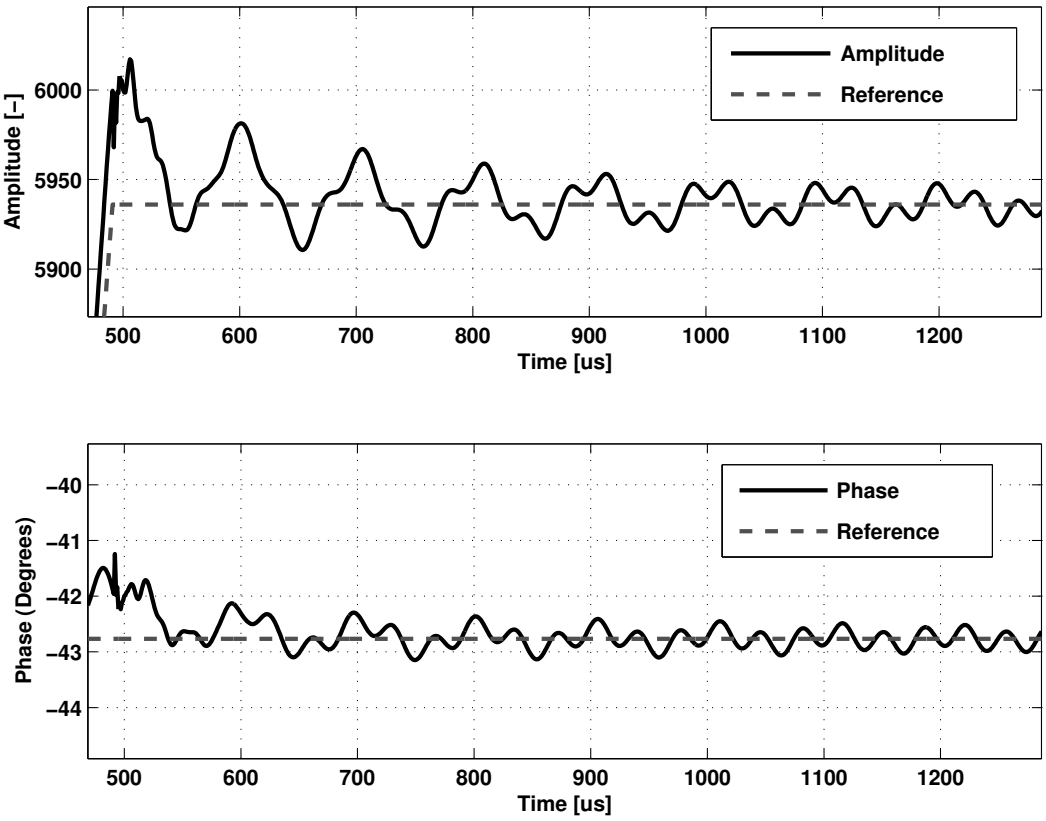

Figure 6.6: Performance of PI tracking controller

Result

Enforcing integral action leads to asymptotic tracking in amplitude and phase and for The parametrized PI controller to a stable closed loop system. However overshoot in phase is still about 2.4% of the setpoint and in amplitude 1.4% respectively. In amplitude and phase oscillations are present which could be suppressed by introducing a transmission zero. Increasing the gain however would lead to higher overshoot. The next step is to parametrize a PID controller to check how the transient behaviour can be influenced by introducing feedback of the time derivative of the control error.

Multivariable PID-controller

Recalling the transfer function elements of eq.(6.14)

$$C_{ij}(z) = K_{ij}\frac{b_{ij}z^2 + a_{ij}z + 1}{d_{ij}z^2 + c_{ij}z + \nu_{ij}}\,.$$

and the PID controller structure of eq.(6.9)

$$C_{ij}^{PI}(z) = \frac{c_2 z^2 + c_1^z + c_0}{z(z-1)}\,,$$

Table 6.4: Estimated PI-controller parameters ($\nu_{ij} = -1$, (f))

Par.	**Val.**	**Par.**	**Val.**	**Par.**	**Val.**	**Par.**	**Val.**	**Par.**	**Val.**
K_{11}	-0.8373	b_{11}	0 (f)	a_{11}	-1.178	d_{11}	0 (f)	c_{11}	1 (f)
K_{12}	-2.2159	b_{12}	0 (f)	a_{12}	-0.7875	d_{12}	0 (f)	c_{11}	1 (f)
K_{21}	0.3307	b_{21}	0 (f)	a_{21}	-1.8072	d_{21}	0 (f)	c_{11}	1 (f)
K_{22}	-5.2523	b_{22}	0 (f)	a_{22}	-1.1943	d_{22}	0 (f)	c_{11}	1 (f)

yields for the coefficients

$$d_{ij} = 1\,, \quad c_{ij} = -1\,, \quad \nu_{ij} = 0\,,$$

such that the controller structure becomes becomes

$$\boldsymbol{C}_c^{PID}(z) = \begin{pmatrix} K_{11}\frac{b_{11}z^2+a_{11}z+1}{z^2-z} & K_{12}\frac{b_{12}z^2+a_{12}z+1}{z^2-z} \\ \\ K_{21}\frac{b_{21}z^2+a_{21}z+1}{z^2-z} & K_{22}\frac{b_{22}z^2+a_{22}z+1}{z^2-z} \end{pmatrix} \tag{6.19}$$

The performance is shown in Figures 6.7 and D.3. Table 6.5 shows the corresponding estimated parameters and table 6.6 the the control errors in amplitude and phase.

Table 6.5: Estimated PID-controller parameters ($\nu_{ij} = 0$, (f))

Par.	**Val.**	**Par.**	**Val.**	**Par.**	**Val.**	**Par.**	**Val.**	**Par.**	**Val.**
K_{11}	0.021	b_{11}	0.6546	a_{11}	-0.3883	d_{11}	1 (f)	c_{11}	-1 (f)
K_{12}	0.9058	b_{12}	-0.6801	a_{12}	-0.6732	d_{12}	1 (f)	c_{11}	-1 (f)
K_{21}	-0.1907	b_{21}	0.4701	a_{21}	-1.1657	d_{21}	1 (f)	c_{11}	-1 (f)
K_{22}	0.4255	b_{22}	1.1696	a_{22}	0.0094	d_{22}	1 (f)	c_{11}	-1 (f)

Result

The parametrization of the PID controller leads to oscillations during the flat top but asymptotic tracking is reached. The overshoot is 3.4% in amplitude and 4.8% in phase. Clearly this parametrization estimated by the *SIMULINK Response optimization toolbox* for

Table 6.6: PID tracking controller performance

	$\mathbf{e}_{\mathbf{a},\mathbf{p2p}}$	$\mathbf{e}_{\varphi,\mathbf{p2p}}$	$\mathbf{e}_{\mathbf{a},\mathbf{rms}}$	$\mathbf{e}_{\varphi,\mathbf{rms}}$
Value in %	6.85	8.61	1.78	2.4

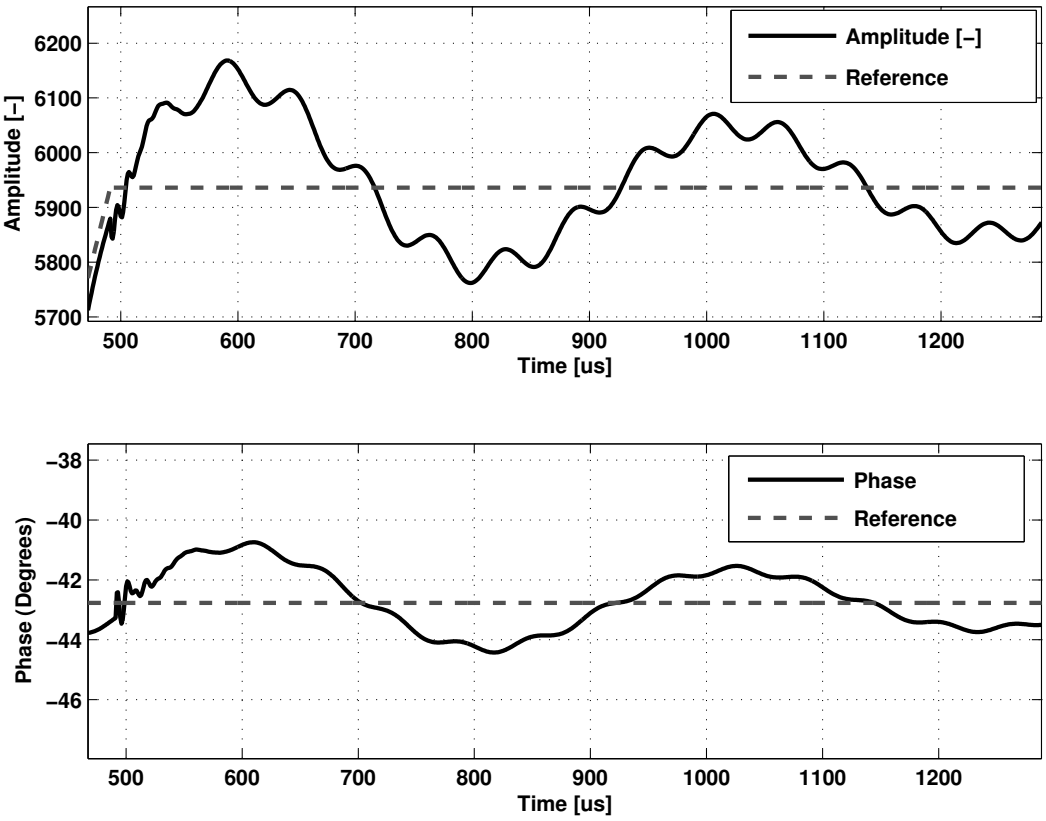

Figure 6.7: Performance of PID tracking controller

the PID controller does not lead to optimal performance: PI controllers are a subset of PID controllers which means that the performance of the optimally parametrized PID controller can not be worse than the PI controller performance. The unreasonable parametrization if the PID controller can have several causes: Either an error was present in the block diagram, numerical problems occurred in the parameter estimation process or the model is not good enough.

PI and PID controller design with respect to signal constraints

The constraints applied are signal constraints on the error signals of both channels to reduce overshoot at the beginning of the flat top phase and signal constraints on the controller output signal (sum of feedback signals and feedforward signals of each channel) to include actuator constraints for the operating point of 14MV/m (see Chapter 2.2.8). The signal constraints on the control errors have been adjusted iteratively to minimize overshoot.

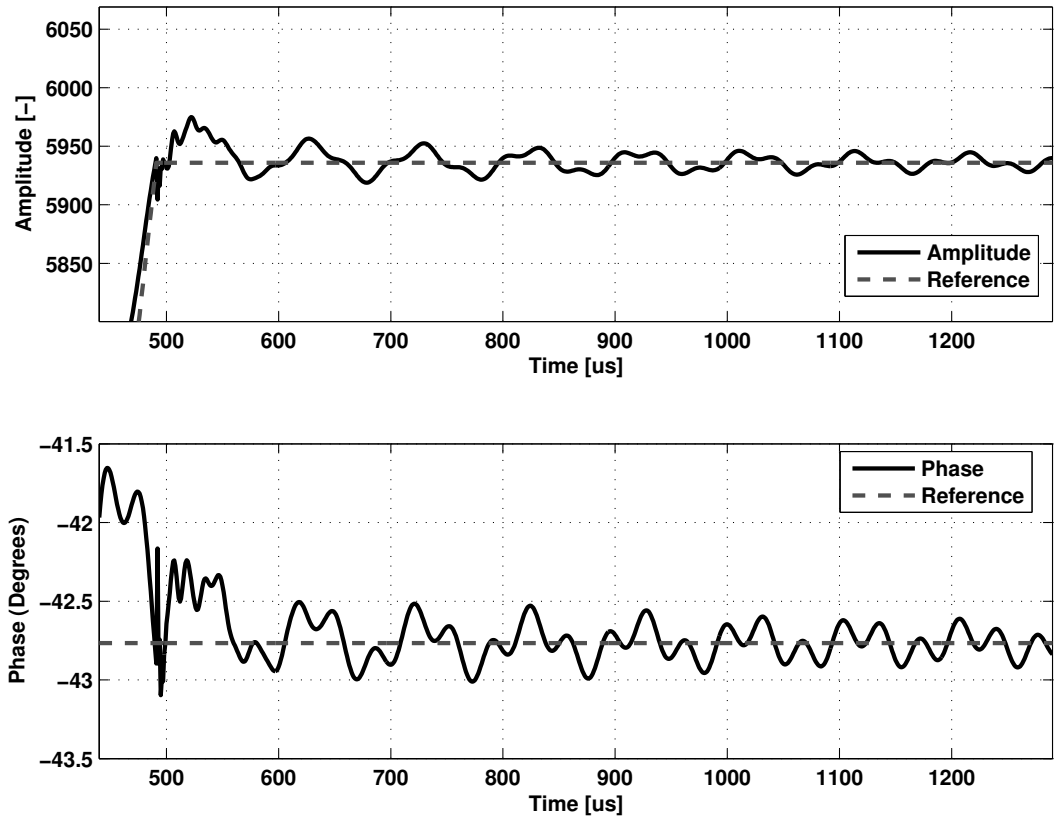

Figure 6.8: Performance of multivariable PI-controlled model with signal constraints

PI controller parametrized with respect to constraints

The initial parameters for the PI controller are the ones estimated without invocing constraints (see table 6.4). The constraints on the error signals that can be fullfilled with the PI-controller are presented in table D.1. In the Figures 6.9 and D.7 the constraints and the resulting control errors for a controller parametrization according to table D.1 are shown.

The resulting performance in amplitude and phase stabilization is shown in Figures 6.8 and D.4. Moreover, in appendix D the performance by means of real and imaginary part of the vector sum is illustrated (Figures D.5 and D.6).

Without violating the actuator constraints (Figure D.8) a significant reduction in overshoot by 1.2% in amplitude and 0.7% in phase compared to the PI tracking controller without constraints (see Section 6.3) has been achieved thus leading to a better transient behaviour between filling and flat top interval and to lower control errors.

Table 6.7: Estimated PI-controller parameters with respect to signal constraints ($\nu_{ij} = -1$, (f))

Par.	**Val.**	**Par.**	**Val.**	**Par.**	**Val.**	**Par.**	**Val.**	**Par.**	**Val.**
K_{11}	-0.9521	b_{11}	0 (f)	a_{11}	-1.8100	d_{11}	0 (f)	c_{11}	1 (f)
K_{12}	-2.0901	b_{12}	0 (f)	a_{12}	-0.7505	d_{12}	0 (f)	c_{11}	1 (f)
K_{21}	0.3614	b_{21}	0 (f)	a_{21}	-1.9181	d_{21}	0 (f)	c_{11}	1 (f)
K_{22}	-5.0786	b_{22}	0 (f)	a_{22}	-1.2541	d_{22}	0 (f)	c_{11}	1 (f)

Table 6.8: PI tracking controller performance with respect to signal constraints

	$\mathbf{e_{a,p2p}}$	$\mathbf{e_{\varphi,p2p}}$	$\mathbf{e_{a,rms}}$	$\mathbf{e_{\varphi,rms}}$
Value in %	1.19	2.18	0.16	0.35

PID controller parametrized with respect to constraints

The actuator constraints given are the same as for the PI-controller and are not violated by the parametrized PID controller (see Figure D.12). The error signal constraints given for the PI controller are violated by the PID controller with the obtained parametrization (see Figures D.11).

The amplitude and phase performance for the PID controller parametrization that least violates the signal constraints is shown in Figure 6.10 and Figure D.10. The achieved error values of this PID controller are denoted in table 6.9 and its parameters are shown in table 6.10.

Overshoot in amplitude could be reduced by a factor of 2.7% and in phase by 1.9% compared to the PID controller parametrized without respect to constraints. However, the problems discussed for the PID controller parametrized without respect to constraints are still present. The PID controller parametrization is clearly not optimal. Varying the initial values for the parameter estimation did not improve the result which again implies structural errors.

Table 6.9: PID controller performance with respect to signal constraints

	$\mathbf{e_{a,p2p}}$	$\mathbf{e_{\varphi,p2p}}$	$\mathbf{e_{a,rms}}$	$\mathbf{e_{\varphi,rms}}$
Value in %	2.60	3.31	0.57	0.07

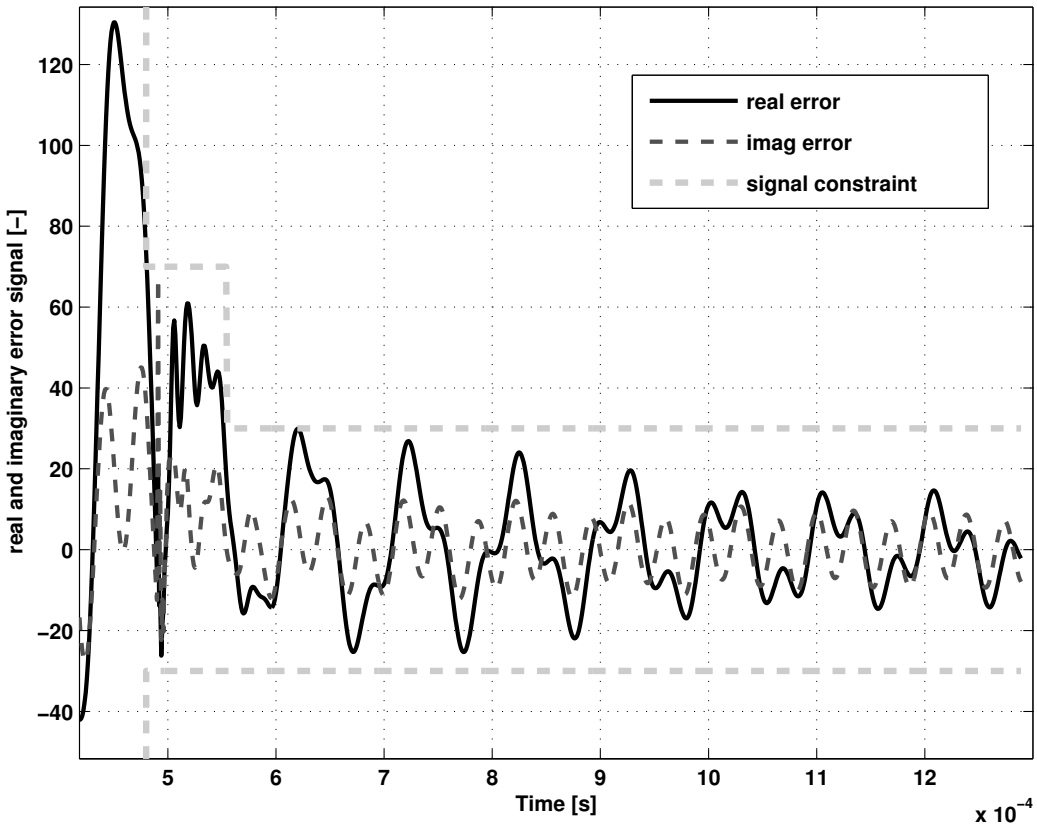

Figure 6.9: Real and imaginary control errors for PI-controlled model with signal constraints

Discussion of results

The controller winning the benchmark is the PI-controller parametrized for signal constraints in the model. The resulting control errors are $\mathbf{e_{a,p2p}} = 1.19$, $\mathbf{e_{\varphi,p2p}} = 2.18$, $\mathbf{e_{a,rms}} = 0.16$ and $\mathbf{e_{\varphi,p2p}} = 0.35$. With a multivariable P controller structure no asymptotic tracking can be achieved because neither in the controller nor in the model integral action is present that ensures asymptotic tracking of the piecewise linear input signals. The PID controller ensures asymptotic tracking but shows a worse performance than the PI controller which implies errors in its parametrization.

The control error values achieved in simulations with the PI controller are about a magnitude far from the XFEL-control objectives although no disturbance of the output signals by the beam has been considered. The fact that even with this assumptions the control objectives can not be fullfilled implies that changes in the controller structure alone are not sufficient to fullfill the control objectives. Structural changes including rejection of mechanical disturbances by active damping with piezo-actuators, improvement of electronical components to reduce noise etc. are crucial to reduce control errors. Moreover, disturbance models are needed to adequately design disturbance rejection controllers.

However, multivariable control involving integral action will clearly reduce the control errors

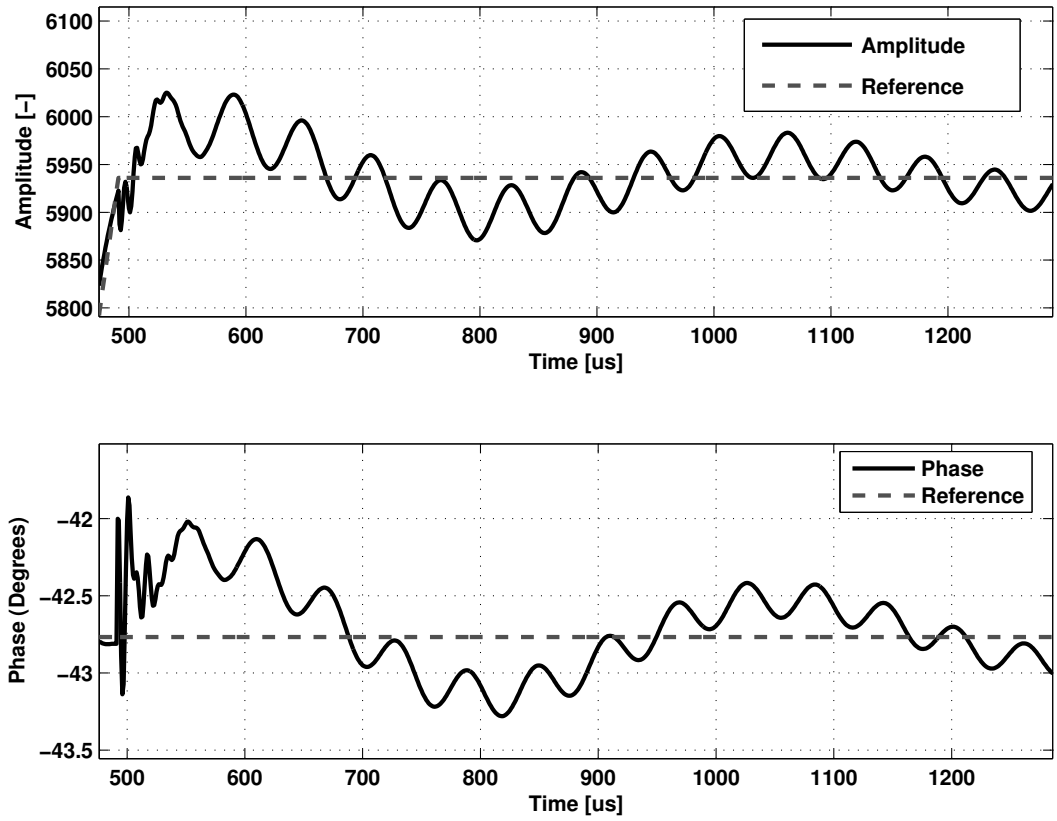

Figure 6.10: Amplitude and phase for PID-controlled model with signal constraints

during the flat top. High performance controller synthesis methods like *mixed* H_2/H_∞ *design* should also be applied. Their application without hardware improvements however will not lead to the achievement of the control objectives because of the methods conservatism due to robustness aspects.

Table 6.10: Estimated PID-controller parameters with respect to signal constraints ($\nu_{ij} = 0$, (f))

Par.	**Val.**	**Par.**	**Val.**	**Par.**	**Val.**	**Par.**	**Val.**	**Par.**	**Val.**
K_{11}	0.0198	b_{11}	0.6525	a_{11}	-0.3786	d_{11}	1 (f)	c_{11}	-1 (f)
K_{12}	0.8935	b_{12}	-0.6826	a_{12}	-0.6726	d_{12}	1 (f)	c_{11}	-1 (f)
K_{21}	-0.1832	b_{21}	0.4884	a_{21}	-1.1704	d_{21}	1 (f)	c_{11}	-1 (f)
K_{22}	0.4262	b_{22}	1.1703	a_{22}	0.0017	d_{22}	1 (f)	c_{11}	-1 (f)

Chapter 7

Conclusion and outlook

The construction of an X-ray free electron laser (XFEL) requires RF-fields in the superconducting cavities that are very precise in amplitude and phase. Besides improving technical components of the accelerator system the vector sum control algorithm of the LLRF control system must be refined in order to make the XFEL project at DESY successful. The synthesis of high performance controllers is model based, i.e. the quality of the designed controller crucially depends on the accuracy of the model. The severe control objectives regarding the amplitude and phase precision are formulated for the flat top phase of the RF-pulse where the acceleration process of the electrons takes part. Therefore models of the linear accelerator system do not only have to describe large signal behaviour of the system accurately but also the small signal I/O behaviour of the RF-fields during the flat top phase in particular. So far the dynamical behaviour of the superconducting cavities has been described by a model that has been developed using first principles, namely analogies of superconducting cavities to an electrical resonant circuit. The model is an LPV model because it has the linear time varying parameter $\Delta\omega(t)$, which resembles the detuning of a superconducting cavity.

Although this model is approriate for physical analysis of the cavity behaviour its applicability for controller design is poor because of its lack of accuracy. Model verification has been performed using an output error structure. Parameter estimation algorithms minimize the output error functional denoting the deviation of the model output from measurement data to parametrize the model structure. The results have been presented in Chapter 4. The poor accuracy of the model regarding small signal I/O behaviour during the flat top phase and transient behaviour between filling and flat top motivates the development of models by system identification.

System identification experiments have been designed and performed at the first accelerator module of TTF2. Thus, experimental based grey and black box LTI models for the I/O behaviour of ACC1 have been developed including large signal models for the whole RF-pulse and its single phases as well as a small signal model for the flat top. Three models proved particularly good output prediction performance for ID and validation data:

- A third order large signal model ($GLDB3_x2_u2_y1_d$) describing the vector sum of the modules during the RF-pulse by a third order state space model with an estimated parameter disturbance input that takes effects of cavity detuning into account. The model has been developed using subspace methods in combination with genetic algorithms and direct search based parameter estimation for the parametrization of the additional input signal. The model sets the benchmark of the large signal models describing the RF-pulse and the decay phase of the RF-fields very accurately.

- A large signal ninth order state space model ($GLDB9_x2_u2_y$) describing the RF-pulse which has been developed with *MATLABs System Identification Toolbox* . The model is an output error model that shows good validation performance although it does not contain a parameter disturbance input.

- A small signal sixth order state space model($PLDB6_x2_u2_y$) for the flat top phase developed using various measurement data preprocessing steps and very accurately describing the flat top behaviour in a gradient range from 13MV/m to 14MV/m.

The models have been analyzed regarding their eigenvalues and transmission zero distribution. All models are LTI models and thus well applicable for a variety of controller design methods.

The model ($GLDB9_x2_u2_y$) has been chosen for a first design approach of multivariable controllers. The design has been performed with respect to nonlinear elements in the control loop like actuator constraints and signal limits. The signal limits have been included to improve the transient behaviour of the vector sum signals between filling and flat top phase. A multivariable discrete time controller structure consisting of four second order transfer functions has been parametrized using the *SIMULINK Response Optimization Toolbox* such that P-,PI- and PID-controllers could be benchmarked with respect to the control errors during the flat top phase. The controller structure has been chosen with respect to applicability in FPGA hardware. The results are promising and a PI-controller structure has shown best performance so far without violating the given actuator constraints. Current work involves the integration of the controller structure on an FPGA board.

However, the obtained simulation results are still about an order of magnitude away from fullfilling the control objectives for the XFEL. It must be stated clearly that improving the controller structure alone will not lead to the achievement of the control objectives. The main aspect will be to improve measurement hardware and the actuating system by means of lower noise levels. Moreover, the active vibration damping of the superconducting cavities using piezo-actuators must be further developed to effectively compensate mechanical disturbances. New controller structures can possibly incorporate more actuating signals once the active damping of cavity vibrations has evolved at TTF2. Thus, detuning of the cavities can be actively reduced at each single cavity and the system will no longer be underactuated. Future work on controller design should be the design of high performance controllers e.g. *mixed H_2/H_∞ controller synthesis* in combination with evolutionary algorithms, which is a current field of research. However, the conservatism in the design of

robust control methods will certainly lead to problems in fullfilling the objectives without improved hardware.

A further aspect of future work will be to determine how well the developed models describe the first accelerator module of TTF2 in the presence of the electron beam and over longer periods of time. The last aspect refers to the fact that the system constantly evolves and changes over time because new components are added and the calibration is refined. Models of the disturbances must be developed to design adequate disturbance rejection controllers.

A possible approach to overcome the problem that a parametrized model does not describe the system over longer periods of time adequately is to use *adaptive control* which involves online system identification and updating the controller parameters with respect to the actual model parameters. In [4] an *active identification* for control of discrete-time uncertain nonlinear systems is proposed. *Active identification* in this context means that the control input of a system is used to drive the system state to points in state space such that unknown parameters can be identified in finite time and the controller parameters are adapted adequately. A similar approach could be used for identification of TTF2 in between the RF-pulses because this time interval of up to one second remains unused so far.

Bibliography

[1] Brinkmann, R. et al., *TESLA XFEL Technical Design Report*, DESY, Hamburg, 2002

[2] Bronstein, I.N. et al., *Taschenbuch der Mathematik*, Harri Deutsch, Frankfurt am Main, 2001

[3] Camaccho, E.F., Bordons, C., *Model Predictive Control*, Springer, London, 2004

[4] Feng, Gang., Lozano, Rogelio, *Adaptive Control Systems*, Newnes, Oxford, 1999

[5] Gassot, H., *Mechanical stability of the RF superconducting cavities*, Proceedings of EPAC 2002, Paris, 2002

[6] Hecht, Eugene, *Optics*, Addison Wesley, Boston, 2003

[7] Isermann, Rolf, *Mechatronische Systeme - Grundlagen*, Springer, Berlin, 1999

[8] Isermann, Rolf, *Identifikation dynamischer Systeme 1*, Springer, Berlin, 1992

[9] Isermann, Rolf, *Identifikation dynamischer Systeme 2*, Springer, Berlin, 1992

[10] Koch, Andreas, *Regular Datapaths on Field Programmable Gate arrays*, Phd-Thesis, Braunschweig, 1997

[11] Liepe, M. et al., *Dynamic Lorentz Force Compensation with a Fast Piezoelectric Tuner*, TESLA Note 2001-3, Hamburg, 2001

[12] Liepe, M., *Regelung supraleitender Resonatoren mit Strahlbelastung*, Diploma-Thesis composed at DESY, Hamburg, 1998

[13] Liepe, M., *Superconducting Multicell Cavities for Linear Colliders*, Phd-Thesis, Hamburg, 2001

[14] Ljung, Lennart, *System identification - A theory for the user*,Prentice Hall, New Jersey, 1999

[15] Lunze, Jan, *Regelungstechnik 1*, Springer, Berlin, 2001

[16] Lunze, Jan, *Regelungstechnik 2*, Springer, Berlin, 2002

[17] Otten, Ernst, *Repetitorium Experimentalphysik*, Springer, Berlin, 1998

[18] Richard, R., Schneider, J. R., Trines, D., Wagner, A., *TESLA Technical Design Report*, DESY, Hamburg, 2001

[19] Saldin, E.L., Schneidmiller, E. A., Yurkov, M. V., *The Physics of Free Electron Lasers*, Springer, Berlin, 2000

[20] Schilcher, Thomas, *Vector sum control of pulsed accelerating fields in lorentz force detuned superconducting cavities*, Dissertation, Hamburg, 1998

[21] Segrè, Emilio, *From X-rays to Quarks: Modern Physicists and Their Discoveries*, W.A. Freeman & Co, San Francisco, 1980

[22] Svelto, Orazio, *Principles of Lasers*, Kluwer Academic / Plenum Publishers, New York, 1998

[23] Sexl, Roman U., *Relativität, Gruppen, Teilchen*, Springer, New York, 1992

[24] The Mathworks, *System Identification Toolbox User's Guide*, The Mathworks, Inc., Natick, 2004

[25] Van Overschee, P., DeMoor, B., *Subspace Identification of Linear Systems: Theory, Implementation, Applications*, Kluwer Academic Publishers, Dordrecht, 1996

[26] Verdult, Vincent, *Nonlinear System Identification - A state space approach*, Twente University Press, Enschede, 2002

[27] Werner, Herbert, *Principles of control systems*, UMIST Control Systems Centre Lecture Notes, Manchester, 1999

[28] Werner, Herbert, *Control systems 2*, TUHH Lecture notes, Hamburg, 2003

[29] *www.xfel.net/de*

[30] Zinke, Otto, Brunswig, Heinz, *Hochfrequenztechnik 1*, Springer, Berlin, 2000

Appendix A

Singular value decomposition

For every matrix $\boldsymbol{M} \in \mathbb{R}^{l\times m}$ there exist matrices $\boldsymbol{Q} \in \mathbb{R}^{l\times l}$ and $\boldsymbol{V} \in \mathbb{R}^{m\times m}$ such that the following decomposition is done

$$\boldsymbol{M} = \boldsymbol{Q}\boldsymbol{\Sigma}\boldsymbol{V}^T \; . \tag{A.1}$$

In eq.(A.1) $\boldsymbol{Q}$ and $\boldsymbol{V}$ are orthogonal matrices and $\boldsymbol{\Sigma} \in \mathbb{R}^{l\times m}$ is a diagonal matrix with nonnegative elements. The diagonal elements σ_{ii} of $\boldsymbol{\Sigma}$ are called *singular values*. The rank of the matrix $\boldsymbol{M}$ is equal to the number of nonzero singular values.

Assume that the singular values are ordered in decreasing magnitude and $p = \min(l, m)$

$$\sigma_1 \geq \sigma_2 \geq \ldots \geq \sigma_r \geq \sigma_{r+1} \geq \ldots \sigma_p \; . \tag{A.2}$$

If there is a significant decay of magnitude in the singular values such that $\sigma_{r+1} \ldots \sigma_p$ are much smaller than σ_r the matrix $\boldsymbol{M}$ has full rank but is close to being singular. Therefore r is called the *numerical rank* of $\boldsymbol{M}$.

If $\boldsymbol{q}_i$ denotes the i^{th} column of $\boldsymbol{Q}$ and $\boldsymbol{v}_i^T$ denotes the i^{th} column of $\boldsymbol{V}$, eq.(A.1) can be written as

$$\boldsymbol{M} = \sum_{i=1}^{p} \sigma_i \boldsymbol{q}_i \boldsymbol{v}_i^T = \sum_{i=1}^{r} \sigma_i \boldsymbol{q}_i \boldsymbol{v}_i^T + \sum_{i=r+1}^{p} \sigma_i \boldsymbol{q}_i \boldsymbol{v}_i^T = \boldsymbol{Q}_s \boldsymbol{\Sigma}_s \boldsymbol{V}_s^T + \boldsymbol{Q}_n \boldsymbol{\Sigma}_n \boldsymbol{V}_n^T \; . \tag{A.3}$$

The matrices $\boldsymbol{Q}_s \in \mathbb{R}^{l\times r}$ and $\boldsymbol{V}_s \in \mathbb{R}^{m\times r}$ are formed by the first r columns of $\boldsymbol{Q}$ and $\boldsymbol{V}$. By the remaining columns the matrices $\boldsymbol{Q}_n$ and $\boldsymbol{V}_n$ are formed similarly. The term $\boldsymbol{Q}_n \boldsymbol{\Sigma}_n \boldsymbol{V}_n^T$ on the right hand side of eq.(A.3) can be neglected if the corrresponding singular values $\sigma_{r+1}, \ldots, \sigma_p$ are very small. Thus, eq.(A.1) can be approximated by

$$\boldsymbol{M} \approx \boldsymbol{Q}_s \boldsymbol{\Sigma}_s \boldsymbol{V}_s^T \; . \tag{A.4}$$

Furthermore noticeable is the following relation resulting from the orthogonality of $\boldsymbol{Q}$ (which holds for $\boldsymbol{V}$ analogously), [28]:

$$\boldsymbol{Q}\boldsymbol{Q}^T = \begin{pmatrix} \boldsymbol{Q}_s^T \\ \boldsymbol{Q}_n^T \end{pmatrix} \begin{pmatrix} \boldsymbol{Q}_s & \boldsymbol{Q}_n \end{pmatrix} = \begin{pmatrix} \boldsymbol{I} & \boldsymbol{0} \\ \boldsymbol{0} & \boldsymbol{I} \end{pmatrix} \; . \tag{A.5}$$

Appendix B

Diagrams for chapter 5

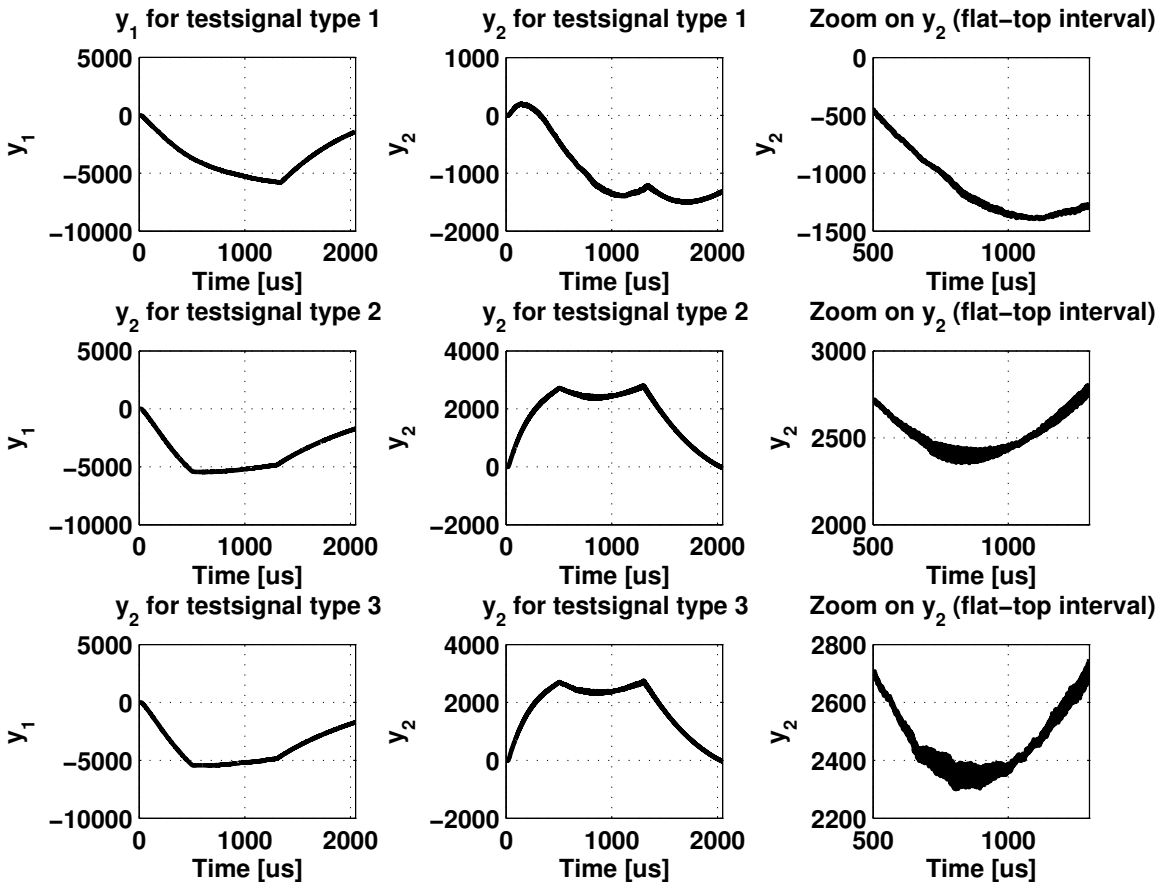

Figure B.1: Measured vector sum signals

Table B.1: Model name convention

Letter position index	**Abbreviating letter and meaning**
1	G (global model for whole RF-pulse) P (piecewise model for single phase)
2	L (linear model) N (nonlinear model)
3	C (continuous time), D (discrete time)
4	model structure W (white), G (grey), B (black)
5	model order
6	x (states)
7	number of control inputs
8	u (inputs)
9	number of outputs
10	y (outputs)
11	number of disturbance inputs
12	d (disturbance inputs)
13	number of model (if necessary)

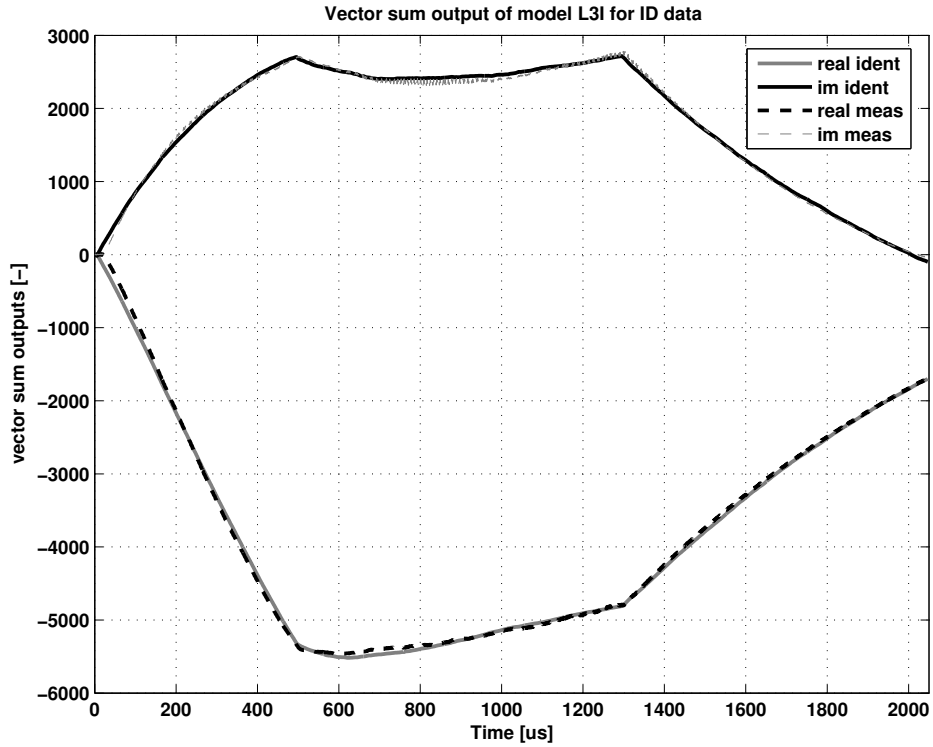

Figure B.2: Vector sum ID data (gradient 14MV/m, type 3 input) for third order large signal model identification

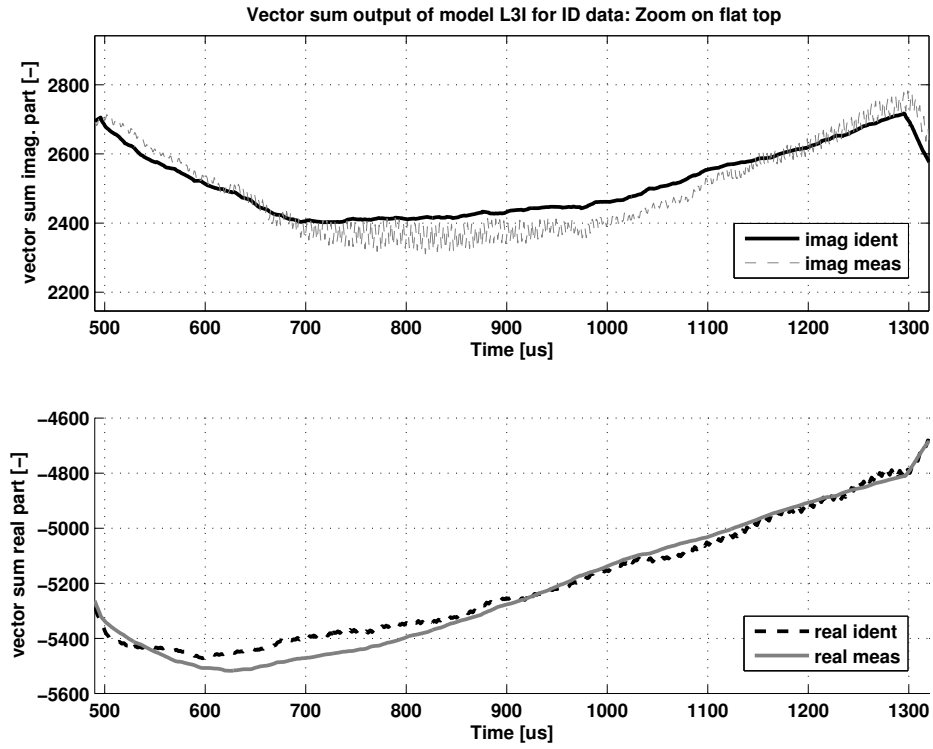

Figure B.3: Zoom on flat top of ID data shown in Figure B.2

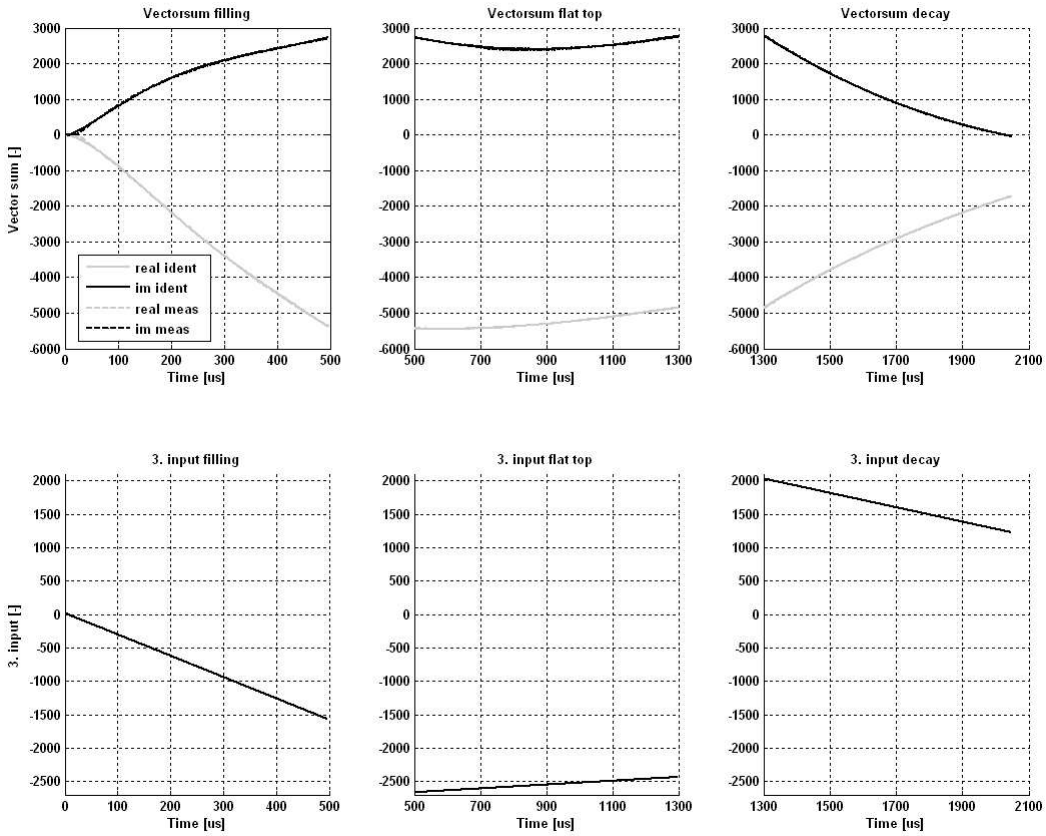

Figure B.4: Partwise identification results with partwise linear third input

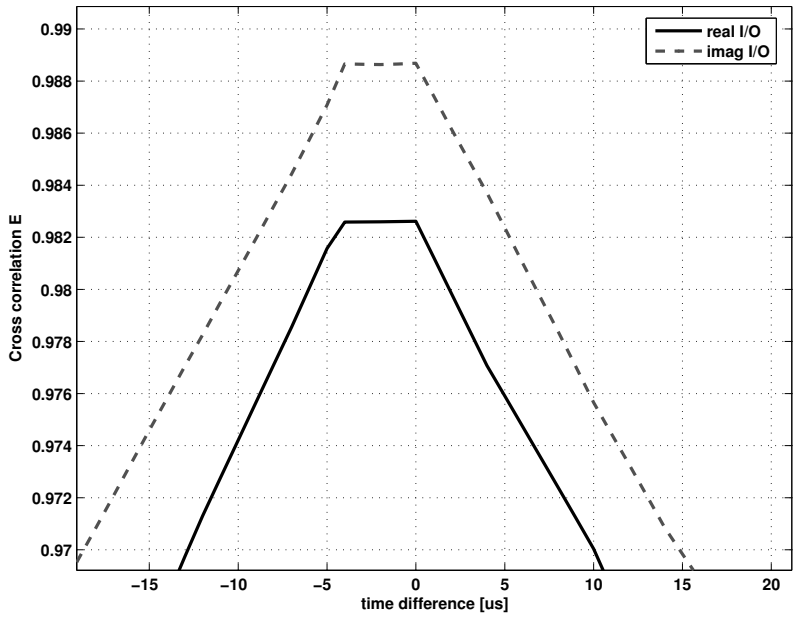

Figure B.5: Cross-correlation of input and output signals (maximum is at $\tau = 0$)

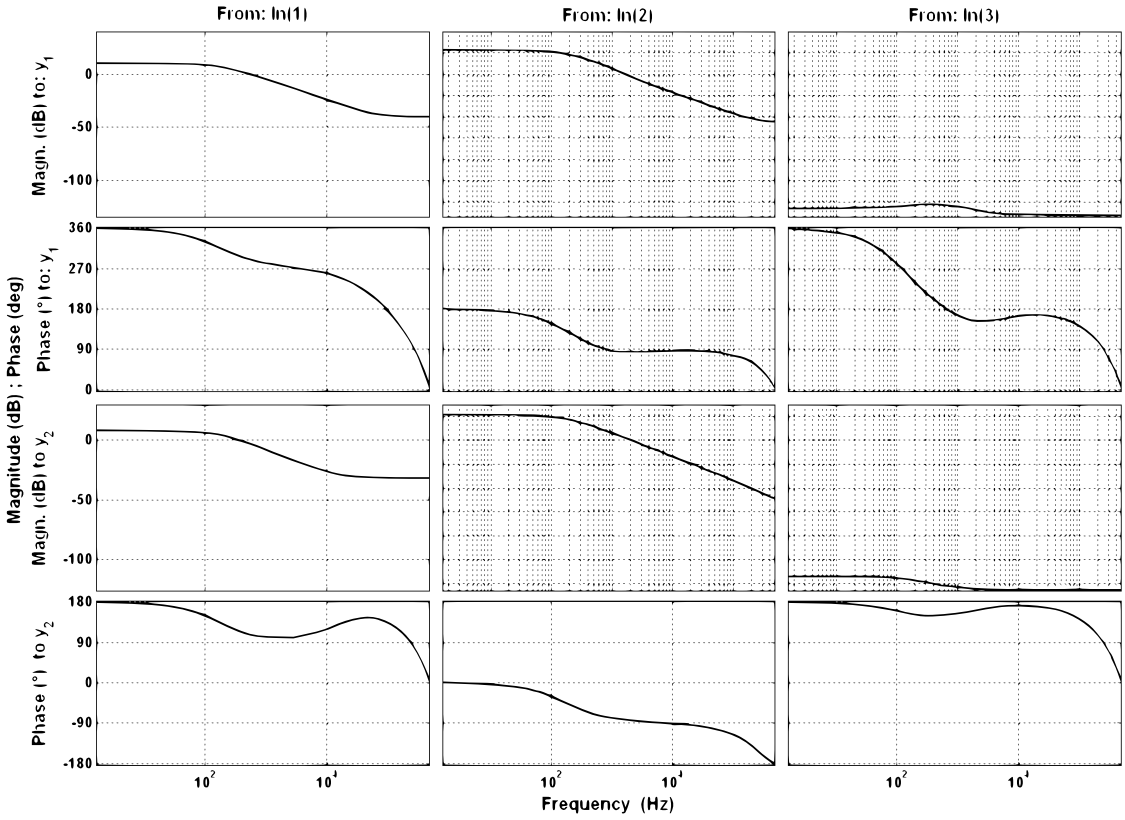

Figure B.6: Frequency response of model $GLDB3_x2_u2_y1_d$

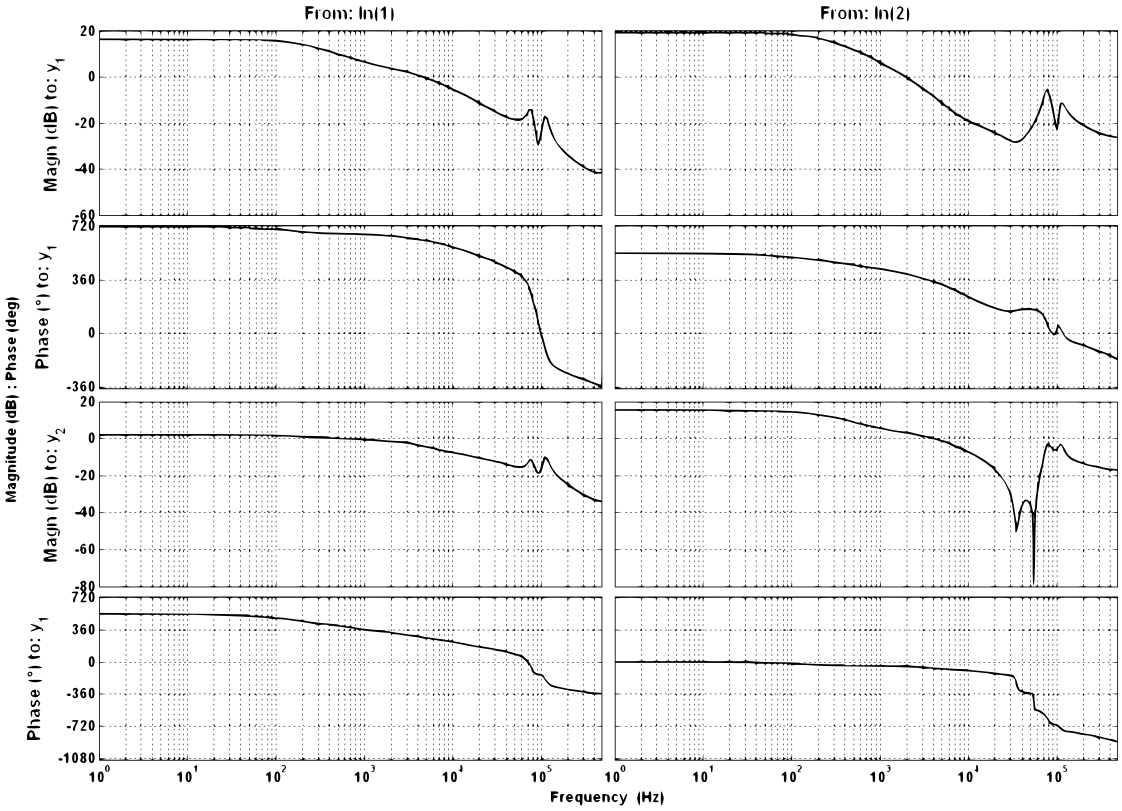

Figure B.7: Frequency response of model $GLDB9_x2_u2_y$

Appendix C

Details of the small signal model development

In chapter 5.4 a model that describes the small signal behaviour of TTF2 has been presented. Here some diagrams visualizing certain preprocessing steps and modelling results are shown:

C.0.1 Periodograms of low pass filtered ID data

In the preprocessing the I/O data used for model parametrization has been low pass filtered using a corner frequency of $f_c = 100$ kHz. The frequency contents of the raw and preprocessed I/O signals are represented in the two periodograms shown in Figure C.1 and C.2.

The theory of periodograms is described thoroughly in [14], here only a brief description shall be given. Suppose a sinusoidal signal $u(t)$ with a frequency ω

$$u(t) = \cos(\omega t) = \Re(e^{i\omega t}) \tag{C.1}$$

with $\Re$ denoting the real part of the Euler's complex representation of trigonometric functions. Considering a finite sequence of inputs $u(t)$, $t = 1, 2, \ldots, N$ the following function $U_N(\omega)$ can be defined as

$$U_N(\omega) = \frac{1}{\sqrt{N}} \sum_{t=1}^{N} u(t) e^{i\omega t} \,. \tag{C.2}$$

Furthermore considering values for $\omega = 2\pi k/N$ with $k = 1, \ldots, N$ eq.(C.2) forms the discrete fourier transform of the sequence of signals for N frequencies ω called u_1^N. Using the inverse discrete fourier transform and the property of periodicity of $u(t)$ the following relationship can be obtained (omitting a detailed derivation)

$$u(t) = \frac{1}{\sqrt{N}} \sum_{k=-N/2+1}^{N/2} U_N(2\pi k/N) e^{i2\pi kt/N} \,. \tag{C.3}$$

The contribution of the frequency $\omega = 2\pi k/N$ to the signal power of $u(t)$ is resembled by the absolute square value $|U_N(2\pi k/N)|^2$. A periodogram of a signal $u(t)$, $t = 1, 2, \ldots, N$ is thus defined by the value

$$|U_N(\omega)|^2 . \tag{C.4}$$

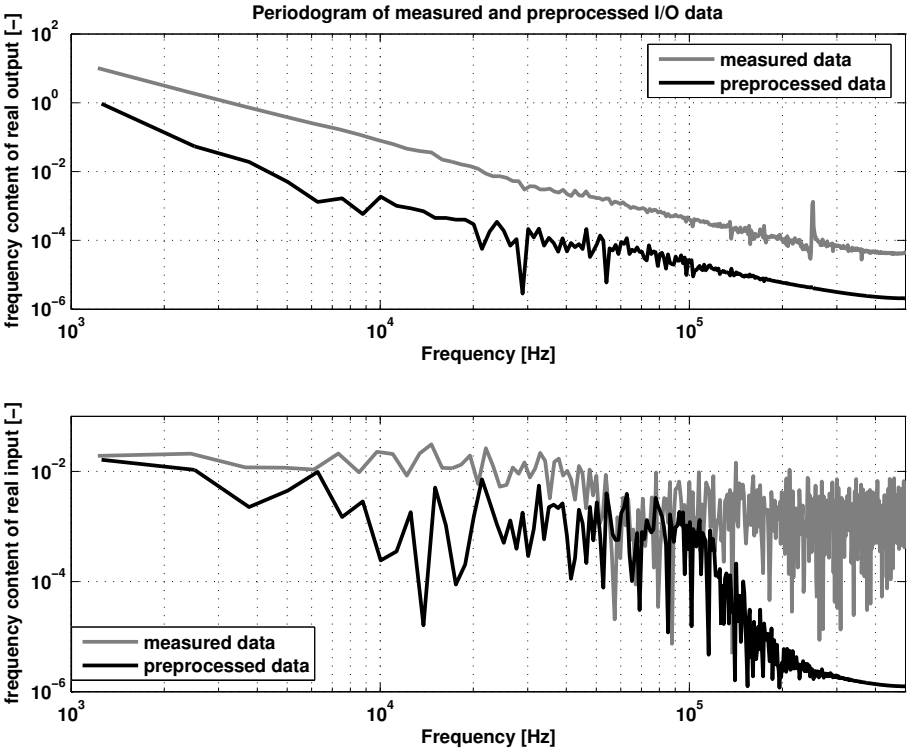

Figure C.1: Periodogram of real input and output signals

From Figure C.1 and C.2 it can be seen that the high frequent noise at a frequency of 250 kHz is filtered out. The level of the individual frequencies has been decreased after the preprocessing because the preprocessing involved removal of linear trends and mean values as well thus leading to a lower signal power.

C.0.2 Frequency response

The small signal models frequency response is shown in Figure C.3.

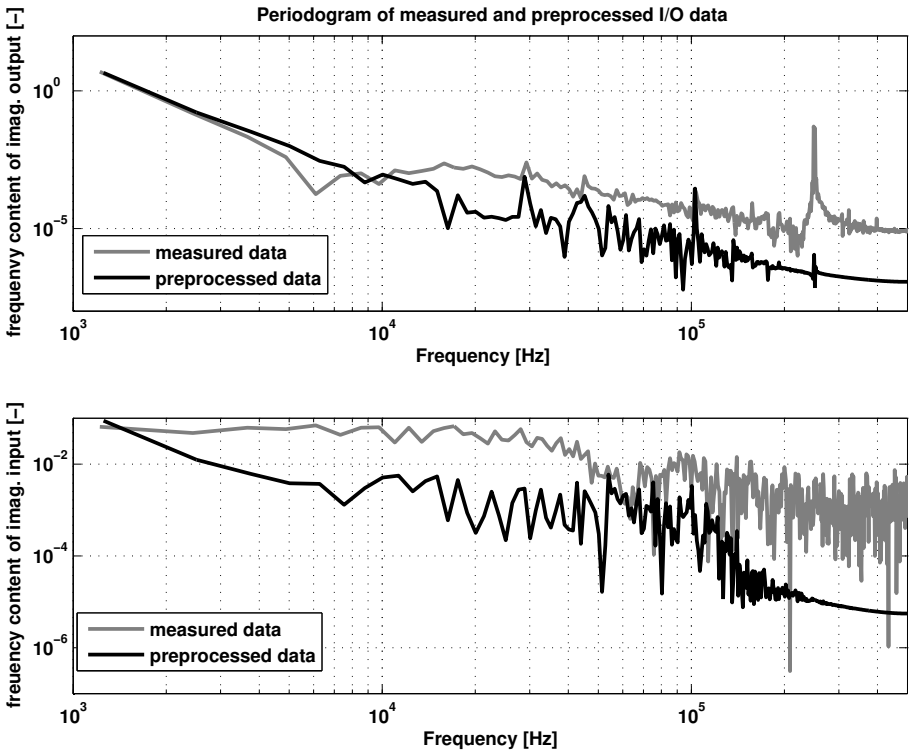

Figure C.2: Periodogram of imaginary I/O signals

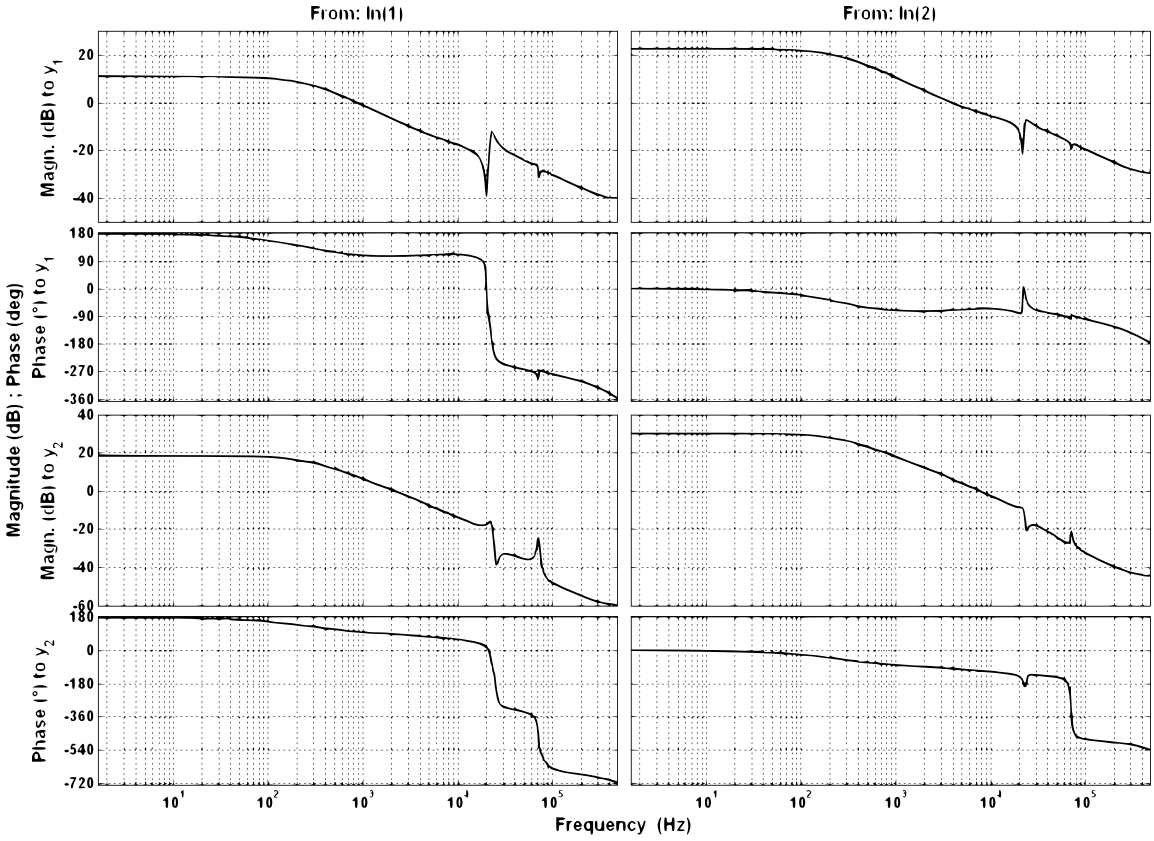

Figure C.3: Frequency response of small signal model $PLDB6_x2_u2_y$

Appendix D

Further Diagrams and tables for controller performance

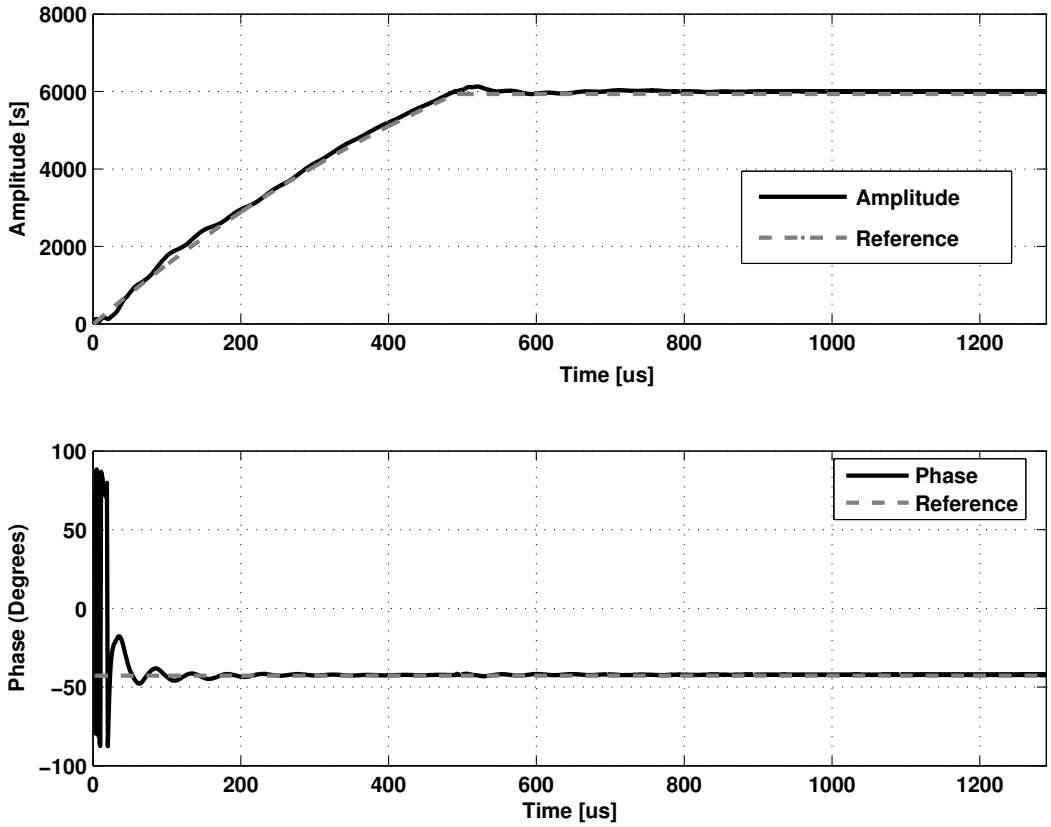

Figure D.1: Large signal behaviour performance of multivariable P-controller

Table D.1: Error signal constraints for PI controller

Time interval [μ**s**]	**Signal range of** e_r **and** e_i
0 - 480	$\pm$1000
481 - 540	-80 to 50
541 - 1300	$\pm$30

Table D.2: Error signal constraints for PID controller

Time interval [μ**s**]	**Signal range of** e_r **and** e_i
0 - 480	-1000 to 1000
481 - 540	-100 to 100
541 - 1300	-50 to 50

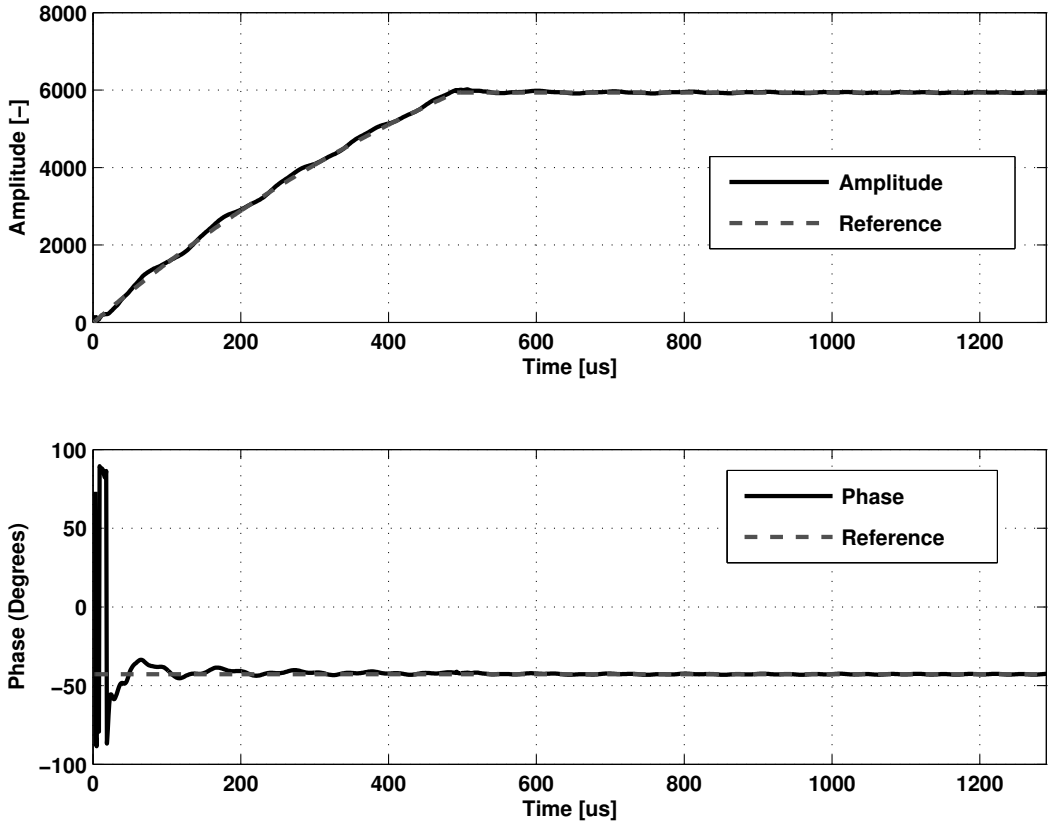

Figure D.2: Large signal behaviour performance of multivariable PI-controller (no signal constraints)

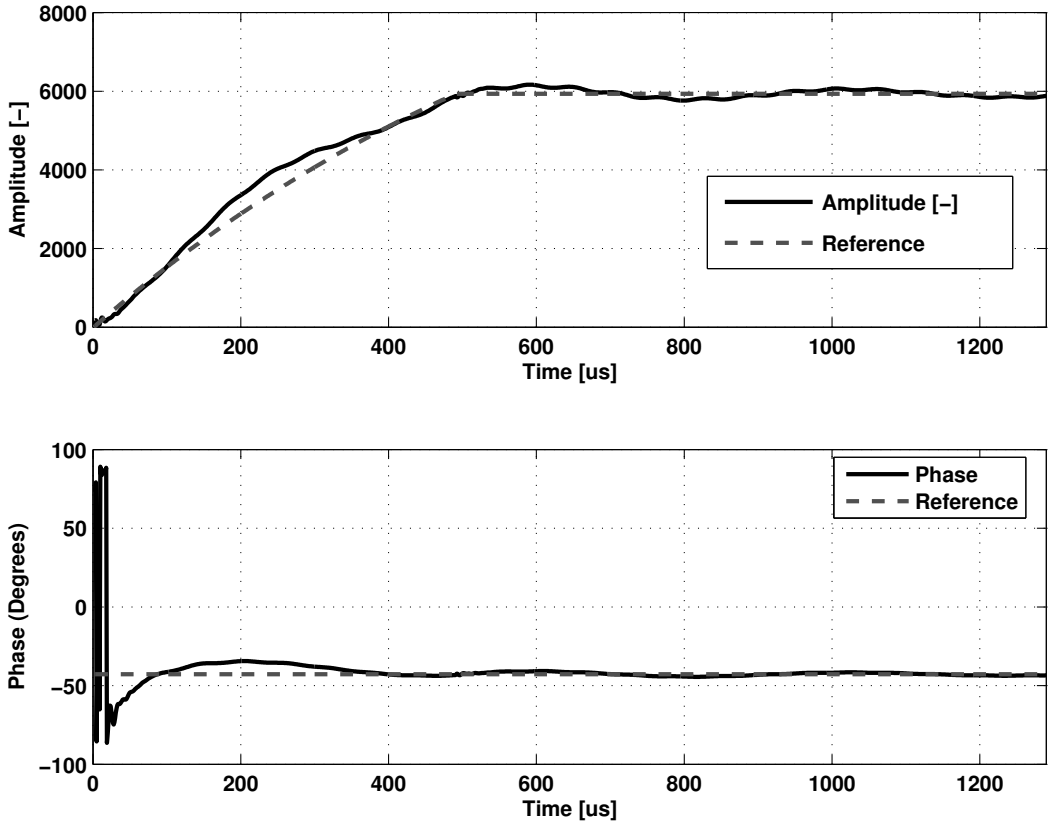

Figure D.3: PLarge signal behaviour performance of multivariable PID-controller (no signal constraints)

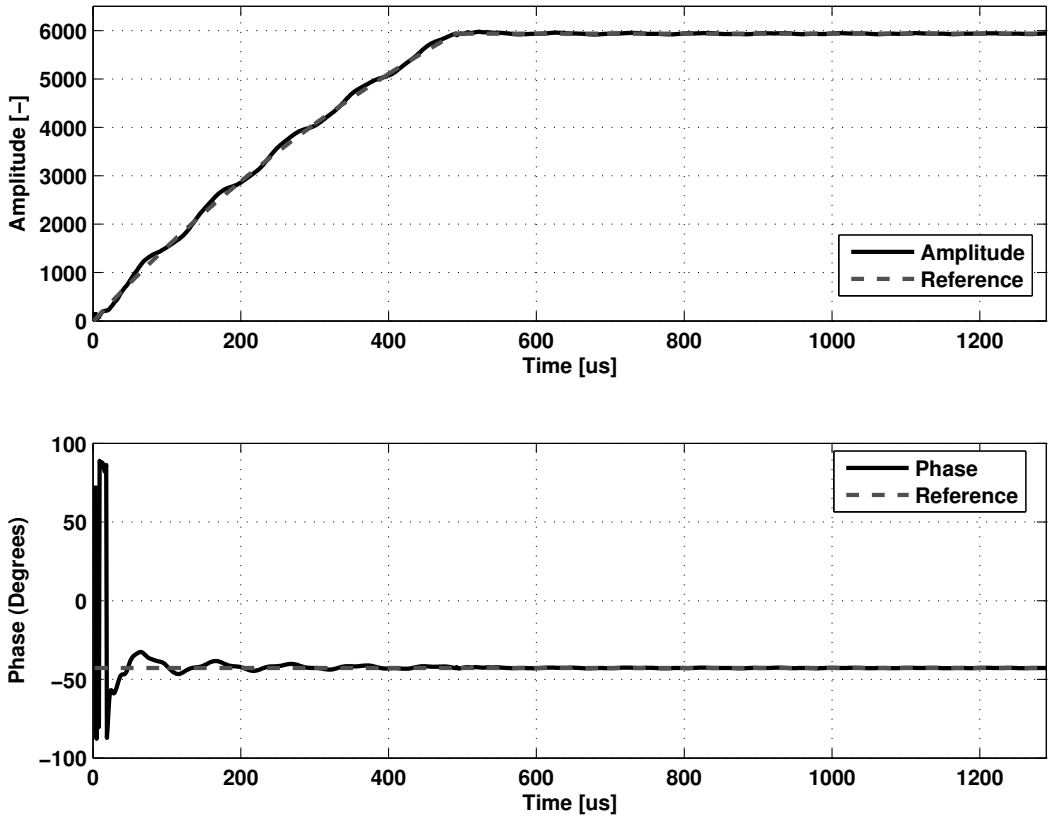

Figure D.4: Large signal behaviour performance for PI-controlled model with signal constraints

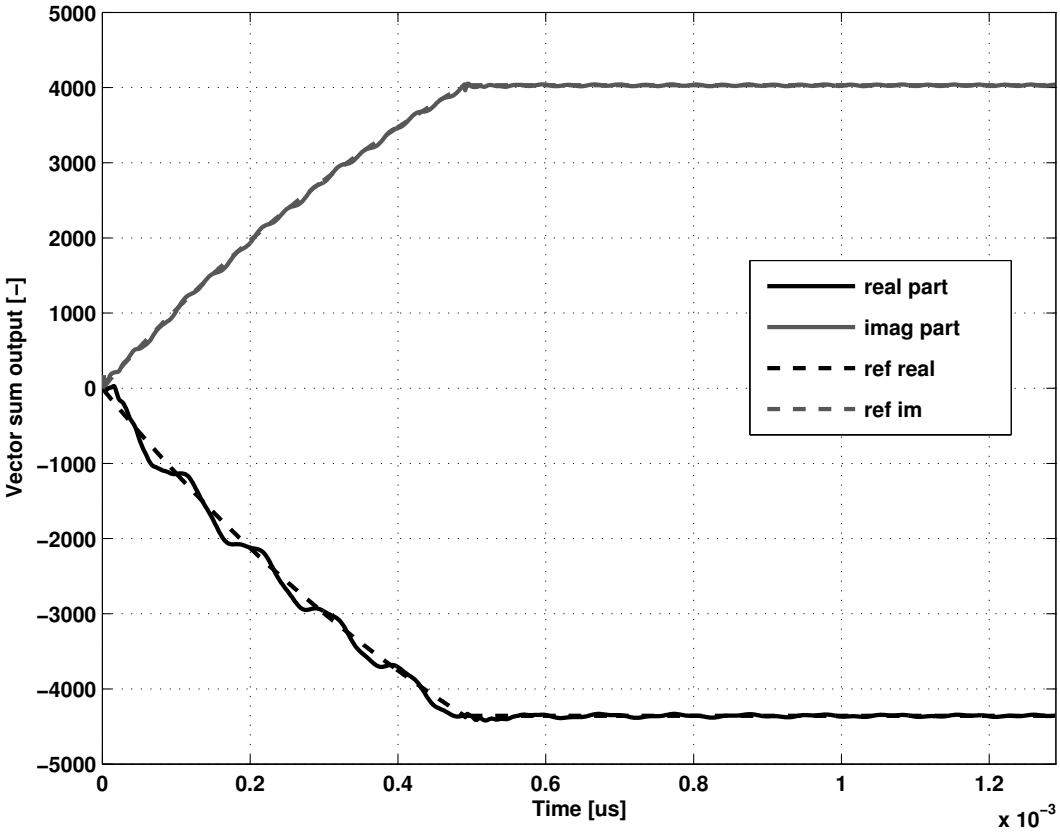

Figure D.5: Real and imaginary part (for whole RF-pulse) for PI-controlled model with signal constraints

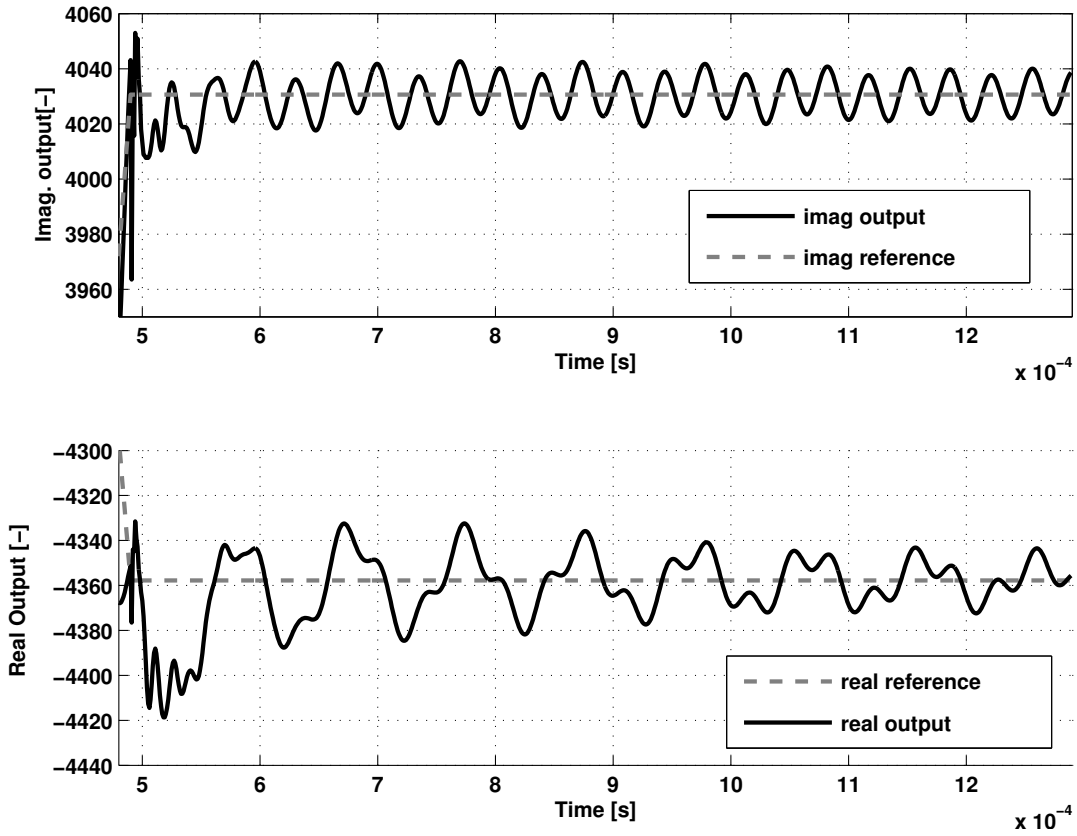

Figure D.6: Zoom on real and imaginary part for PI-controlled model with signal constraints

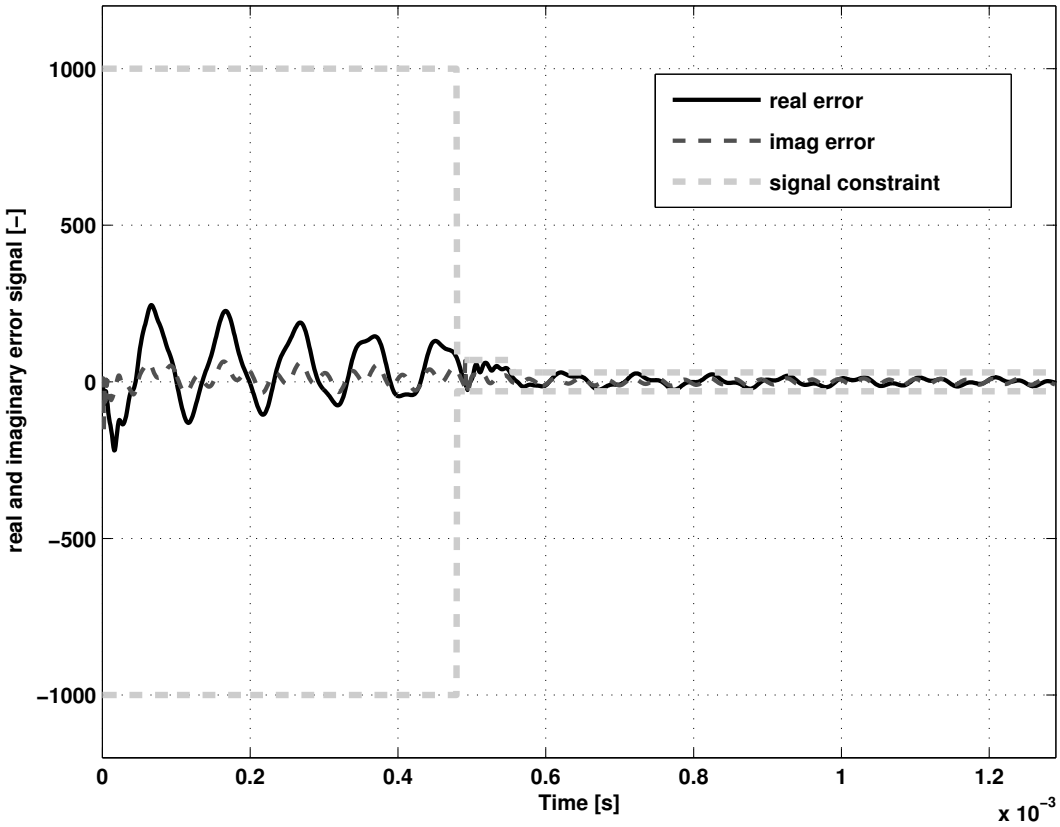

Figure D.7: Real and imaginary control errors (zoom on flat top) for PI-controlled model with signal constraints

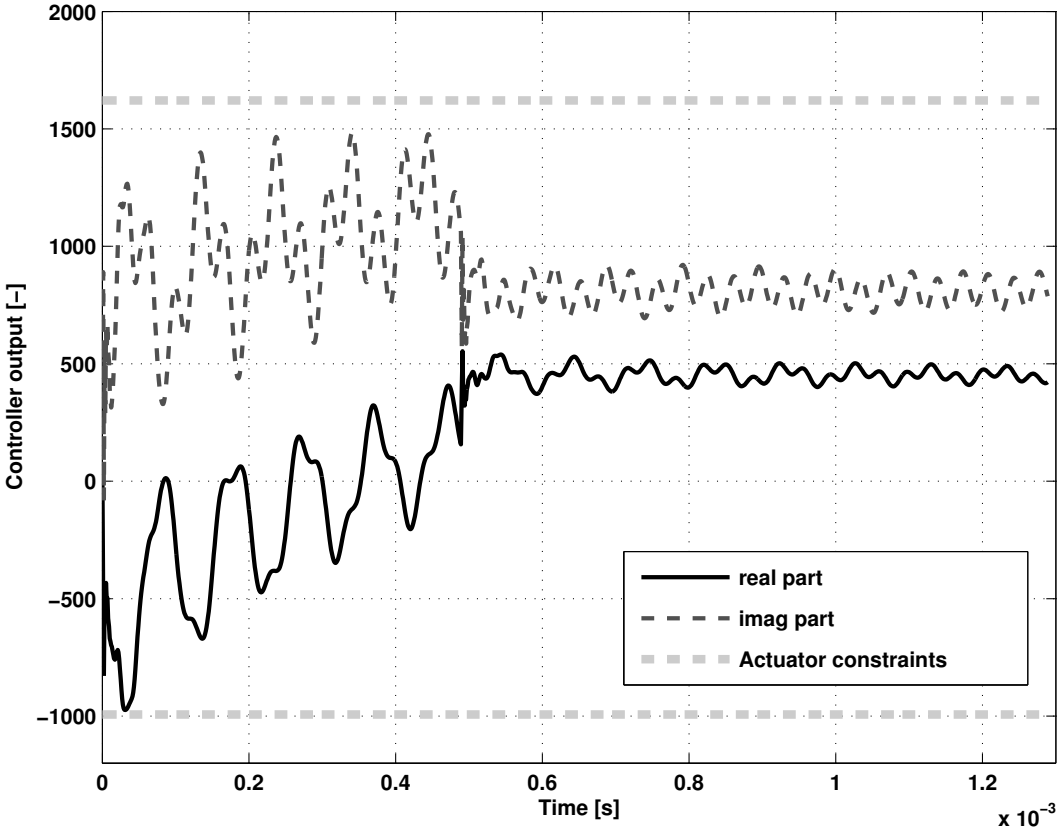

Figure D.8: Real and imaginary controller output signals (u_r and u_i) and actuator constraints (PI-controller)

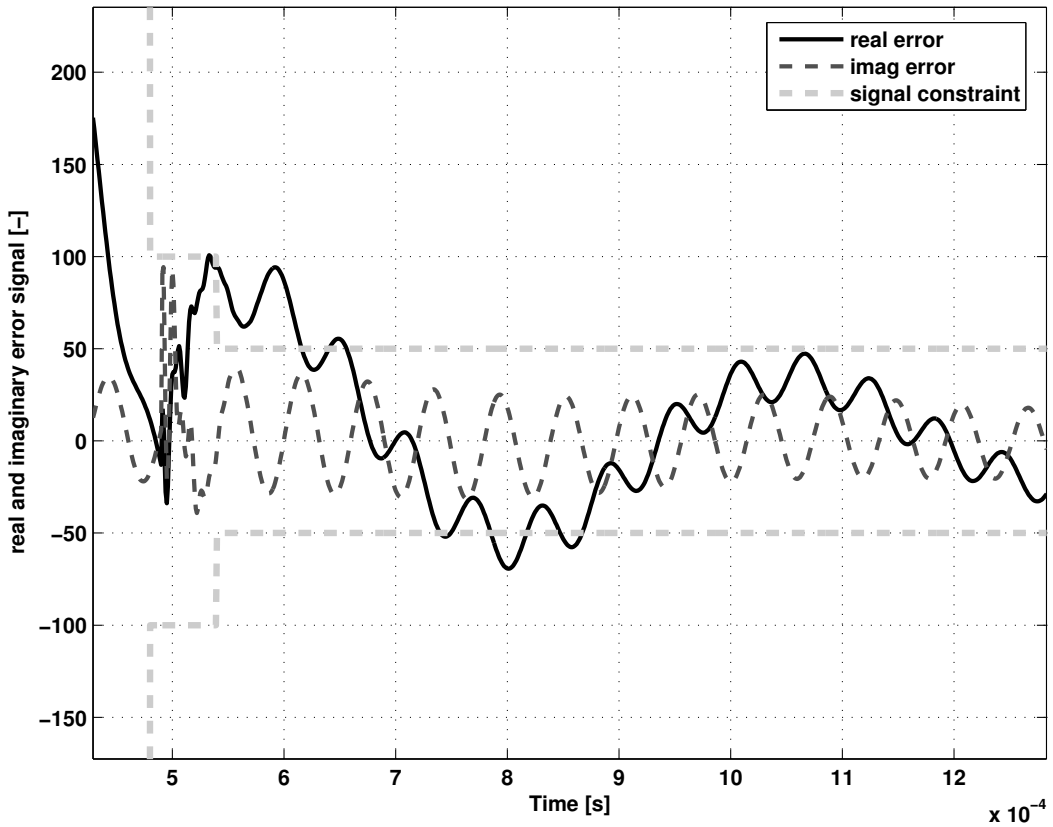

Figure D.9: Real and imaginary control errors for PID-controlled model with signal constraints

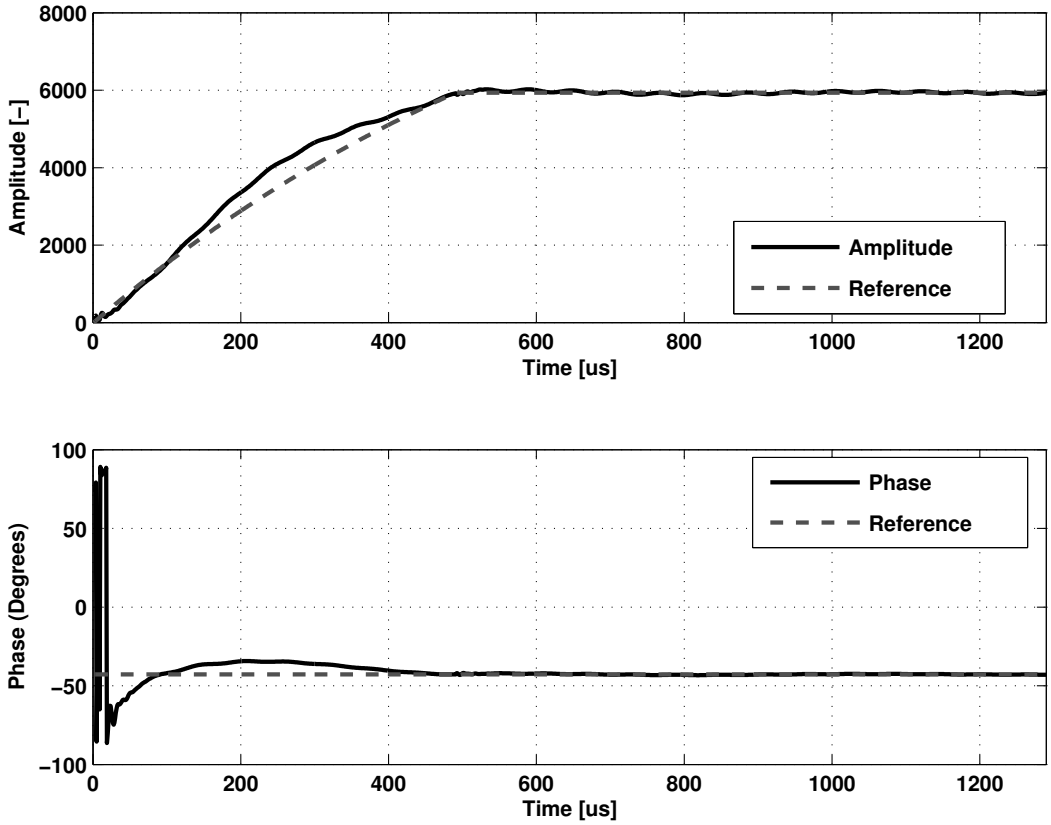

Figure D.10: Large signal behaviour performance of PID-controlled model with signal constraints

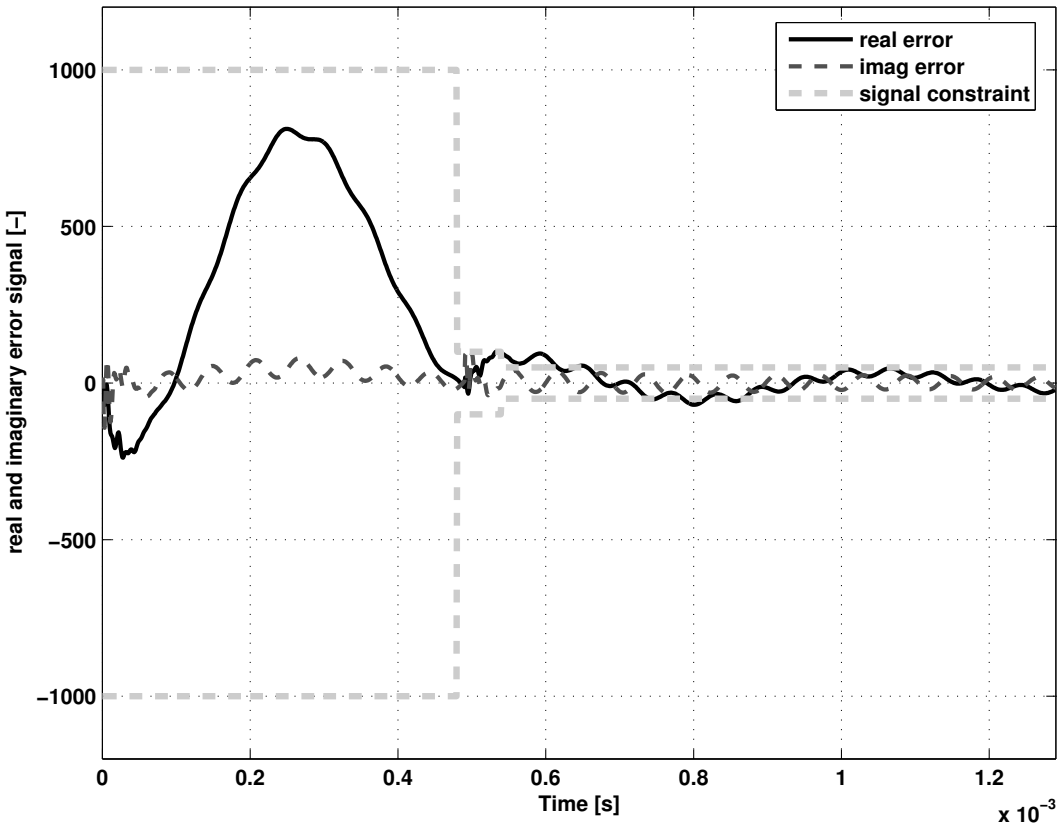

Figure D.11: Real and imaginary control errors for PI-controlled model with signal constraints

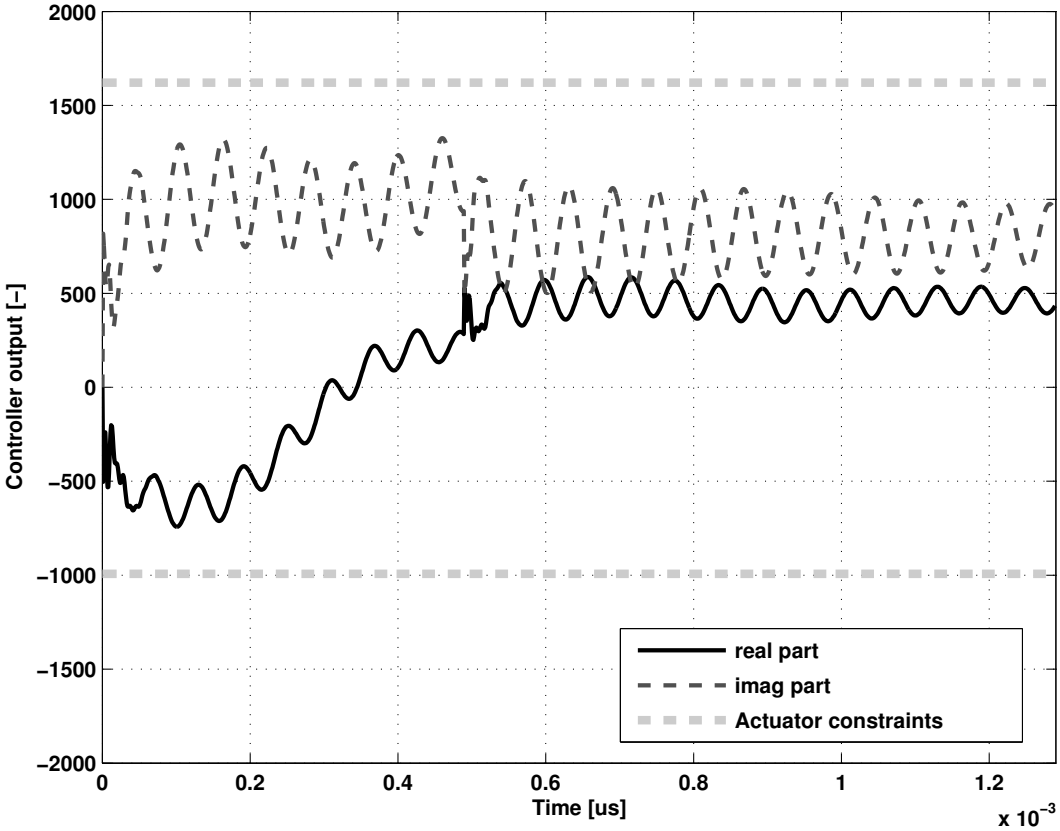

Figure D.12: Real and imaginary controller output signals (u_r and u_i) and actuator constraints (PID controller)